Variational and Multiscale Modeling of Amorphous Silica Glass

Thesis by
William J. Schill

In Partial Fulfillment of the Requirements for the
Degree of
Doctor of Philosophy in Mechanical Engineering

CALIFORNIA INSTITUTE OF TECHNOLOGY
Pasadena, California

2020
Defended June 6, 2019

© 2020

William J. Schill
ORCID: 0000-0003-0950-7433

All rights reserved

ACKNOWLEDGEMENTS

I would like thank my advisor Professor Michael Ortiz for being a truly fantastic mentor over the course of the PhD. I have greatly enjoyed our many conversations in mechanics, physics, and mathematics. I have also greatly appreciated your *many* excellent book suggestions in various topics in math and engineering over the years (though it has resulted in me spending an embarrassingly large percentage of my graduate stipend on books).

I would like to thank my committee members Kaushik Bhattacharya, Laurent Stainier, and Nadia Lapusta for agreeing to be on my committee. I would also like to acknowledge Dennis Kochmann who — though not on my committee — has given me lots of great advice over the years and from whom I have taken many fantastic courses.

I have been fortunate to have many excellent collaborators on papers from whom I have learned much during the PhD. In particular, I would like to acknowledge Bo Li, Stefanie Heyden, Sergio Conti, J.P Mendez, and Laurent Stainier.

I have been very fortunate to have ample financial support during my graduate studies. During my first year I had funding through MCE option fellowship. Thereafter, I was supported through a grant by the ONR, then the Saffman Fellowship, and finally for the last two years this work was supported by a Nasa Space Technology Research Fellowship (NSTRF). I would like to specifically acknowledge Justin Haskins who has been my mentor under the NSTRF with whom I've had many great conversations regarding the mission needs of NASA and about physics in general.

My officemates Erika, Trent, and Arnold have made the PhD a joy and coming to work each day a lot of fun. I would like to in particular comment that many of the figures contained herein would not look nearly so nice without the expert advice of Erika and Trent. I would like to particularly thank Lydia Suarez, who helped me tirelessly with logistics and travel.

My friends and colleagues from Caltech have made this time lots of fun. I recall many many hours doing homework sets as well as fun times with Carlos, Joe, Matt, Greg, and everyone else in my fist year class. My SOPS co-pilot Tori made running that organization for several years a wonderful experience. Dingyi was an excellent mentor during my early days in graduate school, provided lots of great advice and discussion particularly on the multiscale aspect of my work, and got me to apply to conferences which were a great learning experience. I would like to thank Paul

for our many discussions during the early days of my PhD regarding calculus of variations.

I would like to thank my parents for being supportive of my academic endeavors. Particularly, I would like to thank my father, who dedicated many years to my education, fostered my interest in science and math, encouraged me to pursue engineering, and even to this day has been willing to proof-read any document I send him (including much of the content of this thesis).

I would also like to acknowledge my sister Megan for endless support and just in general for being a lot of fun.

Finally, I would like to thank my wife, Jacquelynn, who has not only tolerated my pursuit of a PhD but has been an incredible and supportive spouse throughout.

ABSTRACT

We develop a critical-state model of fused silica plasticity on the basis of data mined from molecular dynamics (MD) calculations. The MD data is suggestive of an irreversible densification transition in volumetric compression resulting in permanent, or plastic, densification upon unloading. Moreover, this data exhibits dependence on temperature and the rate of deformation. We show that these characteristic behaviors are well-captured by a critical state model of plasticity, where the densification law for glass takes the place of the classical consolidation law of granular media and the locus of constant volume states denotes the critical-state line. A salient feature of the critical-state line of fused silica, as identified from the MD data, that renders its yield behavior anomalous is that it is strongly non-convex, owing to the existence of two well-differentiated phases at low and high pressures. We argue that this strong non-convexity of yield explains the patterning that is observed in molecular dynamics calculations of amorphous solids deforming in shear. We employ an explicit and exact rank-2 envelope construction to upscale the microscopic critical-state model to the macroscale. Remarkably, owing to the equilibrium constraint the resulting effective macroscopic behavior is still characterized by a non-convex critical-state line. Despite this lack of convexity, the effective macroscopic model is stable against microstructure formation and defines well-posed boundary-value problems. We present examples of ballistic impact of silica glass rods by way of the optimal transport meshfree method. We extend the study of the inelastic behavior of silica glass to include the effect of many different temperatures, pressures, and strain rates using MD and maximum entropy atomistics (MXE) calculations. Owing to the temperature dependence of the model, the macroscopic model becomes unstable against adiabatic shear localization. Thus, the material adopts small inter-facial regions where the shear strain is extremely high. We characterize the shear band size, thereby predicting a yield knockdown factor at the macroscale, and compare the results to behavior reported in flyer plate impact experiments.

PUBLISHED CONTENT AND CONTRIBUTIONS

[1] W. Schill and S. Heyden and S. Conti and M. Ortiz, 2018, The anomalous yield behavior of fused silica glass, Journal of the Mechanics and Physics of Solids, V. 113, 105 - 125, 0022-5096, doi: https://doi.org/10.1016/j.jmps.2018.01.004, url: http://www.sciencedirect.com/science/article/pii/S0022509617309158,
WS contributed to all aspects of all the work contained herein.

[2] W. Schill and B. Li and M. Ortiz, 2019, Optimal transport meshfree analysis of the impact of glass rods, In Preparation,
WS contributed to all aspects of all the work contained herein.

[3] W. Schill and J.P. Mendez and M. Ortiz, 2019, Temperature, rate, and the anomalous yield strength of fused silica glass, In Preparation,
WS contributed to all aspects of all the work contained herein.

[4] W. Schill and L. Stainier and M. Ortiz, 2019, Shear localization in fused silica glass, In Preparation,
WS contributed to all aspects of all the work contained herein.

TABLE OF CONTENTS

LIST OF ILLUSTRATIONS

LIST OF TABLES

Chapter 1

INTRODUCTION

A leitmotif of present day engineering physics is *multiscale modeling* – the process of extracting information from fundamental physics to inform a reduced order model at some length and time scale of interest to particular engineering applications. In this work, we will utilize molecular scale modeling strategies (introduced in more detail within each of the subsequent chapters) at small length and time scales. Though there are many potential macroscale applications of a multiscale modeling approach, we have been in particular motivated by problems involving ballistic and hypervelocity impact. The physical processes involved in these problems are of high importance in spacecraft protection against micro-meteoroids and in armor applications among others. Such physics are typically highly dependent on many length and timescales and consequently are complex to model. However, the precise characterization is of high importance in the context of design for these applications.

A complementary point of view is that of *variational modeling* – the formulation of a physics problem from an optimization perspective and corresponding analysis of the behavior (and existence) of its solutions. Multiscale modeling might be said to comprise a bottom-up strategy whereas analysis of the variational structure of a macroscale problem might be said to follow a top-down order of business (there are certainly exceptions to this, for instance, there are many applications of Γ-convergence, a variational convergence technique, used in deriving macroscopic behavior from collections of particles). Whereas multiscale modeling seeks to find homogenized values for use in larger scale physics, the variational perspective seeks to establish conditions under which the macroscale problem will be well behaved and amenable to solution. The omission of the former will of course result in a lack of fundamental material information. The neglect of the latter risks the formulation of macroscale physics laws for which the solution may be poorly behaved. For instance, the solution may exhibit artificial dependence on parameters of a computational strategy such as mesh size. Such dependence carries the dangerous potential to ruin any predictive capacity provided by the model. To establish a complete and robust understanding of material behavior requires the utilization of *both* perspectives.

In this thesis, we explore the inelastic behavior of amorphous (also known as fused)

silica (SiO_2) glass. Silica glass exhibits certain characteristics under high pressures which elevate it out of the mundane and into the extraordinary.

First, silica exhibits non-monotonic dependence on pressure by the elastic moduli [35]. Second, and perhaps even more unusual, silica shows a significant decrease in strength in certain regimes as it is compressed to denser structures with higher coordination [57]. We refer to this process as the *anomalous yield behavior* specifically in the sense that the dependence of the shear yield strength on the pressure is non-monotonic. We will find in this work that this essentially implies that the limit domain — in the sense of critical state theory — is non-convex. This a highly unusual property for a plasticity model. Third, in Taylor type bar-impact experiments, silica glass fails via *failure waves* [9]: the rapid fragmentation of a material behind a traveling high pressure region. Finally, under experimental conditions of flyer plate impact, silica may undergo large drops in stress [90]. These studies also include instances where the experimental conditions, such as temperature and strain rate, may vary dramatically resulting in microstructured deformation such as *shear strain localization*.

We analyze all of these behaviors from a variational and multiscale perspective ultimately providing a comprehensive and well posed model for amorphous silica glass. In Chapter 2, we focus on the study of the anomalous yield behavior. We mine data from molecular dynamics and develop a finite deformation Cam-Clay model of plasticity. We find that a *non-local* formulation of the kinetic relation governing plastic flow in tandem with a concept from the direct methods in the calculus of variations [24] known as $\mathcal{A}$-quasi-convexity results in a well-posed model that captures the MD data.

In Chapter 3, we apply this model to the study of failure waves in glass rods using the optimal transport meshfree method and find the speed of the failure waves and the general characteristics of the behavior are well captured by the model. In Chapter 4, we introduce the effect of temperature and rate into the model. Specifically, we utilize max-ent-atomistics to aid in the characterization of rate. We find that the model captures the data well and the anomalous yield behavior persists across a vast range of temperatures and strain rates.

Variation in the temperature and rate is often the culprit for localization in the deformation field. Such shear localization is of high importance in the inelastic behavior of materials and is often a precursor to catastrophic failure by fracture. The analysis of the occurrence of localization is the subject of Chapter 5. Specifically, we

leverage the variational structure of the model to jointly solve for both phase volume fractions as well as the micro-length scale. This amounts to essentially a rank-one convexification of the material model. The competition between thermal softening and rate hardening – which we have derived from microscale physics – dictates these processes. We compare the results of these calculations to experimental flyer plate impacts and find good agreement.

Chapter 2

ANOMALOUS YIELD BEHAVIOR OF FUSED SILICA GLASS

Research presented in this chapter has been adapted from [78].

2.1 Introduction

The anomalous shear modulus behavior of silica glass has been a long-standing topic of investigation. For instance, [35] and references therein examined the non-monotonic dependence of the elastic moduli on pressure for fused quartz, cf. Fig. 2.1a. Notably, between 0 and 2.5 GPa, the shear modulus and bulk modulus decreases. Likewise, the anomalous pressure dependence of the strength of amorphous silica has also received considerable attention. For instance, [57] made measurements of the yield strength at pressures up to 81 GPa at room temperature and showed that the strength of amorphous silica decreases significantly as it is compressed to denser structures with higher coordination, Fig. 2.1b. Clifton *et al.* [1, 12, 90] and [84] investigated the effect of pressure on failure waves in silica and soda-lime glass through angled flyer plate impact experiments and observed a loss of shear strength as the failure wave traversed the glass at pressures of 4-6 GPa.

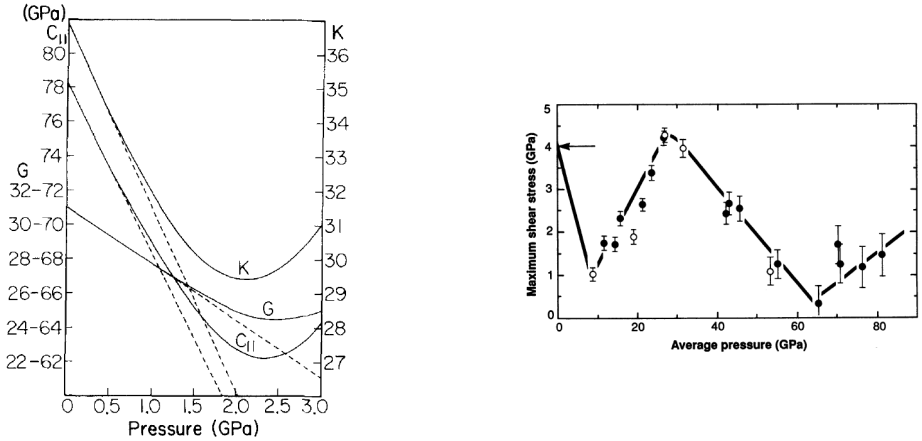

Figure 2.1: a) Elastic moduli *vs*. pressure as measured by [35]; b) Measurements of the yield strength of SiO_2 glass at pressures as high as 81 GPa at room temperature showing the variation of the strength of amorphous silica as it is compressed to denser structures with higher coordination [57].

These phenomena appear to be intimately linked to structural rearrangements occurring at the atomic level. [75, 76] performed structural measurements of SiO_2 glass

Si-O bond length and coordination number at pressures from 20 to 100 GPa using a diamond anvil cell and x-ray diffraction. They observed a transition from four-fold to six-fold coordinated structure that comes to completion at around 45 GPa. [101] studied the densification behavior again using a diamond anvil cell experimental setup and concluded that permanent densification occurs for pressures between 9 and 13 GPa. [99] observed pressure-induced reorganizations of the amorphous network allowing a more efficient packing of tetrahedra that remain linked at their vertices only. [30] studied transformations at pressures of up to about 20 GPa and temperatures of up to about 700 C. Their results are indicative of the existence of a high pressure variant of silica glass. However, a sharp phase transformation was not observed, which is suggestive of a volumetric plastic hardening mechanism. [50] reported a novel dense silica polymorph retrieved from shock-wave and diamond-anvil cell experiments. The polymorph is composed of face-sharing polyhedra and it has a density similar to stishovite. Sterical constraints on the bond angles induce an intrinsic disorder in the Si positions and the resulting Si-coordination is transitional between four and sixfold.

Beyond the specific instance of fused silica, there exists an extensive literature on the microstructural mechanisms that mediate plastic deformation in amorphous solids. [19] observed that in amorphous silicon plastic deformation is mediated by autocatalytic *avalanches* of unit inelastic shearing events. They performed a bond-angle analysis in order to correlate changes in the average bond angle to discrete relaxation events. Langer et al. [23, 40] formulated a theory of *shear transformation zones* (STZ) to describe viscoplastic deformation in amorphous solids. Langer's theory accounts for the formation of deformation patterns such as shear banding in metallic glasses. An alternative theory of structural rearrangement in bulk metallic solids is based on *free-volume* kinetics. [11] observed that the flow in metallic glasses is strongly inhomogeneous at high stresses and low temperatures, and attributed the patterning to local reductions in flow strength. [69] and [85] argued that these reductions are due to the formation of free volume, and that the attendant inhomogeneous flow is controlled by the competition between the stress-driven creation and diffusional annihilation of free volume. This hypothesis was later verified experimentally by [3].

There have also been extensive molecular dynamics studies of the densification behavior and plastic deformations of amorphous silica. [67], [37], [102], and [28, 29] computed pressure-density relationships over a broad range of pressures

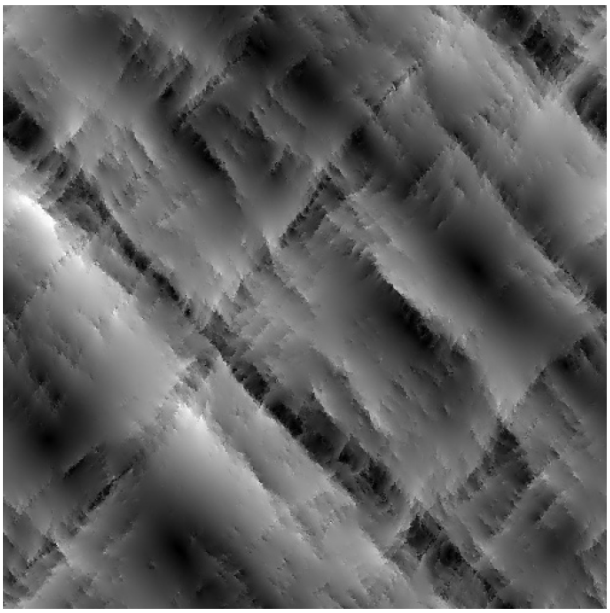

Figure 2.2: Molecular dynamics calculation of an idealized amorphous solid showing distinctive patterns in the deformation field (the darker color indicates larger non-affine displacements) [53].

and temperatures. The attendant mechanisms of deformation entail transitions from four-fold to six-fold coordination. In particular, [102] argued that the four-fold to six-fold transition is not direct but involves the formation of an intermediate five-fold coordinated structures at $\sim$ 12 GPa and is only complete at $\sim$ 60 GPa. [45] noted anomalous behavior in the form of a minimum shear strength occurring at $\sim$ 10 GPa and proposed a mechanism involving unquenchable 5-fold defects. [54] utilized an NVE ensemble along with monoclinic change in the simulation box orientation to study combined pressure-shear loading. They observed steps, or *jerking*, in the shear stress *vs*. shear strain response, which they attribute to either finite size effects or localized dissipative rearrangements. Several authors [42, 53] have performed molecular dynamics calculations on amorphous solids deforming under shear and found that the resulting deformation field forms distinctive patterns to accommodate permanent deformations, Fig. 2.2.

This past work strongly suggests that the plastic deformation of amorphous solids and, in particular, fused silica glass, is mediated by localized atomic-level instabilities that promote deformation patterning, Fig. 2.2. Such fine-scale pattern formation is reminiscent of the microstructure attendant to the relaxation of non-convex energy functionals [16]. We argue that a critical state plasticity model [74, 83] characterized by a *strongly non-convex* critical-state line in pressure-shear space explains the ob-

served patterning. In order to formulate the theory, we perform Molecular Dynamics (MD) calculations designed to mine data on the volume-pressure relation and the pressure-shear response of fused silica, Section 2.2. In Section 2.3, we formulate a critical state constitutive model that closely reproduces the phenomenology revealed by the MD data. The data suggest that the critical-state line in the pressure-shear plane is indeed strongly non-convex. The handling of non-convexity necessitates a fundamental extension of classical plasticity, which is based on the principle of maximum dissipation and is predicated on the assumption of convexity of the elastic domain. In Section 2.4, we consider the implications of this extension and utilize notions from the Direct Methods in the Calculus of Variations to characterize explicitly and exactly the effective, or *relaxed*, behavior of fused silica at the macroscale. Remarkably, owing to the equilibrium constraint the effective macroscopic behavior of fused silica is still strongly non-convex, despite being stable with respect to microstructure formation. In particular, it defines well-posed boundary-value problems.

2.2 Supporting Molecular Dynamics calculations

We use MD calculations for purposes of data mining, as well as to gain insight into the molecular basis of the inelasticity of glass.

NB (Pressure sign convention): *In keeping with the standard sign convention in experimental work and in MD, we take compressive pressure to be positive and tensile pressure to be negative.*

Methodology

All calculations are performed using Sandia National Laboratories (SNL) Large-scale Atomic/Molecular Massively Parallel Simulator (LAMMPS) [68]. Calculations are carried out by explicit velocity-Verlet dynamics [96] with a time step of 0.5 fs for a total of 10^6 time steps up to maximum deformations of the order of 20%, corresponding to strain rates of approximately 4×10^8 1/s. The representative volume element (RVE) contains $1,536$ atoms and is subjected to periodic boundary conditions. We utilize 4^3 primitive lattice cells of β-cristobalite to construct RVEs $4\times7.16 = 28.64$ Å wide. We have verified that unit cells comprising 8^3 lattice cells do not significantly alter the results of the calculations.

All calculations are performed at a temperature of 300K. Long-range Coulombic interactions are evaluated by Ewald summation [95]. Short-range interactions are

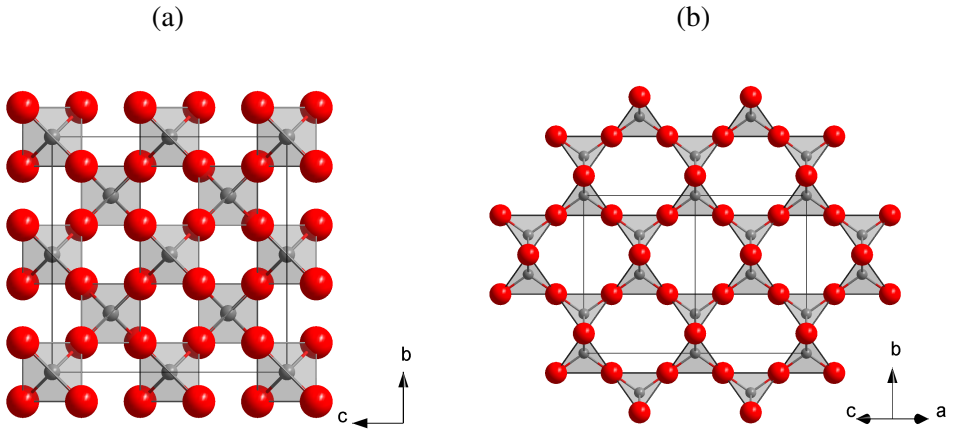

Figure 2.3: Two views of the crystal structure of β-cristobalite (By Solid State (Own work) [Public domain], via Wikimedia Commons). Si: red atoms; O: grey atoms.

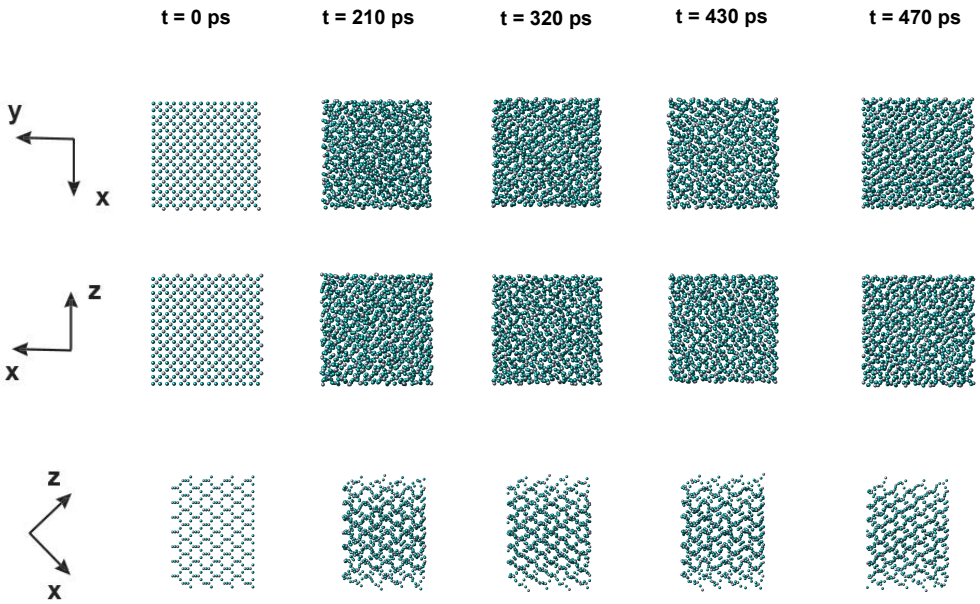

Figure 2.4: Rapid cooling of a β-cristobalite melt and generation of an amorphous structure. Sample is cooled from β-cristobalite structure at $T = 5000$K to $T = 300$K in $t = 470$ ps.

assumed to obey the modified BKS potential

$$E(r_{ij}) = A\exp(-r_{ij}/\rho) - C/r_{ij}^6 + D/r_{ij}^{12},$$

proposed by [52], where r_{ij} represents the interatomic distance. This potential modifies the BKS potential proposed by [97] by the insertion of an additional repulsive short-range interaction term in order to increase calculation stability. The additional repulsive term additionally prevents the unphysical divergence of the

potential at small interatomic distances. The parameters A, C, D, and ρ used in calculations may be found in Table 4 of [52].

In order to obtain an initial amorphous state of SiO_2, we utilize the melt quench procedure No. 2 of [52]. This quench procedure is performed on an NVT ensemble [95] and consists of cooling a β-cristobalite melt, Fig. 2.3, from 5000K to 300K over 470 fs with a time step of 2 fs, Fig. 2.4.

The results of the calculations exhibit fluctuations that are sensitive to initial conditions. To assess this influence and, where appropriate, to average out the effects of random fluctuations, we perform the same calculations for multiple initial amorphous states. These states are obtained by holding the temperature fixed at 50 0 0 K for different periods of time during which the atoms rearrange. Four separate initial conditions are generated using rearrangement periods of 10 0 0, 150 0, 20 0 0, and 30 0 0 time-steps. Subsequent calculations utilize Nosé-Hoover style barostat equations (cf. Eqs. (1)–(3) in Shinoda et al., 2004), to control pressure and temperature. The free parameters regulating the response time are chosen to be T damp = 0 . 05 ps and P damp = 0 . 5 ps.

Volumetric behavior

We begin by querying the behavior of amorphous silica under compressive volumetric loading and unloading. Fig. 2.5 shows the computed dependence of pressure on volume, including unloading from a range of maximum pressures. At low maximum pressures, the material unloads ostensibly elastically and returns to its initial undeformed configuration upon unloading. By contrast, at pressures above $\sim$ 8 GPa the material undergoes a distinctive permanent densification transition and the unloading curve exhibits permanent volumetric deformation.

Past studies [28, 29, 67] have reported similar pressure-density relationships, but calculations to date have been limited to significantly smaller sample sizes and monotonic loading. We note that without unloading it is not possible to ascertain whether the material response is nonlinear elastic, and therefore governed by a simple equation of state, or elastic-plastic. The results collected in Fig. 2.5 clearly reveal that the latter is indeed the case and that the volumetric response of glass exhibits inelasticity in the form of loading-unloading irreversibility, path-dependency and hysteresis at sufficiently high pressures.

Radial distribution functions are commonly used as a validation and interpretation

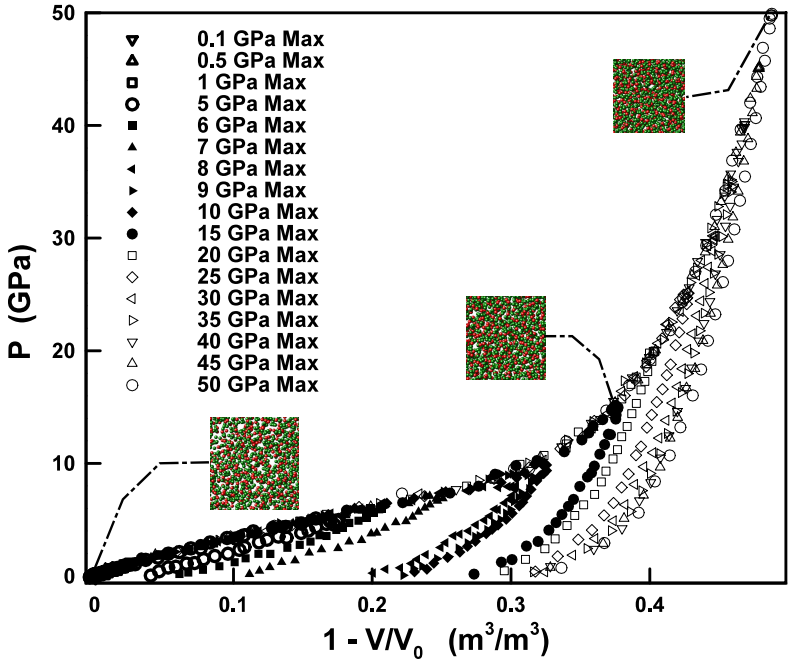

Figure 2.5: Pressure-compression response showing densification transition at ~ 8 GPa and unloading from several pressures showing permanent densification upon full unloading.

metric in MD simulations [32, 33]. Fig. 2.6 shows the computed radial distribution function at 50 GPa. By way of comparison, Fig. 2.6 also shows corresponding experimental measurements performed by [75]. As can be seen from the figure, the MD calculations accurately capture the location and amplitude of the first peak in the radial distribution, which determines the radius of the first shell of atoms, and, to a fair degree of approximation, the location and amplitude of the second peak. The tails of the computed and measured radial distributions differ in fine detail but exhibit a similar rate of decay.

In order to elucidate the atomic-level mechanisms underlying permanent volumetric deformation, we examine the evolution of the *coordination number* [33, 98]

$$CN = \int_0^{r_m} \rho g(r)\, 4\pi r^2\, dr, \tag{2.1}$$

where ρ is the particle density, or number of atoms per unit volume, $g(r)$ is the radial distribution function and r_m is the location of the first minimum of $g(r)$. The coordination number measures the number of nearest-neighbors of an atom. A simple way to approximate equation (2.1) given a set of atomic positions, is to perform a Voronoi tessellation of the atoms and then count the number of faces

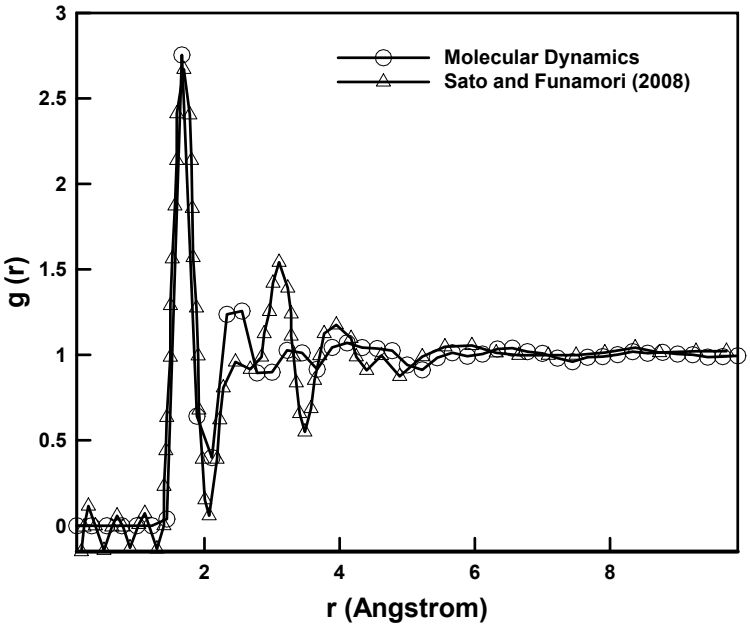

Figure 2.6: Computed and experimentally measured [75] radial distribution function at pressure $p = 50$ GPa.

of individual Voronoi cells. In order to mitigate the effect of noise, a face is not counted if its area is below 1.3 Å^2, if it has more than 10 edges, or if one of its edges is shorter that 0.5 Å. Fig. 2.7 shows the evolution of the distribution of coordination numbers in a sample during compressive volumetric loading and unloading up to a pressure of 50 GPa. Initially, the entire sample consists of 4-fold coordinated atoms, Figs. 2.7a and 2.7b. At peak pressure, the coordination of most atoms changes from 4-fold to 6-fold, but a significant fraction of atoms exhibits an intermediate coordination. Remarkably, upon unloading, only a small fraction of atoms recovers a 4-fold coordination, with the second largest fraction retaining 6-fold coordination and the majority of the sample remaining in an intermediate 5-fold coordination. These results evince the irreversible nature of the structural transitions attendant to permanent densification of glass, in agreement with experimental observations [30, 50, 75, 76, 99, 101]. The prevalence of transitional structures with a preponderance of 5-fold atoms upon unloading is also in agreement with the calculations of [102] and the experimental observations of [50].

Pressure-shear coupling

Using the same initial amorphous configuration of atoms, we now subject the RVE to pressure followed by monotonic shear deformation. To impart the shear deformation, affine boundary conditions are applied to the boundary of the RVE while simultaneously controlling the pressure by means of a barostat. We generate shear stress-strain curves over a range of pressure and we average the curves over a sample of initial conditions.

The resulting average shear stress-strain curves are shown in Fig. 2.8. The shear stress-strain curves exhibit an initial pressure-dependent elastic stage followed by yielding. The computed dependence of the shear modulus on pressure is shown in Fig. 2.9, which also includes measurements by [35] by way of comparison. As may be seen from the figure, the MD results capture the anomalous initial decrease of the shear modulus with pressure [12]. Furthermore, the MD results closely match the experimental measurements, which provides a measure of model validation.

A salient feature of the shear stress-strain curves is the serrated nature of the yield plateau, also known as *jerky flow*, Fig. 2.8. These serrations have been associated with localized bursts of atomic movements, or *avalanches* [19]. In order to detect and quantify these avalanches, [23] proposed the parameter

$$D(i) \equiv \min_{\boldsymbol{\beta}\in\mathbb{R}^{3\times 3}} \left(\sum_j \left| (\boldsymbol{u}_j - \boldsymbol{u}_i) - \boldsymbol{\beta}(\boldsymbol{r}_j - \boldsymbol{r}_i) \right|^2 \right)^{1/2}, \tag{2.2}$$

which represents the deviation of the incremental displacements $\boldsymbol{u}_j$ of the atoms in a neighborhood of a reference atom i from an incremental affine deformation. Spikes in the distribution of $D(i)$ may therefore be identified with the occurrence of avalanches around atom i. Fig. 2.10 shows the distribution of $D(i)$ at points of a shear stress-strain curve when such avalanches occur. In this case, no averaging with respect to initial conditions is performed in order to preserve fluctuations. As may be seen from the figure, the occurrence of avalanches correlates closely with drops in the stress-strain curve, which identifies avalanches as the agents of plastic deformation and the mechanism underlying the observed jerky plastic flow.

Volume evolution and critical state behavior

A fundamental characteristic of the pressure-shear response of glass, especially as regards the categorization of its plastic response, concerns the evolution of volume during shearing deformation. In order to ascertain this behavior, we deform samples volumetrically up to a maximum pressure $p_{\max}$, or *preconsolidation pressure*, and

subsequently unload to a lower pressure $p \leq p_{\max}$, or *confining pressure*. The samples are then deformed in shear at constant confining pressure p.

Fig. 2.11, shows the evolution of the volume of the sample with shear deformation at four values of confining pressure p and a range of preconsolidation pressures $p_{\max} \geq p$. The striking feature in these plots is that, in all cases, the volume of the sample attains a *limiting volume*, or *critical state*, at sufficiently large shear deformation. The critical state is attained both under compressive (positive) and tensile (negative) confining pressures. The limiting volume depends on the confining pressure but is independent of the preconsolidation pressure, Fig. 2.11. The calculations also show that, at the critical state, the sample deforms at a constant shear stress that depends on the confining pressure but is independent of the preconsolidation pressure. The volume initially decreases in under-consolidated samples, $p_{\max} \lesssim 2p$, and increases in over-consolidated samples, $p_{\max} \gtrsim 2p$. Similar trends are observed in the evolution of the volumetric strain, Fig. 2.12. We remark that independence of material behavior from pre-pressure has direct analogs in several existing theories of amorphous plasticity. Thus, both the Shear Transition Zone [23] and free-volume theories [69] exhibit independence of long term behavior from initial amounts of free volume.

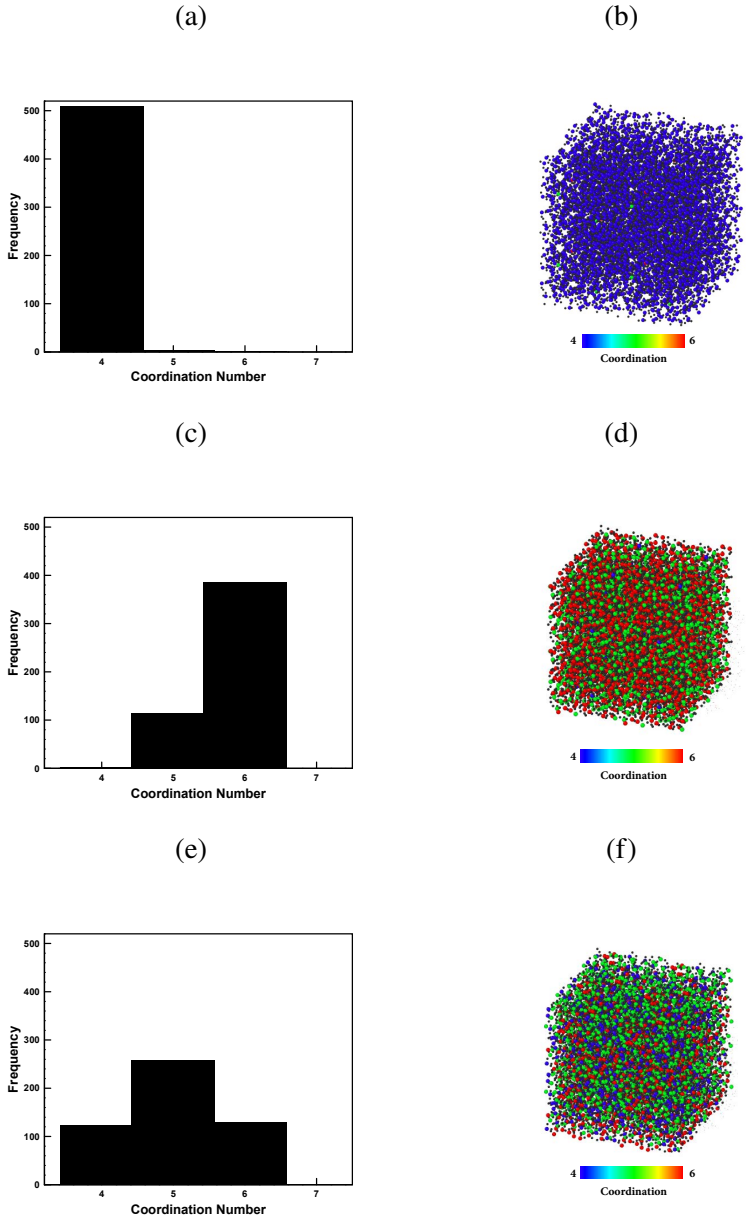

Figure 2.7: Evolution of the distribution of coordination numbers of the atoms in a sample during volumetric-compression loading and unloading up to a pressure of 50 GPa. Si atom coordination numbers are illustrated by the color bar and the oxygen atoms are represented as black spheres. (a) and (b) Initial state; (c) and (d) Peak pressure. (e) and (f) Unloaded state.

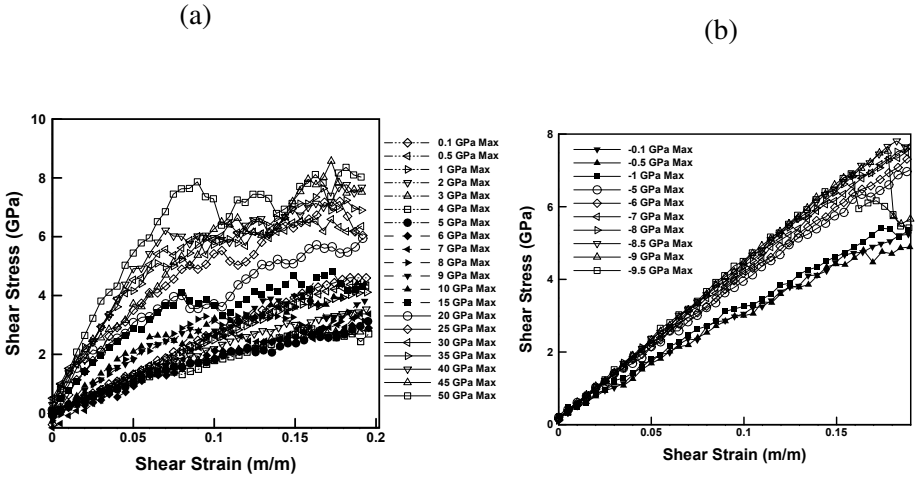

Figure 2.8: a) Shear stress *vs*. shear strain under compressive pressure. b) Shear stress *vs*. shear strain under tensile pressure.

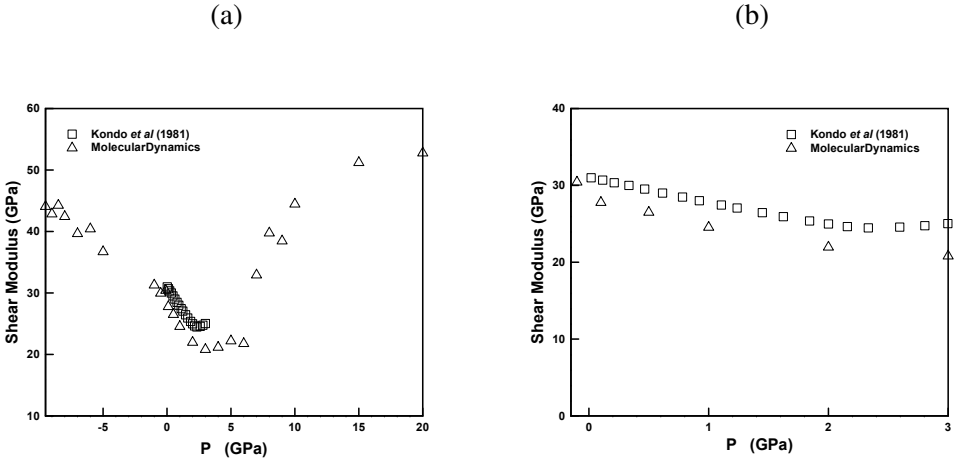

Figure 2.9: Computed and experimentally measured [35] dependence of the shear modulus on pressure. a) Overall view showing initial anomalous dependence. b) Detail of the pressure range of 1-3 GPa.

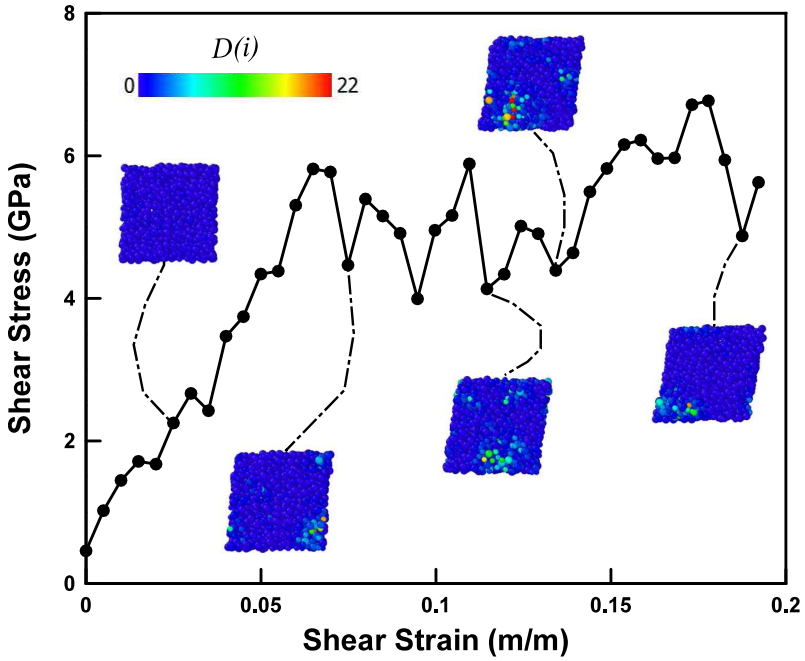

Figure 2.10: Shear stress *vs.* shear strain curve and shear transition zones at serrations. We compute $D(i)$ from equation (2.2) and color the atoms to indicate variation in this parameter. Blue indicates affine deformation whereas yellow and red indicate medium and large non-affine deformations, respectively.

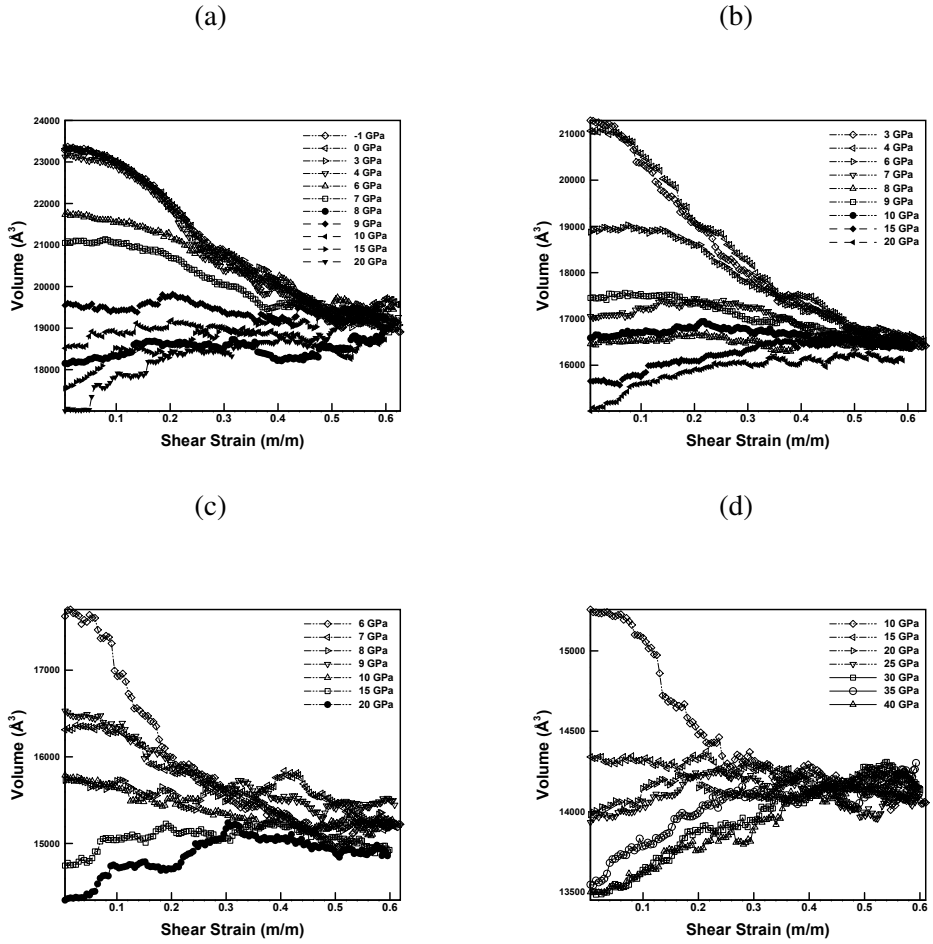

Figure 2.11: Evolution of volume during pressure-shear response for different values of preconsolidation pressure p_{max} (shown inset in the figures) and confining pressure p. a) $p = -1$ GPa. b) $p = 3$ GPa. c) $p = 6$ GPa. d) $p = 10$ GPa.

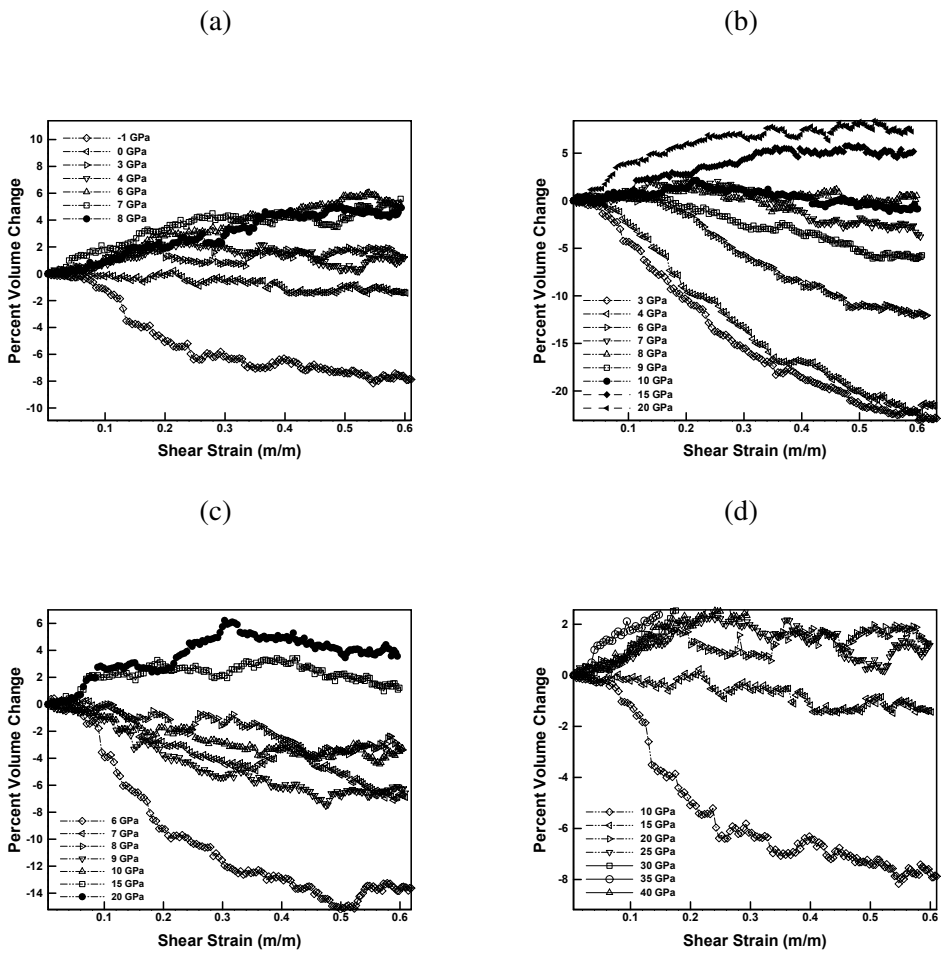

Figure 2.12: Evolution of volumetric strain during pressure-shear response for different values of preconsolidation pressure p_{max} (shown inset in the figures) and confining pressure p. a) $p = -1$ GPa. b) $p = 3$ GPa. c) $p = 6$ GPa. d) $p = 10$ GPa.

(a) (b)

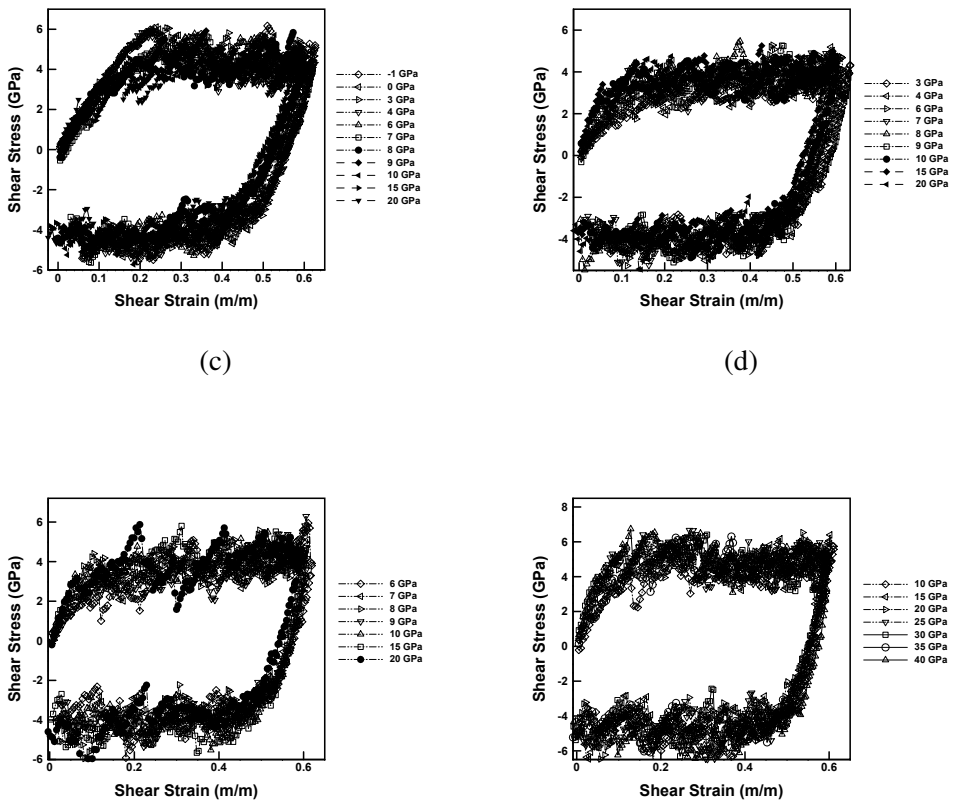

(c) (d)

Figure 2.13: Shear stress *vs.* shear strain for different values of preconsolidation pressure p_{max} (shown inset in the figures) and confining pressure p. a) $p = -1$ GPa. b) $p = 3$ GPa. c) $p = 6$ GPa. d) $p = 10$ GPa.

2.3 Mesoscopic Critical-State Model

The preceding MD data provides a basis for the formulation of a mesoscopic continuum model of the inelasticity of fused silica glass. In particular, the attainment of a critical state in the evolution of volume under pressure-shear loading, Section 2.2, strongly suggests a representation based on critical-state theory of plasticity [74, 83]. A central tenet of critical-state theory is that a solid confined at fixed pressure attains a critical state after sufficient shear deformation beyond which subsequent plastic deformation occurs at constant volume and without further consolidation. In this section, we investigate the ability of critical-state theory to describe the behavior of glass gleaned from molecular dynamics.

Finite kinematics

In view of the large deformations that occur over the pressure range of interest, we formulate the theory in finite kinematics. We assume a standard multiplicative decomposition of the deformation gradient $\boldsymbol{F}$ of the form [41]

$$\boldsymbol{F} = \boldsymbol{F}^e \boldsymbol{F}^p \tag{2.3}$$

into an elastic part $\boldsymbol{F}^e$ and a plastic part $\boldsymbol{F}^p$. We denote by $J = \det(\boldsymbol{F})$, $J^e = \det(\boldsymbol{F}^e)$ and $J^p = \det(\boldsymbol{F}^p)$ the corresponding Jacobians.

Equilibrium relations

We further adopt a thermodynamic formalism [46, 47] to describe the local inelastic processes and postulate the existence of a Helmholtz free energy density per unit undeformed volume of the general form

$$A = W^e(\boldsymbol{C}^e, T) + W^p(J^p, T), \tag{2.4}$$

where

$$\boldsymbol{C}^e = \boldsymbol{F}^{eT} \boldsymbol{F}^e \tag{2.5}$$

is the elastic right Cauchy-Green deformation tensor, W^e is the thermoelastic strain energy density per unit undeformed volume and W^p is the stored energy density per unit undeformed volume. The corresponding equilibrium relations are

$$\boldsymbol{P} = \frac{\partial W}{\partial \boldsymbol{F}} = 2\boldsymbol{F}^e \frac{\partial W^e}{\partial \boldsymbol{C}^e} \boldsymbol{F}^{p-T}, \tag{2.6a}$$

$$\boldsymbol{Y} = -\frac{\partial W}{\partial \boldsymbol{F}^p} = \left(\boldsymbol{C}^e \frac{\partial W^e}{\partial \boldsymbol{C}^e} + \frac{\partial W^e}{\partial \boldsymbol{C}^e} \boldsymbol{C}^e \right) \boldsymbol{F}^{p-T} - \frac{\partial W^p}{\partial J^p} J^p \boldsymbol{F}^{p-T}, \tag{2.6b}$$

where $\boldsymbol{P}$ is the first Piola-Kirchhoff stress tensor and $\boldsymbol{Y}$ is the thermodynamic driving force conjugate to $\boldsymbol{F}^p$. We additionally assume that the elastic behavior of glass is isotropic. In particular,

$$\boldsymbol{C}^e \frac{\partial W^e}{\partial \boldsymbol{C}^e} = \frac{\partial W^e}{\partial \boldsymbol{C}^e} \boldsymbol{C}^e. \tag{2.7}$$

Using this identity, the rate of dissipation evaluates to

$$\boldsymbol{Y} \cdot \dot{\boldsymbol{F}}^p = J\, \boldsymbol{y} \cdot \boldsymbol{d}^p, \tag{2.8}$$

where

$$\boldsymbol{y} = \boldsymbol{\sigma} + p_c \boldsymbol{I} \tag{2.9}$$

is a spatial driving force,

$$\boldsymbol{d}^p = \frac{1}{2}(\boldsymbol{l}^p + \boldsymbol{l}^{pT}) = \frac{1}{2}\big(\dot{\boldsymbol{F}}^p \boldsymbol{F}^{p-1} + (\dot{\boldsymbol{F}}^p \boldsymbol{F}^{p-1})^T\big) \tag{2.10}$$

is the plastic rate of deformation tensor,

$$J\boldsymbol{\sigma} = 2\boldsymbol{F}^e \frac{\partial W^e}{\partial \boldsymbol{C}^e}(\boldsymbol{C}^e, T)\boldsymbol{F}^{eT} \tag{2.11}$$

is the Cauchy stress and

$$J p_c = -J^p \frac{\partial W^p}{\partial J^p}(J^p, T) \tag{2.12}$$

is a critical pressure.

Flow rule

In view of the structure of the rate-of-dissipation identity (2.8), and following the classical kinetic theory of Onsager, we assume the existence of a dual kinetic potential $\psi^*(\boldsymbol{y}, J^p)$ such that

$$\boldsymbol{d}^p = \frac{\partial \psi^*}{\partial \boldsymbol{y}}(\boldsymbol{y}, J^p). \tag{2.13}$$

We allow for a dependence of ψ^* on J^p in order to account for the effect of densification of the glass on its flow characteristics. We also note that objectivity, or invariance under rotations superposed on the spatial configuration, follows from the assumed isotropy of $\psi^*(\cdot, J^p)$. If, in addition, we idealize the kinetics of plastic deformation as rate-independent, then $\psi^*(\boldsymbol{y}, J^p)$ is the indicator function of an elastic domain $E(J^p) \subset \mathbb{R}^{3\times 3}_{sym}$, i.e.,

$$\psi^*(\boldsymbol{y}, J^p) = I_{E(J^p)}(\boldsymbol{y}) = \begin{cases} 0, & \text{if } \boldsymbol{y} \in E(J^p), \\ +\infty, & \text{otherwise.} \end{cases} \tag{2.14}$$

Because of the extended character and lack of differentiability of $I_{E(J^p)}(\boldsymbol{y})$, the potential relation (2.13) needs to be understood in the sense of some appropriate notion of generalized derivative, or flow rule. If $E(J^p)$ is convex, the appropriate generalized derivative is supplied by the set-valued subdifferential [72]

$$\boldsymbol{d}^p \in \{\boldsymbol{r} \in \mathbb{R}^{3\times 3}_{sym} \text{ s. t. } (\boldsymbol{y} - \boldsymbol{y}^*) \cdot \boldsymbol{r} \geq 0, \ \forall\, \boldsymbol{y}^* \in E(J^p)\}, \tag{2.15}$$

which embodies Drucker's principle of maximum dissipation, which underlies the classical theory plasticity [48].

Calibration from MD data

We proceed to use the data mined from MD, Section 2.2, to specialize the general framework just outlined to fused silica glass and calibrate the resulting model.

Elasticity

For definiteness, we consider elastic strain-energy densities of the neo-Hookean form

$$W^e(\boldsymbol{C}^e) = \frac{\mu(J^e)}{2}\big(J^{e-2/3}\mathrm{tr}(\boldsymbol{C}^e) - 3\big) + f(J^e), \tag{2.16}$$

where $\mu(J^e)$ is a volume-dependent shear modulus and $f(J^e)$ defines the volumetric equation of state. The Cauchy stress follows from (2.16) as

$$\begin{aligned} J\boldsymbol{\sigma} = 2\boldsymbol{F}^e\frac{\partial W^e}{\partial \boldsymbol{C}^e}\boldsymbol{F}^{eT} = &\Big(\frac{1}{2}\mu'(J^e)(J^{e-2/3}\mathrm{tr}(\boldsymbol{B}^e) - 3) + f'(J^e)\Big)\, J^e\boldsymbol{I} \\ &+ \mu(J^e)\Big(J^{e-2/3}\boldsymbol{B}^e - \frac{1}{3}J^{e-2/3}\mathrm{tr}(\boldsymbol{B}^e)\boldsymbol{I}\Big), \end{aligned} \tag{2.17}$$

where

$$\boldsymbol{B}^e = \boldsymbol{F}^e\boldsymbol{F}^{eT} \tag{2.18}$$

is the elastic left Cauchy-Green deformation tensor.

We identify the Jacobian J from the molecular dynamics data in figure 2.5 as the ratio of the current volume to the initial volume. In addition, we compute J^p as the ratio of the final volume upon unloading divided by the initial volume and set $J^e = J/J^p$. The molecular dynamics data suggests a densification phase transition when the plastic volumetric deformation attains a critical value of $J^p = J^p_c \approx 0.9$, Fig. 2.14a. We therefore regard glass as a two-phase material and describe the elasticity of each phase by means of an elastic strain-energy density of the form (2.16). Specializing (2.17) to simple elastic shear following a volumetric plastic deformation gives

$$J\sigma_{12} = \mu(J^e)\gamma, \tag{2.19}$$

(a) (b)

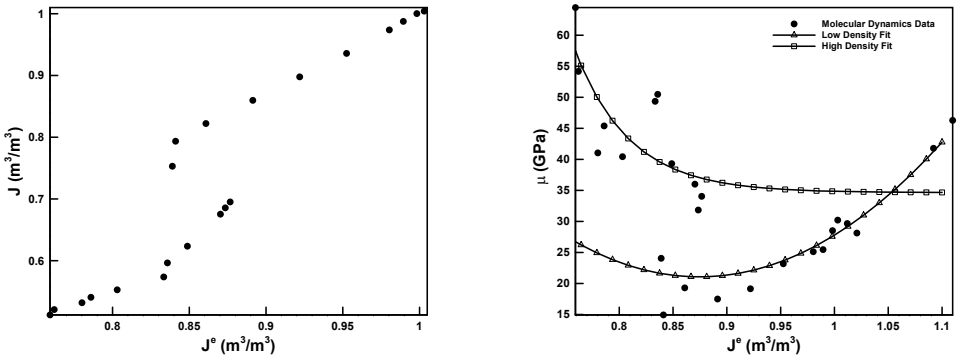

Figure 2.14: Volumetric MD data during monotonic compressive loading. a) Total volumetric Jacobian J *vs.* elastic Jacobian J^e as deduced from unloading, showing two phases (dense and loose) separated by a densification phase transition. b) Shear modulus μ *vs.* J^e and fit of each of the phases.

in axes aligned with the shearing directions and with γ denoting the shear strain. Using this relation in combination with the MD data in Fig. 2.9a gives the μ *vs.* J^e data shown in Fig. 2.14b. For definiteness, we fit these data by functions of the form

$$\mu(J^e) = \begin{cases} a_0 + a_1 J^e + a_2 J^{e^2}, & J^p \geq J_c^p, \\ b_1 \exp(b_2(J^e - 1)) + b_3, & \text{otherwise}, \end{cases} \tag{2.20}$$

and obtain the coefficients tabulated in Table 2.1. The goodness of the fit is shown in Fig. 2.14b. The two-phase structure of the equation of state is also clear from the figure.

Table 2.1: Pressure-dependent shear-modulus parameters

a_0	a_1	a_2	b_1	b_2	b_3
347.15 GPa	-745.82 GPa	426.46 GPa	0.20773 GPa	-19.498	34.6439 GPa

Next, we determine the equation-of-state function $f(J^e)$ in eq. (2.16) by examining the case of pure elastic compression. Specializing (2.17) to this case, we obtain the relation

$$-Jp = f'(J^e)J^e. \tag{2.21}$$

In this particular case, the MD data of Fig. 2.5 reduces to Fig. 2.15a. We fit these

(a) (b)

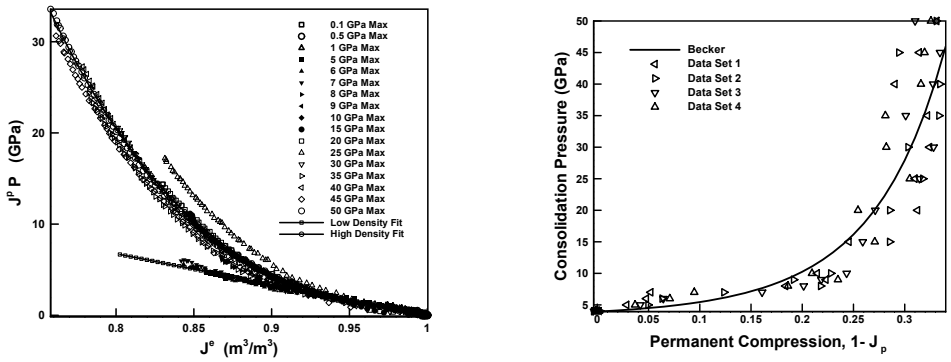

Figure 2.15: Consolidation MD data during monotonic compressive loading. a) Pressure p *vs*. elastic Jacobian J^e and fits for dense and loose phases. b) Preconsolidation pressure p_c on permanent densification $1 - J^p$ and fit.

data by functions of the form

$$f(J^e) = \begin{cases} \dfrac{c}{2}(J^e - 1)^2, & J^p \geq J_c^p, \\ \dfrac{d_1}{2}(J^e - 1)^2 + \dfrac{d_2}{4}(J^e - 1)^4, & \text{otherwise}, \end{cases} \tag{2.22}$$

and obtain the coefficients tabulated in Table 2.2. The goodness of the fit is also shown in Fig. 2.15b.

Table 2.2: Volumetric elastic-energy dependence

c	d_1	d_2
-33.75 GPa	-25.167 GPa	-1879.69 GPa

Elastic domain and yield surface

Under the assumption of rate independence, we model the yield-behavior of glass by means of the elliptic elastic domain

$$E(J^p) = \left\{ \boldsymbol{y} \in \mathbb{R}^{3\times3}_{sym},\ \left(\frac{q}{q_c(J^p)}\right)^2 + \left(\frac{p - (p_c(J^p) + p_t)/2}{(p_c(J^p) - p_t)/2}\right)^2 \leq 1 \right\}, \tag{2.23}$$

where

$$q = \sqrt{\frac{1}{2}\boldsymbol{s} \cdot \boldsymbol{s}} \tag{2.24}$$

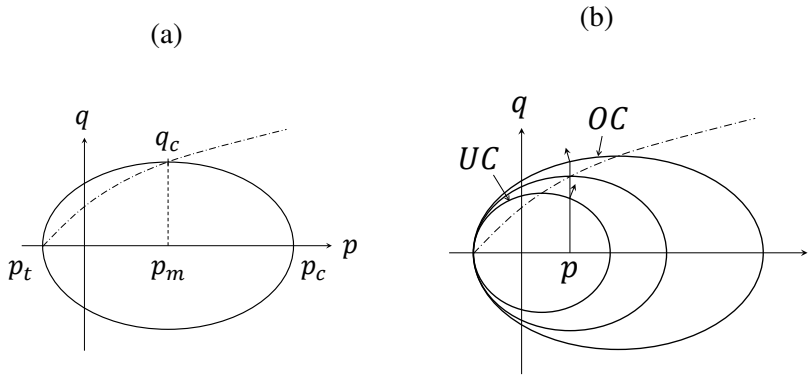

Figure 2.16: a) Schematic of elastic domain in the (p, q)-plane, where p denotes the pressure, q the Mises effective shear stress, p_t the tensile failure pressure, p_c the compressive yield pressure and q_c the shear yield strength. The dash-dot line represents the critical-state line. b) Stress path for pressure-shear test (vertical line at p) and directions of plastic deformation rate (arrows) in the over-consolidated case, labeled OC, and under-consolidated case, labeled UC.

is the Mises effective shear stress,

$$\boldsymbol{s} = \boldsymbol{\sigma} - \frac{1}{3}\mathrm{tr}(\boldsymbol{\sigma})\,\boldsymbol{I} = \boldsymbol{y} - \frac{1}{3}\mathrm{tr}(\boldsymbol{y})\,\boldsymbol{I} \tag{2.25}$$

is the stress deviator, p_t is the tensile failure pressure, p_c is the compressive yield pressure, q_c is the shear yield strength, and J^p plays the role of an internal variable, cf. Fig. 2.16a. Elastic domains of the type (2.23) have been used in connection to Cam-Clay models of granular media [62] and glasses [26, 34, 54]. The function $p_c(J^p)$ defines the *consolidation relation*. The curve in the (p, q)-plane

$$q_c = g(p_m), \tag{2.26}$$

with

$$p_m = \frac{p_t + p_c}{2} \tag{2.27}$$

may be obtained by eliminating J^p between $q_c(J^p)$ and $p_c(J^p)$. Evidently, p_m is the pressure at which q attains its maximum value q_c on the yield surface $\partial E(J^p)$, cf. eq. (2.23), and at which, by the flow rule (2.15), the plastic strain rate is volume preserving. Thus, the relation (2.26) represents the *critical state line* in the (p, q)-plane.

Consolidation curve

We proceed to identify the consolidation curve $p_c(J^p)$ for fused silica from the MD data shown in Fig. 2.5. To this end, we identify J^p as the volumetric deformation

upon unloading and the corresponding $p_c(J^p)$ as the maximum pressure attained during loading. The resulting data are shown in Fig. 2.14b. We fit these data by means of a power-law relation of the form

$$p_c = p_0 + \frac{A}{\alpha}(1 - J^{p-\alpha}), \tag{2.28}$$

previously used by [7] as a volumetric equation of state. In addition, we identify the tensile failure stress p_t from MD calculations as the maximum tensile pressure at which the glass sample is stable. The resulting values of the constants are tabulated in Table 2.3. The goodness of the fit is shown in Fig. 2.14b.

Table 2.3: Hardening parameters

A	α	p_0	p_t
-8.48613 GPa	9.2689	3.02934 GPa	−8.5 GPa

Evolution towards the critical state

We verify that a simple elastic domain of the form (2.23) and the consolidation curve (2.28) are indeed capable of representing the complex yield and flow behavior revealed by the pressure-shear MD data collected in Section 2.2. Thus, consider a pressure-shear test at confining pressure p and effective shear stress q increasing monotonically from zero. The corresponding loading path is shown as a vertical line at p in Fig. 2.16b. The intermediate ellipse in the figure corresponds to the critical state that is eventually attained along the loading path. The figure also depicts two cases, labeled 'under-consolidated' (UC) and 'over-consolidated' (OC). In the under-consolidated case, p lies to right of the initial value of p_m, resulting in a plastic strain rate $\boldsymbol{d}^p$ (shown as an arrow in the figure) with a negative, or compressive, volumetric component, $\mathrm{tr}(\boldsymbol{d}^p) < 0$.[1] By contrast, in the over-consolidated case, p lies to left of the initial value of p_m, resulting in a plastic strain rate $\boldsymbol{d}^p$ (also shown as an arrow in the figure) with a positive, or tensile, volumetric component, $\mathrm{tr}(\boldsymbol{d}^p) > 0$. It thus follows that under-consolidated samples are predicted to decrease their volume, whereas over-consolidated samples are predicted to increase their volume, in accord with the MD data in Fig. 2.12. From relation (2.10), it follows that

$$\dot{J}^p = J^p \,\mathrm{tr}(\boldsymbol{d}^p), \tag{2.29}$$

[1] We recall that, under the pressure sign convention $p = -\mathrm{tr}(\boldsymbol{\sigma})$, a positive (negative) component of the normal to the yield surface in the (p, q)-plane corresponds to a negative (positive), or compressive (tensile), volumetric plastic strain, $\mathrm{tr}(\boldsymbol{d}^p) < 0$ ($\mathrm{tr}\boldsymbol{d}^p) > 0$).

and from the monotonicity of the consolidation curve, Fig. 2.14b, it follows that p_c increases in the under-consolidated case and decreases in the over-consolidated case. Thus, in both cases the yield surface converges towards the critical-state yield surface, as required. We also note that, following the attainment of the critical state, represented by the intermediate ellipse in Fig. 2.17b, both the sample volume and the shear stress remain constant, in agreement with the MD data collected in Fig. 2.12 and Fig. 2.13. We therefore conclude that the MD data for fused silica presented in Section 2.2 is indicative of—and well-represented by—critical state theory of plasticity.

The anomalous critical-state line of fused silica

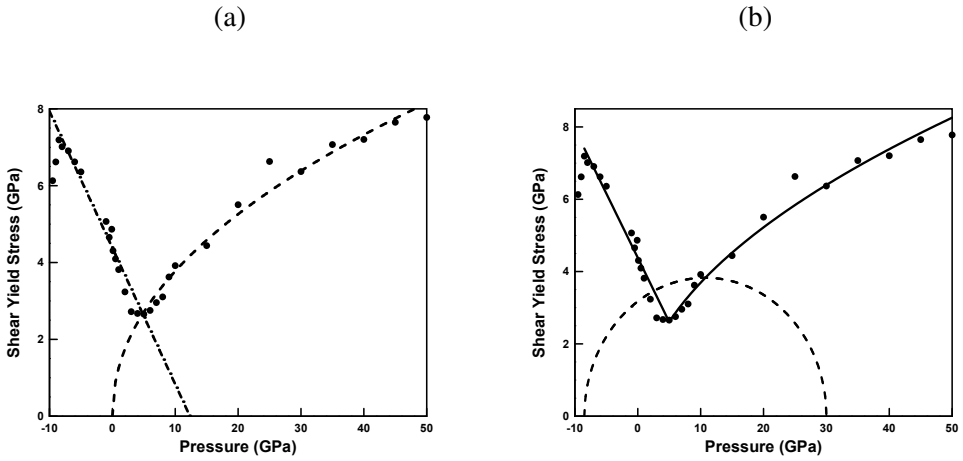

Figure 2.17: a) Critical state line MD data (dots) and fits. The dash line is the fit in the compressive regime and the dash-dot line is the fit in the tensile regime. b) Critical state line (solid curve) obtained by intersecting the compressive and tensile critical state lines. The dash line represents a typical elastic domain.

In order to close the model, the critical state line (2.26) remains to be identified. We determine the critical state line, eq. (2.26), from the MD simulations described in Section 2.2, by identifying p_m with the confining pressure applied to the sample and the corresponding q_c with the shear stress upon the attainment of the critical state of constant volume.

The data thus obtained is shown in Fig. 2.17a. The critical-state line thus determined exhibits two clear regimes, one under predominantly compressive pressures and another under predominantly tensile pressures. Remarkably, *in the tensile regime the critical-state line increases with increasing tensile pressure*, which represents

anomalous behavior. By contrast, in the compressive regime the critical-state line increases with increasing compressive pressure, or confinement, as expected.

The tensile regime of the critical-state line is well-represented by a linear relation of the form

$$q = \frac{p_1 - p}{p_1 - p_t}\, q_t, \tag{2.30}$$

capped vertically at $p = p_t$. The compressive regime of the critical-state line is in turn well-presented by a power law of the form

$$q = Bp^{\beta}. \tag{2.31}$$

The resulting values of the constants are tabulated in Table 2.4. The goodness of the fit is shown in Fig. 2.17a.

Table 2.4: Critical state line constants

p_1	q_t	p_t	B	β
12.337 GPa	7.402 GPa	−8.5 GPa	1.168 $\sqrt{\text{GPa}}$	0.5

The anomalous yield behavior of fused silica under predominantly tensile pressures uncovered by the MD data is indeed consistent with the experimental data of [57] noted in the introduction, Fig. 2.1b, who attributed the anomaly to changes in coordination at the atomic level. Interestingly, [57] observe an additional region of anomalous shear yield strength behavior at pressures above 30 GPa, not captured by the present MD calculations. Likely causes of this discrepancy are the large disparity in strain rates between the work of [57], which was performed at quasi-static loading rates, and the present calculations, which entail large rates of deformation, and possible inadequacies of the interatomic potentials at extremely large pressures and volume reductions.

The intersection of the tensile and compressive critical state lines, eq. (2.30) and (2.31), respectively, results in a *non-convex* combined critical-state line, Fig. 2.17b. The figure reveals that fused silica is doubly anomalous, on account of the anomalous dependence of the its shear modulus of volumetric deformation, and of the strong non-convexity of its critical-state line.

2.4 Microstructure, relaxation, and div-quasiconvexification

We now proceed to show that the strongly non-convex critical-state line in Fig. 2.17b is, in fact, unstable with respect to microstructure formation and that consideration

of microstructure results in a stable, or *relaxed*, critical-state line that captures the fine structure of the MD data at the tensile-to-compressive transition. We recall that, as noted in the introduction, several authors [42, 53] have performed molecular dynamics calculations on amorphous solids deforming under shear and found that the resulting deformation field develops fine microstructure in order to accommodate permanent macroscopic deformations, Fig. 2.2. In this section, we appeal to notions from the Direct Methods in the Calculus of Variations in order establish a connection between the strong non-convexity of the critical-state line and the development of fine microstructure, and to characterize explicitly and exactly the effective or relaxed behavior at the macroscale. For completeness, a summary of the main mathematical concepts and arguments is consigned to the Appendix. A full mathematical account may be found in the article of [15].

We carry out the analysis within the framework of limit analysis [48]. Thus, we assume that the solid is at *collapse*, i.e., it deforms plastically at constant applied load. Under these conditions, the instantaneous behavior of the solid is rigid and ideally plastic, i.e., no instantaneous hardening takes place (ideal plasticity) and (rigid-plastic behavior)

$$\boldsymbol{d}^p = \frac{1}{2}(\nabla \boldsymbol{v} + \nabla \boldsymbol{v}^T) \equiv \boldsymbol{e}(\boldsymbol{v}), \tag{2.32}$$

where $\boldsymbol{v} : \Omega \to \mathbb{R}^3$ is the velocity field at collapse, or collapse mode, and Ω is the domain of the solid at collapse. The corresponding kinematic and static problems of limit analysis [48] can then be jointly expressed as the saddle-point problem

$$\inf_{\boldsymbol{v}} \sup_{\boldsymbol{\sigma}} \left\{ \int_\Omega \boldsymbol{\sigma} \cdot \nabla \boldsymbol{v} \, dx \; : \; \boldsymbol{\sigma}(x) \in E(J^p(x)), \; \boldsymbol{v} = \boldsymbol{g} \text{ on } \partial\Omega \right\}, \tag{2.33}$$

where the minimization and maximization take place over suitable spaces of velocities and stresses, respectively, J^p accounts for the state of consolidation of the solid, $\boldsymbol{g}$ is a prescribed velocity field over the boundary and we assume that the solid is free of body forces. We recall that the inner maximum problem in (2.33) embodies Drucker's principle of maximum dissipation and the static principle of classical plasticity, whereas the outer minimum problem embodies the kinematic principle of classical plasticity.

We further note that, for a solid obeying critical-state theory of plasticity, instantaneous rigid-ideally plastic behavior implies, in particular, instantaneous constancy of volume, which in turn requires that the solid be either locally rigid or at critical state. This condition sets the requirement that $\sigma(x) \in K$ a. e. in Ω, where K is the domain bounded by the critical-state line. Since the critical-state line is the locus

of points in stress space at which material behavior is ideally plastic, K may be regarded as a *limit domain* in the sense of hardening plasticity (cf., e. g., [56] for a lucid introduction to limit surfaces in hardening plasticity). Thus, at collapse (2.33) specializes to

$$\inf_{\boldsymbol{v}} \sup_{\boldsymbol{\sigma}} \Big\{ \int_\Omega \boldsymbol{\sigma} \cdot \nabla \boldsymbol{v} \, dx \ : \ \boldsymbol{\sigma}(x) \in K, \ \boldsymbol{v} = \boldsymbol{g} \text{ on } \partial\Omega \Big\}, \tag{2.34}$$

The maximization with respect $\boldsymbol{\sigma}$ may be effected pointwise, whereupon the problem (2.34) reduces to the kinematic problem

$$\inf_{\boldsymbol{v}} \Big\{ \int_\Omega \phi(\boldsymbol{e}(\boldsymbol{v})) \, dx \ : \ \ \boldsymbol{v} = \boldsymbol{g} \text{ on } \partial\Omega \Big\}, \tag{2.35}$$

where

$$\phi(\boldsymbol{d}^p) = \sup_{\boldsymbol{\sigma} \in K} \boldsymbol{\sigma} \cdot \boldsymbol{d}^p \tag{2.36}$$

is the limit plastic dissipation potential.

This classical theory of limit analysis is mathematically well-developed provided that the limit domain K is *convex*, in which case no microstructure occurs. In order extend the theory to non-convex domains and microstructure formation, we reformulate the saddle-point problem (2.34) as

$$\sup_{\boldsymbol{\sigma}} \inf_{\boldsymbol{v}} \Big\{ \int_\Omega \boldsymbol{\sigma} \cdot \nabla \boldsymbol{v} \, dx \ : \ \boldsymbol{\sigma} \in K, \ \boldsymbol{v} = \boldsymbol{g} \text{ on } \partial\Omega \Big\}, \tag{2.37}$$

where we have simply inverted the order of the maximum and minimum problems. We recall that, in the convex case, problems (2.37) and (2.34) are equivalent by the inf-sup theorem [21], but not so in the non-convex case. An integration by parts gives (2.37) in the equivalent form

$$\sup_{\boldsymbol{\sigma}} \inf_{\boldsymbol{v}} \Big\{ \int_{\partial\Omega} \boldsymbol{\sigma} \nu \cdot \boldsymbol{g} \, d\mathcal{H}^2 - \int_\Omega \mathrm{div} \boldsymbol{\sigma} \cdot \boldsymbol{v} \, dx \ : \ \boldsymbol{\sigma} \in K, \ \boldsymbol{v} = \boldsymbol{g} \text{ on } \partial\Omega \Big\}, \tag{2.38}$$

where $d\mathcal{H}^2$ denotes the element of area on the boundary $\partial\Omega$. Evidently, for the supremum to be non-trivial we must have $\mathrm{div}\, \boldsymbol{\sigma} = \boldsymbol{0}$, i. e., the stress field must be in equilibrium, whereupon (2.38) reduces to the static problem

$$\sup_{\boldsymbol{\sigma}} \Big\{ \int_{\partial\Omega} \boldsymbol{\sigma} \nu \cdot \boldsymbol{g} \, d\mathcal{H}^2 \ : \ \boldsymbol{\sigma} \in K, \ \mathrm{div} \boldsymbol{\sigma} = \boldsymbol{0} \Big\}. \tag{2.39}$$

The question of existence of solutions of problem (2.39) may be ascertained by recourse to the direct method of the Calculus of Variations [16]. Existence of solutions is indicative of *stability* of the material with respect to microstructure.

Stability in turn necessitates some appropriate notion of convexity to be satisfied by the limit domain K. In the present setting, the appropriate notion is *symmetric* div*-quasiconvexity* [15, 25], cf. Appendix A, a notion of convexity in symmetric stress space that accounts for the equilibrium constraint d$iv\boldsymbol{\sigma} = \mathbf{0}$.

Equally as important as establishing existence is the treatment of cases that depart from the preceding program, specifically, solids for which K fails to be symmetric div-quasiconvex. In such cases, the supremum in (2.39) may be attained arbitrarily closely by weakly-convergent sequences of stress fields, but the supremum itself may not be attained by any one stress field. The weakly-convergent maximizing sequences are typically characterized by increasingly fine microstructure, a situation reminiscent of the fine patterns computed by [53]. The weak limits of the maximizing sequences can then be identified as the macroscopically observable, or average, stress fields. The problem is, then, to characterize all macroscopic stress fields that are attainable as weak limits of sequences of maximizing microscopic stress-field sequences. This characterization determines the effective yield behavior of the solid at the macroscale.

Based on standard theory [16] we expect that the macroscopic states thus defined satisfy the *relaxed problem*

$$\sup_{\boldsymbol{\sigma}} \left\{ \int_{\partial\Omega} \boldsymbol{\sigma}\boldsymbol{\nu} \cdot \boldsymbol{g}\, d\mathcal{H}^2 \;:\; \boldsymbol{\sigma} \in \bar{K},\ \mathrm{d}iv\boldsymbol{\sigma} = 0 \right\}, \tag{2.40}$$

for some effective limit domain $\bar{K}$. Evidently, $\bar{K}$ must contain K and be symmetric div-quasiconvex in order for the supremum of the effective problem (2.40) to be attained. In addition, $\bar{K}$ must be as small as possible in order for the solutions of the effective problem (2.40) to be weak limits of maximizing sequences of the unrelaxed problem (2.39). These constraints identify $\bar{K}$ as the symmetric div-quasiconvex envelope of K, and can be visualized as the smallest symmetric div-quasiconvex set containing K.

The remaining problem of interest is to determine the symmetric div-quasiconvex envelope $\bar{K}$ of the limit surface of fused silica, eqs. (2.30) and (2.31), Fig. 2.17. An explicit and exact construction of $\bar{K}$ has been derived by [15]. They show that the curves

$$q = \left(s + \frac{3}{4}(p - r)^2 \right)^{1/2} \tag{2.41}$$

in (p, q)-plane represent rank-2 connections between states of constant stress in traction equilibrium, and that the curves bound symmetric div-quasiconvex sets in

the (p, q)-plane. Evidently, the smallest such set containing K, or *rank*-2 *envelope* of K, contains $\bar{K}$. The mathematical challenge is to show that the rank-2 envelope of K is in fact $\bar{K}$. This equivalence has been proven by [15].

Specifically, the rank-2 envelope of the limit domain K for fused silica is obtained by fitting a curve of the form (2.41) so as to smooth out the transition between the tensile and compressive regimes of the critical-state line. The conditions that determine the extreme rank-2 connection are

$$\sqrt{s + \frac{3}{4}(p_{\min} - r)^2} = \frac{p_1 - p_{\min}}{p_1 - p_{\min}} q_t \,, \tag{2.42a}$$

$$-\frac{q_t}{p_{\min}} = \frac{1}{q}\frac{3}{4}(p_{\min} - r) \,, \tag{2.42b}$$

$$\sqrt{s + \frac{3}{4}(p_{\max} - r)^2} = B p_{\max}^{\beta} \,, \tag{2.42c}$$

$$\beta B p_{\max}^{\beta - 1} = \frac{1}{q}\frac{3}{4}(p_{\max} - r) \,, \tag{2.42d}$$

to be solved for r, s, $p_{\min}$ and max. The values of these variables computed from Tables 4.4 and 2.4 are shown in Table 2.5.

Table 2.5: The rank-2 envelope of fused silica glass.

r	s	$p_{\mathrm{m}in}$	$p_{\mathrm{m}ax}$
5.176 GPa	7.674 GPa^2	4.141 GPa	6.084 GPa

The resulting envelope is shown in Fig. 2.18a. It bears emphasis that the relaxed limit domain $\bar{K}$ is not convex, which illustrates the fact that symmetric div-quasiconvex sets are a strictly larger class than convex sets. We also note that $\bar{K} \neq K$, which shows that, indeed, K is not symmetric div-quasiconvex, or stable against microstructure, as surmised. Fig. 2.18b shows the rank-2 connection curve in isolation together with the MD data. The comparison suggests that the rank-2 envelope construction indeed captures the fine structure of the MD data at the tension-to-compression transition point, which, in hindsight, the unrelaxed model in Fig. 2.17 fails to do. Conversely, we conclude that the fine structure of the MD data at the tension-to-compression transition point is the result of accommodation at the microstructural level.

Specifically, the way in which the material attains the relaxed limit domain $\bar{K}$ is by developing mixed states of stress that combine fine regions of tensile and compressive pressure. These mixed states of stress are in equilibrium and average to points (p, q) outside the unrelaxed limit domain K.

(a) (b)

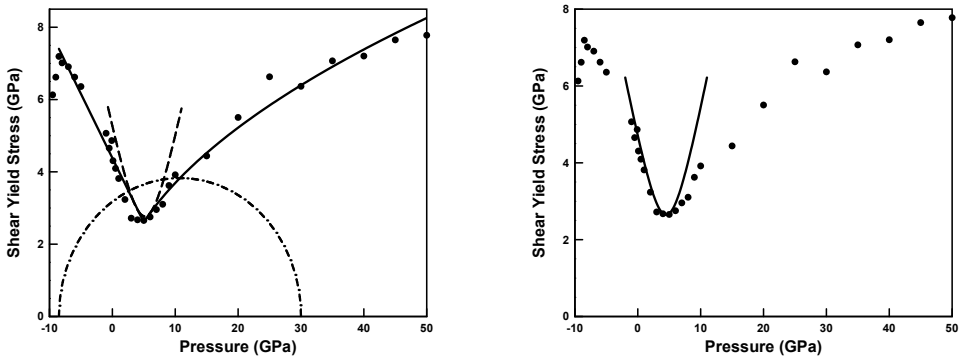

Figure 2.18: a) Relaxed critical-state line showing rank-2 connection envelope (dash line). b) Rank-2 connection captures the fine structure of the MD data at the tension-to-compression transition point.

With the benefit of hindsight, we may indeed uncover these mixed states in the molecular dynamics calculations. To this end, we revisit the pressure-shear calculations and bin the per-atom pressures on layers parallel to the shear plane (cf. [92] for an in-depth description of per-atom stresses). Fig. 2.19 shows the resulting histograms of pressure vs. transverse coordinate for a confining pressure of $p = 5$ GPa, roughly corresponding to the reentrant corner of K separating the tensile and the compressive parts of the critical state line. We partition the RVE into 5, 10, 15, and 20 bins in order to obtain a sequence of increasingly finer mixed states.

As expected from theory, the highly oscillatory nature of the mixed states of stress is clearly evident in Fig. 2.19 . The pressure oscillates between tensile and compressive states on both sides of the average pressure of 5 GPa. The distribution of binned stresses relative to the unrelaxed critical stress line is shown in Fig. 2.20 (a) for the case of 20 bins. In this representation, most of the points fall within the unrelaxed limit surface with a few of the points falling outside. The limit of refinement of individual per-atom stresses is shown in Fig. 2.20 (b). In this representation, the data exhibits a clear clustering into tensile and compressive states, revealing that the mixed states of stress responsible for accommodation are, in this case, bimodal.

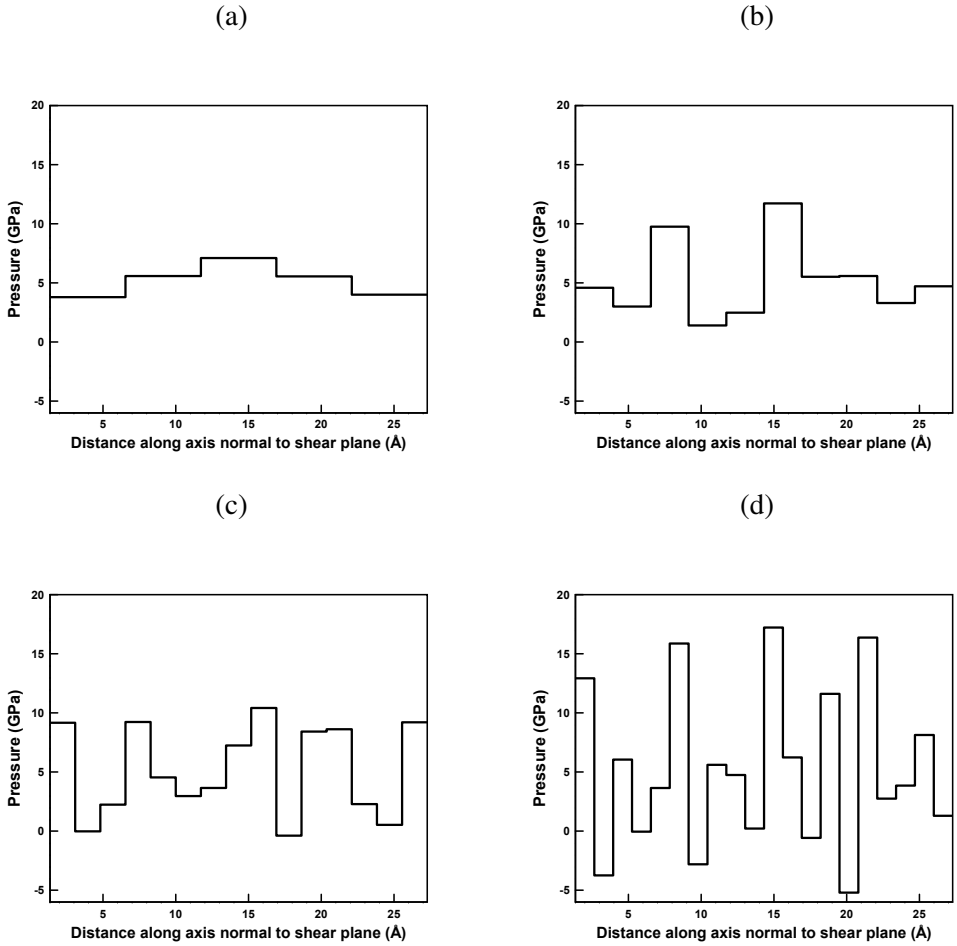

Figure 2.19: We examine averages of pressure over a cross sections of the RVE as viewed along the shear axis.

(a) (b)

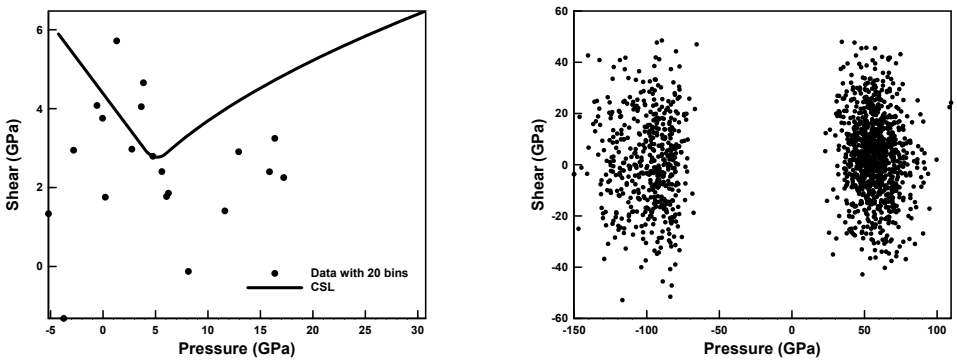

Figure 2.20: a) We plot shear versus pressure for the case considered above with 20 bins. b) In the limit, atom-wise stresses exhibit a clear partition into tensile and compressive pressures.

2.5 Summary and concluding remarks

We have developed a critical-state model of fused silica plasticity on the basis of data mined from Molecular Dynamics (MD) calculations. The MD data is suggestive of an irreversible densification transition in volumetric compression resulting in permanent, or plastic, densification upon unloading. The MD data also reveals an evolution towards a critical state of constant volume under pressure-shear deformation. The trend towards constant volume is from above, when the glass is overconsolidated, or from below, when it is underconsolidated. We have shown that these characteristic behaviors are well-captured by a critical-state model of plasticity, where the densification law for glass takes the place of the classical consolidation law of granular media and the locus of constant-volume states defines the critical-state line.

A salient feature of the critical-state line of fused silica, as identified from MD data, that renders its yield behavior anomalous—and raises it from the commonplace—is that it is strongly non-convex, owing to the existence of two well-differentiated phases, at low and high pressures. This anomalous yield strength of fused silica is indeed consistent with—and born out by—the measurements of [57]. The strong non-convexity of yield in turn explains the patterning observed by [53] in molecular dynamics calculations of amorphous solids deforming in shear.

The proclivity of fused silica for patterning at the microscale raises the question of its effective behavior at the macroscale, i. e., the average stress and deformation conditions that are attainable when microstructure is accounted for. Remarkably, this question can be rigorously and exactly ascertained for fused silica within the framework of limit analysis and the calculus of variations [15]. We recall that stress solutions of the static problem of limit analysis are subject to an equilibrium, or divergence, constraint. The problem is, therefore, to determine all macroscopic states of stress attainable as averages of microscopic stress fields that are within yield and at equilibrium. [15] have shown that the effective or macroscopic critical-state line thus defined can be computed explicitly and exactly through a rank-2 envelope construction in the (p,q)-plane. This remarkable result effectively *upscales* the microscopic critical state model delineated by the MD data to the macroscale. The rank-2 envelope indeed captures the fine structure of the critical-state line, as gleaned from MD data, at the tension-to-compression transition, which further underscores the importance of microstructure in shaping the macroscopic, or effective, behavior of fused silica. The effective or macroscopic model of fused silica is stable

with respect to microstructure, defines well-posed boundary-value problems and is, therefore, suitable for use in large-scale continuum calculations.

Acknowledgements

We gratefully acknowledge support from the US Office of Naval Research through grant N000141512453.

Chapter 3

OPTIMAL TRANSPORT MESHFREE ANALYSIS OF THE IMPACT OF GLASS RODS

Research presented in this chapter has been adapted from [79].

3.1 Introduction

The inelastic behavior of Silica glass has been a long-standing topic of investigation yet has left open questions regarding general constitutive behavior. Salient extraordinary behaviors include the anomalous shear moduli behavior [35], anomolous yield behavior [78], and the exhibition of failure waves [9] – the rapid fragmentation of a material behind a traveling high pressure region. Kondo *et al.* [35] and references therein examined the non-monotonic dependence of the elastic moduli on pressure for fused quartz. Notably, between 0 and 2.5 GPa, the shear modulus and bulk modulus decreases. Likewise, the anomalous pressure dependence of the strength of amorphous silica has also received some attention due to the investigators Meade and Jeanloz [57] who made measurements of the yield strength at pressures up to 81 GPa at room temperature and showed that the strength of amorphous silica decreases significantly as it is compressed to denser structures with higher coordination. Clifton *et al.* [1, 12, 90] and Gupta [84] investigated the effect of pressure on failure waves in silica and soda-lime glass through angled flyer plate impact experiments and observed a loss of shear strength as the failure wave passed through the glass at pressures of 4-6 GPa.

There has been some previous effort in modeling amorphous silica glass from a continuum perspective. Kermouche and coworkers [34] proposed a plasticity model with a yield surface involving volumetric terms to capture the permanent densification observed experimentally. They furthermore performed a nano-indentation test to compare to experimental procedures. Holmquist and coworkers [27] formulated a phenomenological constitutive model to capture the high strain rate behavior of Silica glass with a particular interest in surface effects. Recently, a variational constitutive model was derived from molecular dynamics data to characterize the deformation behavior of SiO2 glass at at high strain rates [78]. In particular, the authors implemented a multiscale modeling program in which stress-strain data sets were generated. This data was mined to inform a simple constitutive law, borrowing

notions from Cam Clay theories to capture the extensive volumetric plasticity observed in the molecular dynamics data sets. Remarkably, the resulting limit surface is not convex, but is, in fact, *symmetric div-quasiconvex* [14, 78]. In a restricted setting, this can be shown to be a necessary and sufficient condition for existence of solutions in plasticity [14].

The goals of this paper are two-fold. First, we report a first detailed continuum calculations of this model for Silica glass using the *optimal transport meshfree* [43] method and find that it performs quite well with fidelity to existing MD data. Second, we report a strong characterization of failure waves in glass bars as compared to experiments by Brar et al. [9] with no fitting to these results the elastic or plastic parameters which were all previously derived from MD data.

3.2 Variational Constitutive Updates in Finite Deformations

We consider a body $\Omega \subset \mathbb{R}^3$ and a deformation mapping $\varphi : \Omega \to \mathbb{R}^3$. The body deforms under the action of body forces B and tractions $\bar{t}$ on $\partial\Omega_2$ subject to Dirichlet boundary conditions on $\partial\Omega_1$. The deformation gradient is $\boldsymbol{F} = \boldsymbol{\nabla}\varphi$ and the right Cauchy-Green tensor is $\boldsymbol{C} = \boldsymbol{F}^T\boldsymbol{F}$. We specify a constitutive law by an objective free energy

$$W = W(\boldsymbol{C}, T, Q)\,, \tag{3.1}$$

where T is the temperature and Q is a list of internal variables describing changes in the microstructure. The Piola Kirchoff tensor follows from the Coleman Noll equilibrium relations

$$\boldsymbol{P} = \frac{\partial W}{\partial \boldsymbol{F}}\,. \tag{3.2}$$

Conservation of momentum is

$$\boldsymbol{\nabla}\cdot\boldsymbol{P} + RB = RA\,. \tag{3.3}$$

The evolution of the internal variables is specified via the kinetic relation

$$0 \in \frac{\partial W}{\partial Q} + \frac{\partial \psi^*}{\partial \dot{Q}}\,, \tag{3.4}$$

where $\psi^*(\dot{Q})$ known as the *dissipation function* (or *dual kinetic potential*) specifies the rate dependency of the problem. Equivalently equation (3.4) may be placed in a minimization form

$$\dot{Q} \in \arg\inf\{\dot{W} + \psi^*\}\,. \tag{3.5}$$

Discretizing $\dot{W} = \dfrac{W_{\alpha+1} - W_\alpha}{\Delta t}$ where $W_\alpha := W(\boldsymbol{C}_\alpha, Q_\alpha)$, we obtain an incremental variational constitutive update

$$Q_{\alpha+1} \in \arg\inf_{Q_{\alpha+1}} \{W(\boldsymbol{C}_{\alpha+1}, Q_{\alpha+1}) + \Delta t \psi^*(\frac{Q_{\alpha+1} - Q_\alpha}{\Delta t})\} \ . \tag{3.6}$$

Defining

$$\mathcal{F}_{\alpha+1}(Q_{\alpha+1}; \boldsymbol{C}_{\alpha+1}, Q_\alpha) := W(\boldsymbol{C}_{\alpha+1}, Q_{\alpha+1}) + \Delta t \psi^*(\frac{Q_{\alpha+1} - Q_\alpha}{\Delta t}) \, ,$$

we realize that $\mathcal{F}^{\alpha+1}$ furnishes an incremental stress potential, i.e.,

$$\boldsymbol{P}_{\alpha+1} = \frac{\partial W_{\alpha+1}}{\partial \boldsymbol{F}_{\alpha+1}} = \frac{\partial \mathcal{F}_{\alpha+1}}{\partial \boldsymbol{F}_{\alpha+1}} \ . \tag{3.7}$$

3.3 Rate Independent Cam Clay Constitutive Model for Amorphous Silica Glass

variational cam clay plasticity

We begin by briefly reviewing the constitutive modeling recently introduced by Schill et al. [78] of Amorphous Silica Glass as derived from molecular dynamics modeling. We begin by assuming the multiplicative decomposition holds for the deformation gradient tensor $\boldsymbol{F} = \boldsymbol{F}^e \boldsymbol{F}^p$. For specificity, we take the set of internal variables to be $Q_{\alpha+1} = \boldsymbol{F}^p_{\alpha+1}$. Further, we assume that the stored energy occurs via permanent volumetric deformation as described by $J^p = \det(\boldsymbol{F}^p)$ and that the free energy admits the additive decomposition

$$W = W^e(\boldsymbol{C}^e) + W^p(J^p) \ . \tag{3.8}$$

The stationarity condition corresponding to equation (3.6) is

$$0 \in \frac{\partial W_e^{\alpha+1}}{\partial \boldsymbol{C}^e_{\alpha+1}} \frac{\partial \boldsymbol{C}^e_{\alpha+1}}{\partial \boldsymbol{F}^p_{\alpha+1}} + \frac{\partial W^p_{\alpha+1}}{\partial J^p_{\alpha+1}} \frac{\partial J^p_{\alpha+1}}{\partial \boldsymbol{F}^p_{\alpha+1}} + \psi^{*'}(\frac{\boldsymbol{F}^p_{\alpha+1} - \boldsymbol{F}^p_\alpha}{\Delta t}) \, , \tag{3.9}$$

and the following simplifications may be made:

$$\frac{\partial W^e_{\alpha+1}}{\partial \boldsymbol{C}^e_{\alpha+1}} \frac{\partial \boldsymbol{C}^e_{\alpha+1}}{\partial \boldsymbol{F}^p_{\alpha+1}} = -2\boldsymbol{C}^e_{\alpha+1} \frac{\partial W^e_{\alpha+1}}{\partial \boldsymbol{C}^e_{\alpha+1}} \boldsymbol{F}^{p^{-T}}_{\alpha+1} \, , \tag{3.10}$$

and

$$\frac{\partial W^p_{\alpha+1}}{\partial J^p_{\alpha+1}} \frac{\partial J^p_{\alpha+1}}{\partial \boldsymbol{F}^p_{p+1}} = J^p_{\alpha+1} \frac{\partial W^p_{\alpha+1}}{\partial J^p_{\alpha+1}} (\boldsymbol{F}^p_{\alpha+1})^{-1} \ . \tag{3.11}$$

The specific material model free energy following our earlier work in Silica glass

$$-\frac{J^p}{J} \frac{\partial W^p}{\partial J^p} = p_0 + \frac{A}{\alpha}(1 - (J^p)^\alpha) \, , \tag{3.12}$$

and

$$\frac{\partial W^e}{\partial \boldsymbol{C}^e} = \frac{1}{2}\left(\frac{\mu'}{2}(\tilde{I}_1 - 3)J^e + f'J^e - \mu\frac{\tilde{I}_1}{3}\right)(\boldsymbol{C}^{e^{-1}}) + \frac{1}{2}\mu J^{e^{-2/3}}\boldsymbol{I}\,, \tag{3.13}$$

where

$$\mu(J^e) = \begin{cases} a_0 + a_1 J^e + a_2 J^{e^2}, & J^e \geq J_c^p, \\ b_1 \exp(b_2(J^e - 1)) + b_3, & \text{otherwise}, \end{cases}, \tag{3.14}$$

and

$$f(J^e) = \begin{cases} \dfrac{c}{2}(J^e - 1)^2, & J^p \geq J_c^p, \\ \dfrac{d_1}{2}(J^e - 1)^2 + \dfrac{d_2}{4}(J^e - 1)^4, & \text{otherwise}\,, \end{cases} \tag{3.15}$$

are the pressure dependent shear modulus and bulk modulus. We remark that we have used α for both the time index and for a material parameter but the difference may be deduced by the context. The parameters are derived from MD data and are given in Tables 3.1 and 3.2.

Table 3.1: Pressure Dependent Shear Modulus Parameters

a_0	a_1	a_2	b_1	b_2	b_3
347.15 GPa	-745.82 GPa	426.46 GPa	0.20773 GPa	-19.498	34.6439 GPa

Table 3.2: Volumetric Elastic Energy Dependence

c	d_1	d_2
-33.75 GPa	-25.167 GPa	-1879.69 GPa

Consolidation curve

The consolidation curve $p_c(J^p)$ is given as a power-law relation of the form

$$Jp_c = p_0 + \frac{A}{\alpha}(1 - J^{p^{-\alpha}})\,. \tag{3.16}$$

In addition, the tensile failure stress p_t specifies the maximum tensile pressure at which the glass sample is stable, thereby providing a lower bound on the initial consolidation pressure. These constants are tabulated in Table 3.3.

Table 3.3: Hardening parameters

A	α	p_0	p_t
-8.48613 GPa	9.2689	3.02934 GPa	−8.5 GPa

the symmetric div-quasiconvex limit surface

We now identify the critical state line. The tensile regime of the critical-state line is well-represented by a linear relation (capped vertically at $p = p_t$), the compressive regime of the critical-state line is in turn well-presented by a power law, and these are interpolated by a rank-2 connection which ensures the corresponding limit surface is symmetric div-quasiconvex [78]

$$q = \begin{cases} \frac{p_1 - p}{p_1 - p_t}\, q_t, & p \le p_1 \\ \left(s + \frac{3}{4}(p - r)^2\right)^{1/2} & p_1 \le p \le p_2 \\ B p^{\beta} & p_2 \le p\ . \end{cases} \tag{3.17}$$

The corresponding values of the constants are tabulated in Tables 3.4 and 3.5.

Table 3.4: Critical state line constants

p_1	q_t	p_t	B	β
12.337 GPa	7.402 GPa	−8.5 GPa	1.168 $\sqrt{\text{GPa}}$	0.5

Table 3.5: Critical state line constants specific to rank two connection

p_1	p_2	r	s
4.141 GPa	6.084 GPa	5.176 GPa	7.674 GPa^2

elastic region and explicit form of the dissipation function

The dissipation potential $\psi^*(\dot{\boldsymbol{F}}^p)$ is related to the dissipation potential per unit deformed volume $\tilde{\psi}^*(\boldsymbol{d}^p)$ by

$$\psi^*(\dot{\boldsymbol{F}}^p) = J\tilde{\psi}^*(\boldsymbol{F}^e \dot{\boldsymbol{F}}^p \boldsymbol{F}^{p^{-1}} \boldsymbol{F}^{e^{-1}})\ . \tag{3.18}$$

To obtain the dissipation potential per unit deformed volume, we consider the elastic region

$$K = \{\boldsymbol{y} \in \mathbb{R}^{3\times3}_{\text{sym}} | \left(\frac{2p_y + p_c - p_t}{p_c - p_t}\right)^2 + \left(\frac{q}{q_c}\right)^2 = 1; p_y = -\frac{\text{tr}(\boldsymbol{y})}{3}; q = \sqrt{\frac{3}{2}\text{dev}\boldsymbol{y} \cdot \text{dev}\boldsymbol{y}}\} \,. \tag{3.19}$$

The corresponding dissipation function follows from convex duality as

$$\tilde{\psi}^*(\boldsymbol{d}^p) = \sup_{\boldsymbol{y}\in K} \boldsymbol{y} \cdot \boldsymbol{d}^p \,. \tag{3.20}$$

Thus,

$$\boldsymbol{d}^p \in \partial I_K(y) \,, \tag{3.21}$$

where I_K is the indicator function for the set K and ∂ denotes the subdifferential of convex analysis [73]. If the boundary of K is smooth, then $\partial I_K(\boldsymbol{y})$ is the normal to the set K. Let

$$f = \alpha^2\big(\frac{2p_y + p_c - p_t}{2}\big)^2 + q^2 - q_c^2 \,, \tag{3.22}$$

where $\alpha = \dfrac{2q_c}{p_c - p_t}$. A normalized vector normal to the level sets of this function is given as

$$\boldsymbol{M} = \frac{\boldsymbol{\nabla}_{\boldsymbol{y}} f}{|\boldsymbol{\nabla}_{\boldsymbol{y}} f|} \,. \tag{3.23}$$

Computing this directly, we have

$$\boldsymbol{\nabla}_{\boldsymbol{y}} f = \frac{1}{3}\alpha^2(2p_y + p_c - p_t I + 3\text{dev}\boldsymbol{y} \,, \tag{3.24}$$

and

$$|\boldsymbol{\nabla}_{\boldsymbol{y}} f|^2 = \frac{1}{3}\alpha^4(2p_y + p_c - p_t)^2 + 6q^2 \,. \tag{3.25}$$

We may obtain a useful identity as follows:

$$\text{tr}(\boldsymbol{M}) = \frac{\alpha^2(2p_y + p_c - p_t)}{|\boldsymbol{\nabla}_{\boldsymbol{y}} f|} \,, \tag{3.26}$$

and

$$\text{dev}\boldsymbol{M} = 3\text{dev}\boldsymbol{y}\frac{1}{|\boldsymbol{\nabla}_{\boldsymbol{y}} f|} \,, \tag{3.27}$$

from which we realize

$$\frac{\text{tr}(\boldsymbol{M})^2}{3} + \text{dev}\boldsymbol{M} \cdot \text{dev}\boldsymbol{M} = 1. \tag{3.28}$$

The plastic symmetric spatial velocity gradient admits the following decomposition

$$\boldsymbol{d}^p = \dot{\epsilon}^p \boldsymbol{M} \,,$$

for some $\dot{\epsilon}^p \in \mathbb{R}$. From equation (3.20), we arrive at an explicit form for the dissipation function

$$\begin{aligned}
\tilde{\psi}^*(\boldsymbol{d}^p) &= \dot{\epsilon}^p \boldsymbol{y} \cdot \frac{\boldsymbol{\nabla}_{\boldsymbol{y}} f}{|\boldsymbol{\nabla}_{\boldsymbol{y}} f|} \\
&= \dot{\epsilon}^p \left(\frac{1}{2} \operatorname{tr}(\boldsymbol{M}) \big(\frac{|\boldsymbol{\nabla}_{\boldsymbol{y}} f|}{\alpha^2} \operatorname{tr}(\boldsymbol{M}) - p_c + p_t \big) + \frac{1}{3} |\boldsymbol{\nabla}_{\boldsymbol{y}} f| \operatorname{dev} \boldsymbol{M} \cdot \operatorname{dev} \boldsymbol{M} \right) \\
&= \dot{\epsilon}^p \left(\frac{1}{2} \operatorname{tr}(\boldsymbol{M}) \big(\frac{|\boldsymbol{\nabla}_{\boldsymbol{y}} f|}{\alpha^2} \operatorname{tr}(\boldsymbol{M}) - p_c + p_t \big) + \frac{1}{3} |\boldsymbol{\nabla}_{\boldsymbol{y}} f| (1 - \frac{\operatorname{tr}(\boldsymbol{M})^2}{3}) \right) \\
&= \frac{1}{2} \operatorname{tr}(\boldsymbol{d}^p) \left(\frac{\bar{\eta}}{\alpha^2} \operatorname{tr}(\boldsymbol{d}^p) - p_c + p_t \right) + \frac{1}{3} \bar{\eta} \operatorname{dev} \boldsymbol{d}^p \cdot \operatorname{dev} \boldsymbol{d}^p \,,
\end{aligned} \tag{3.29}$$

where

$$|\boldsymbol{\nabla}_{\boldsymbol{y}} f|^2 = \frac{q_c^2}{\big(\frac{1}{4\alpha^2} \operatorname{tr}(\boldsymbol{M})^2 + \frac{1}{6} (1 - \frac{\operatorname{tr}(\boldsymbol{M})^2}{3}) \big)}$$

follows from equations (3.22), (3.26), and (3.27) and we have defined for simplicity

$$\bar{\eta}^2 := \frac{q_c^2}{\big(\frac{1}{4\alpha^2} \operatorname{tr}(\boldsymbol{d}^p)^2 + \frac{1}{6} (\operatorname{dev} \boldsymbol{d}^p \cdot \operatorname{dev} \boldsymbol{d}^p) \big)} \,.$$

This explicit form enables the direct calculation of gradients of the dissipation function which is useful for efficiently solving equation (3.6). The calculation of these derivatives are easy but are slightly cumbersome and thus are relegated to the Appendix.

eigenfracture

To capture fracture processes in the glass, we assume a (fracture) dissipation potential of the form

$$\psi^*(C) = G_c |C| \,, \tag{3.30}$$

where G_c is an energy release rate and $|C|$ is the area of the crack set. The direct numerical simulation of such functionals is numerically cumbersome so we utilize the variational methodology of eigenfracture — which can be shown to converge to (3.30)— due to [66, 82] as modeled by material point failure. In particular, as shown

in [43], the energy release rate due to material point erosion may be estimated to first order as

$$G \approx \frac{h^2}{K_\epsilon} \int_{K_\epsilon} W^e dx \,, \tag{3.31}$$

where h defines an estimate of the material point spacing, K_ϵ is given by an ϵ neighbor construction (c.f. for instance [44, 65]), and we remark that in particular only the elastic portion of the free energy contributes to the driving force. The failure criterion on a material point basis is

$$G \geq G_c \,,$$

with the additional requirement of crack opening which we enforce by only failing a material point if the Cauchy stress tensor satisfies

$$\sigma \succ 0 \,,$$

i.e. is positive definite. We utilize the energy release rate for Silica glass of $G_c = 1$ J/m^2 = $1e^3$g/s^2 = $1e^6\mu$g/s^2 as used by Repetto et. al [70].

3.4 Model Verification

To verify that we have implemented this model correctly, we conducted several verification calculations by directly comparing with outputs from molecular dynamics calculations that were used to parameterize the model in [78]. Evidently, the model reflects the underlying molecular dynamics data quite well as seen in Figure 3.1a. The line of shear yield stress versus pressure, which in this context may be viewed as a limit surface of plasticity, coincides quite closely with the MD data.

Additionally, we compute J as a function of J^e. The model was not fit to this specific variable relationship in [78] so it provides a good test of the model's behavior. In figure 3.1b, we plot both the calculation for the model as well as the MD data. The agreement is reasonably good. The constitutive law captures the phase transition (the jump) due to the elastic moduli. However, during loading, it transitions slightly later than in the MD calculations as evidenced by the initial J curve which curves out beyond the data.

(a)

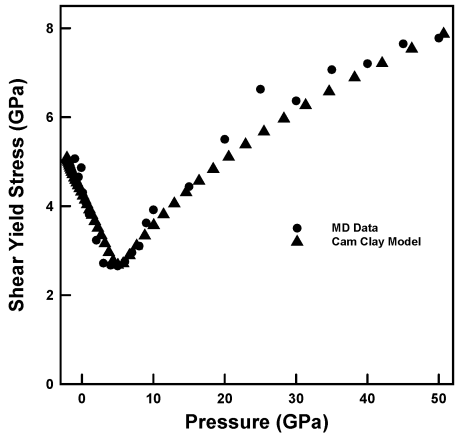

(b)

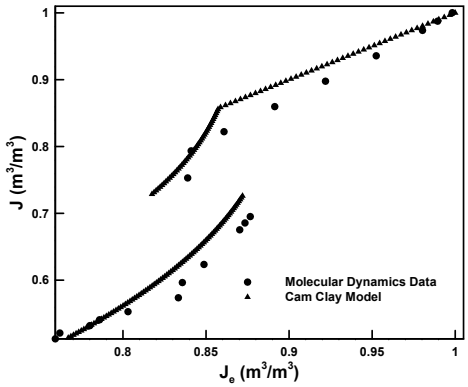

Figure 3.1: (A) The implementation of the silica glass Cam Clay model represents the MD data well. (B) We plot J versus J_e for the constitutive law and the MD data. This particular data relationship was not used to fit the constitutive law.

3.5 Comminution of a glass rod

As an validation example for this model of Silica glass, we examine the experimental data of Brar, Bless and Rosenberg [9]. The configuration of interest is given in Table 3.6.

Table 3.6: Rod initial configuration parameters

L (mm)	D (mm)	v_0 (mm/s)
150	12.7	2.1×10^5

We discretize the domain using 975304 OTM nodes. The calculation was run in paralell on 16 processors. The measurements in Brar et al. [9] were taken about 10 μs apart and they recorded six frames. The simulation is run for 10^{-4} sec to encompass the timescale over which the experimental data was collected. We now study the impact of a glass rod, 150 mm in length with a diameter of 12.7 mm. The rod strikes a stiff wall — modeled as a step — quadratic potential with a stiffness coefficient much in excess of the moduli of glass. We reproduce here a scenario studied by Brar et. al in Figure 3.2 with an impact speed of 210 m/s. The figure consists of six high speed pictures taken 10 microseconds apart of a glass rod impacting a wall. These track the speed of propagation of the failure wave which is defined by the location ahead of the which the material is non-fractured and behind which the material is totally shattered. We have reproduced a simulation

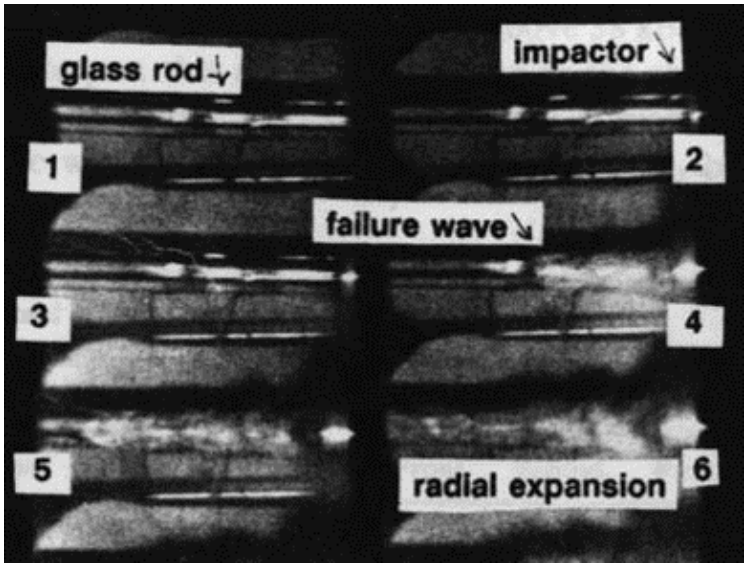

Figure 3.2: Pictures of experimental failure wave propagation study due to Brar, Bless, and Rosenberg in 1991 at 210 m/s at 10 μs intervals.

of this scenario to assess the efficacy of our model. We visualize the rod failing shortly after impact (~30 microseconds) in Figure 3.3 using blue spheres to picture the failed sections and red to picture the non-failed section. In particular, we find that the general behaviors are remarkably consistent with experiment and moreover, specific quantitative targets such as failure wave propagation velocity are matched quite closely – obtaining $V_{\text{experimental}}$ = 4.5 mm/μs and $V_{\text{simulation}}$ = 4.7 mm/μs. Similarly, we repeat the calculation for the case of Impact speed, v = 336 m/s. Again, we obtain excellent agreement of $V_{\text{experimental}}$ = 5.2 mm/μs and $V_{\text{simulation}}$ = 5.4 mm/μs. The computational velocity speeds are slightly higher than the

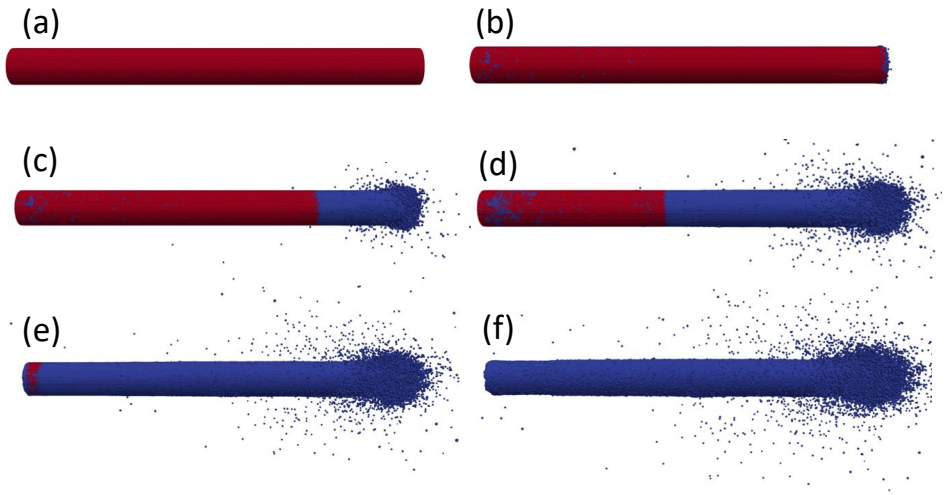

Figure 3.3: Time snapshots of impact of glass rod at 210 m/s(a) t = 0 μs and (b) t = 10 μs; (c)t = 20 μs (d)t = 30 μs (e) t = 40 μs (f) t = 50 μs.

experimentally measured speeds reported however it is unknown at the present if this is a systematic error or otherwise.

Table 3.7: Failure wave velocity comparison to experiment

Impact Speed	Failure wave speed computational	Failure wave speed experimental
125 m/s	2.6 mm/μs	2.3 mm/μs
210 m/s	4.7 mm/μs	4.5 mm/μs
336 m/s	5.4 mm/μs	5.2 mm/μs

In figures 3.5 and 3.6, we visualize the pressure and Mises stress respectively for the case of v = 336 m/s (The results are quite similar in the case of 210 m/s). The failed section of the rod is portrayed in gray with direct representation of the OTM particles as points. Maximum pressure and Mises stress are given in dark blue. We note that in particular, the maximal values (in dark blue) of pressure and mises stress indicate that yield is taking place in the dark blue regions. We remark that a lower stress region in light blue propagates ahead of the dark blue.

This aligns with the notion of elastic precursor and plastic follower [49] observed in the theories of one dimensional elastic-plastic waves. However, the 3D nature of this calculation is particularly important in the sense that the interaction of the elasticity, plasticity, and fracture which produces the radial expansion characteristic

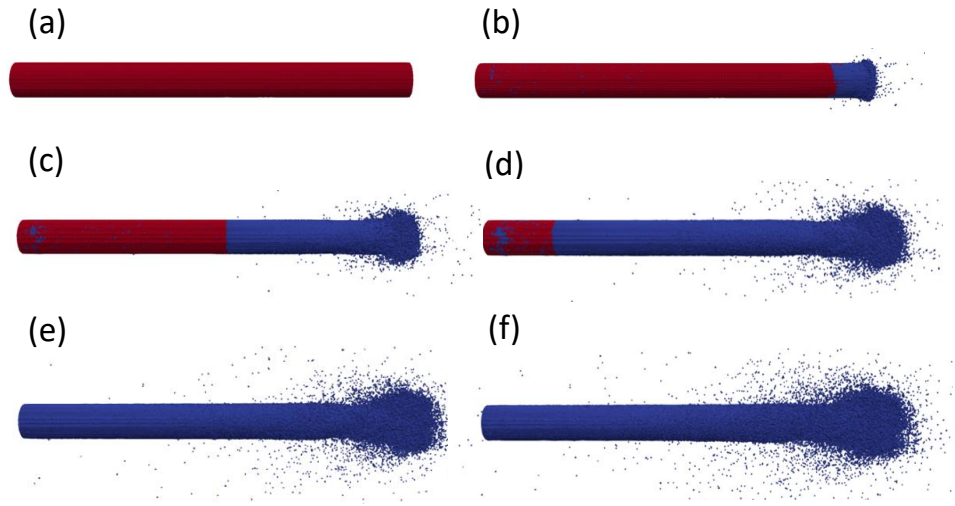

Figure 3.4: Time snapshots of impact of glass rod at 336 m/s(a) t = 0 μs and (b) t = 10 μs; (c)t = 20 μs (d)t = 30 μs (e) t = 40 μs (f) t = 50 μs.

of experimentally observed failure waves. Indeed, the plasticity law is intrinsically 3D due to its incorporation of volumetric plasticity.

In figure 3.7, we visualize the transverse (to the axis of the rod) velocity distributions versus location along the axis of the rod at several different times. In particular, we see that as the plastic wave passes through the material and the glass begins to fragment, much of the material has a large transverse velocity, strongly characterizing the notion of *radial expansion* following failure wave. A large portion of the material has a velocity of between 10^3 and 10^5 mm/s with a certain smaller fraction of the material being ejected at rates similar to the impact speed to the rod in the 10^5 to greater than 10^6 mm/s range.

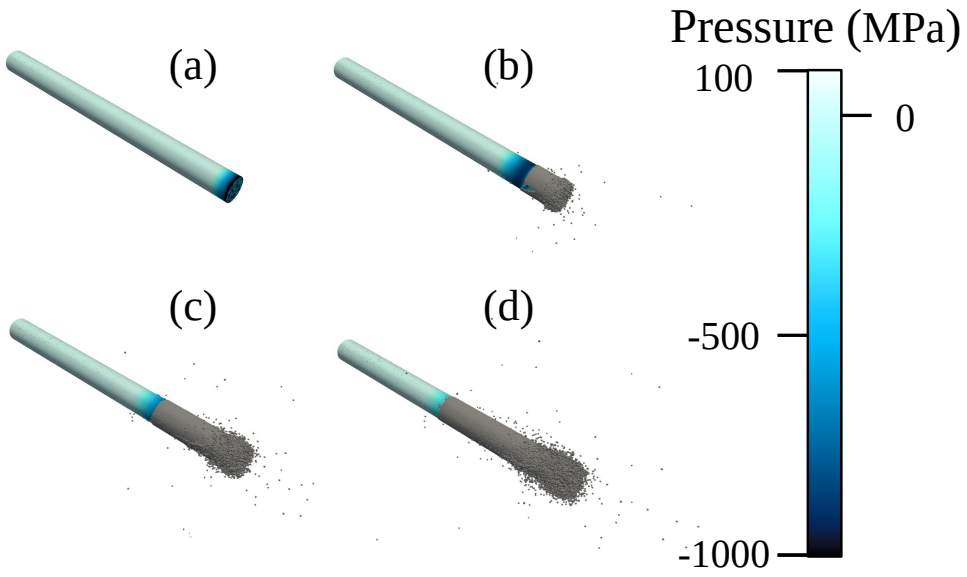

Figure 3.5: Time snapshots of the pressure contours in glass rods for impact speed of 336 m/s(a) t = 5 μs and (b) t = 10 μs; (c)t = 15 μs (d)t = 20 μs.

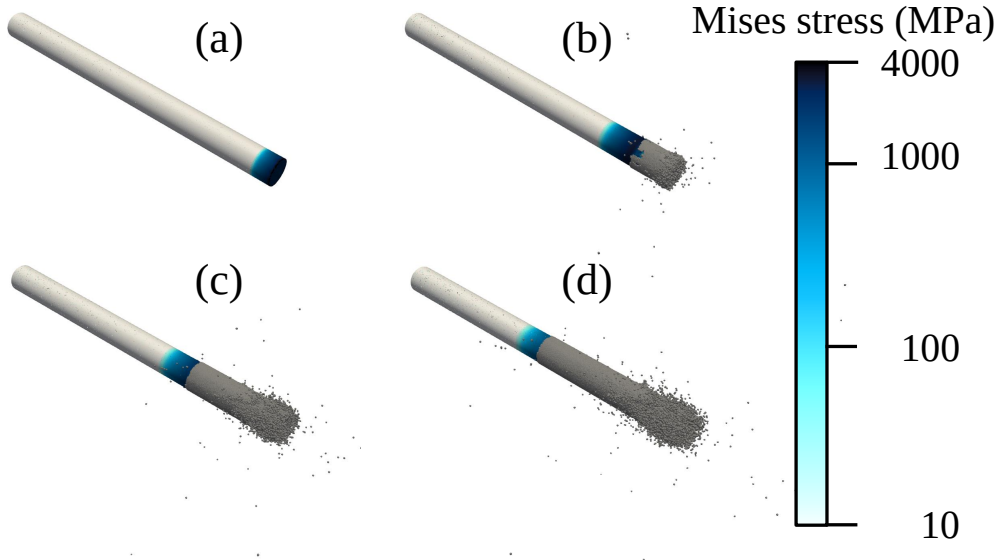

Figure 3.6: Time snapshots of the Mises stress contours in glass rods for impact speed of 336 m/s(a) t = 5 μs and (b) t = 10 μs; (c)t = 15 μs (d)t = 20 μs.

(a)

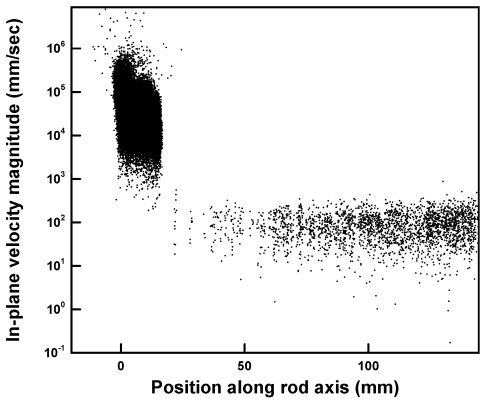

(b)

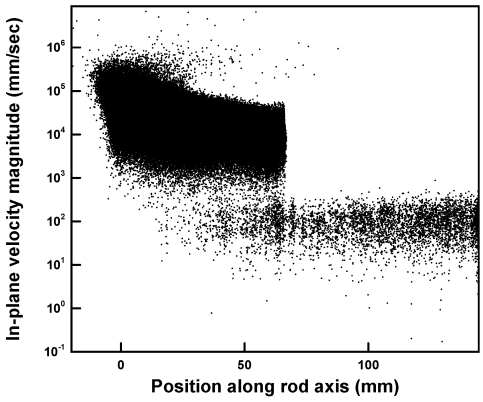

(c)

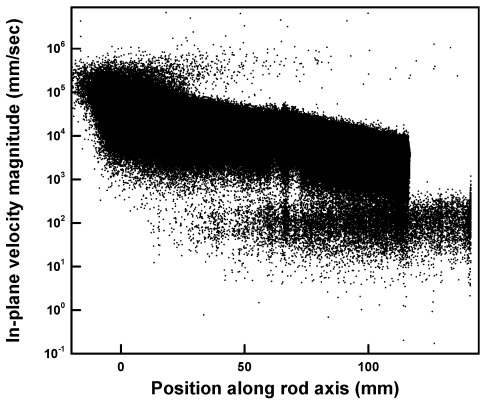

Figure 3.7: Time snapshots of transverse velocity per OTM particle by the location along the direction of impact. In particular, this is for the impacting rod traveling at 336 m/s(a) t = 10 μs and (b) t = 20 μs; (c)t = 30 μs.

3.6 Summary and concluding remarks

We have performed the first detailed continuum calculation of a previously proposed model for Silica glass using the *optimal transport meshfree* method. The model performs well with fidelity to existing MD data. Second, the model strongly characterizes *failure waves* in glass bars as compared to experiments by Brar and coworkers with no fitting to these results the elastic or plastic parameters which were all previously derived from MD data. In particular, the simulation of glass rods reproduces accurate failure wave speeds as well as dramatic radial expansion emblematic of this distinctive physical process. In addition, these calculations constitute, to our knowledge, the first usage of a plasticity law explicitly constructed to preserve *symmetric div-quasiconvexity*. Open remaining questions meriting further investigation involve a) additional detailed calculations involving plasticity limit surfaces that are explicitly symmetric div-quasiconvex in both static and dynamics settings, and b) the nature of the plasticity law (including the nature of the yield surface) at difference temperatures and strain rates which may admit localized plastic deformation such as shear bands. These questions are under active investigation by the authors.

Acknowledgements

We gratefully acknowledge support from the US Office of Naval Research through grant N000141512453. This work was supported by a NASA Space Technology Research Fellowship.

Chapter 4

TEMPERATURE AND RATE

Research presented in this chapter has been adapted from [80].

4.1 Introduction

Silica glass is one of the most commonly used glassy materials in engineering and its material properties have been a long-standing topic of investigation. However, it exhibits several anomalous behaviors (see [78] and references therein) under extreme pressure. Specifically, silica exhibits both non-monotonic dependence on pressure of the elastic moduli [35] as well as a significant decrease in strength in certain regimes as it is compressed to denser structures with higher coordination [57]. In [78], the anomalous yield behavior was given the interpretation of a *non-convex limit domain* in the sense of limit analysis of classical critical state plasticity theory [49]. See also [79].

Various experimental studies of failure waves in silica and soda-lime glass through angled flyer plate impact experiments support this viewpoint [1, 12, 84, 90]. However, these studies also include instances where the experimental conditions — such as temperature and strain rate — are quantitatively different from those computed in [78]. Additionally, it appears that under various conditions the inelastic mechanical response of glass may be dramatically different and may involve microstructured deformation such as shear banding and localization [54]. Though small relative to the macro-scale, these deformations are *large* relative to any atomistic calculations. It is well known, (c.f. for instance [20] for an introduction) that the determination of shear localization is highly dependent on temperature and strain rate.

In this study, we implement a multiscale modeling program that succeeds in extending and calibrating a Cam-Clay model of plasticity [78] for fused silica glass to account for the thermal and rate dependence of the media directly from data mined at the atomistic level using both molecular dynamics and max-ent atomistics. This model has been formulated with the intended application of ballistic and hypervelocity impact. The effect of rate and temperature are of high importance under such conditions which, for example, include space applications such as as micrometeoroid impact. See also the applications suggested by [6].

We find that silica glass exhibits anomalous yield behavior in the sense that the dependence of the shear yield strength on the pressure is non-monotonic. This essentially implies that the limit domain — in the sense of critical state theory — is non-convex. We find following [77] that the appropriate condition describing the yield behavior in this context is symmetric div-quasiconvexity which characterizes the material stability against the formation of micromechanical residual stresses. Silica glass is the first example (to our knowledge) of a non-convex elastic domain derived from micromechanics. We endeavor to determine to what extent this anomalous yield behavior exhibits either qualitative or quantitative dependence on both strain rate and temperature. We find that the process of constructing the critical state line is quantitatively dependent on temperature and rate. Nonetheless the construction holds for all regimes of temperature and rate probed in this study. Thus, the relaxation of the non-convex limit domain and the corresponding rigorous connection between microstructural patterning and the non-convexity of the limit domain is extremely robust with respect to varied conditions.

The paper is organized as follows. In section 4.2, we perform extensive molecular dynamics and maximum entropy atomistics calculations to produce a large quantity of data describing the inelastic deformation of silica under a wider range of temperature, pressure, and rate conditions. In section 4.3, we formulate and calibrate a Cam-Clay plasticity model to the data and show that the model captures the MD data well. In section 4.4, we explore the relationship between the anomalous critical state line, the stability (or lack thereof) of silica glass against micro-mechanical residual stresses, and the atomistic origins of the anomalous yield.

4.2 Supporting Molecular Dynamic Calculations

In this section, we generate data describing silica glass using molecular dynamics simulations. Specifically, we establish the relationship between pressure, compression, the shear stress shear strain relationship, and the sensitivity of the shear behavior to the rate of loading.

Temperature

We first study the effect of temperature on densification and shear behavior of silica glass. We construct several 1500 atom sample systems of silica by a melt-quench procedure beginning from a β-crystobolite (a detailed accounting of the preparation of the configurations is given in [78]). We utilize a Nosé-Hoover (NPT) barostat to control the pressure and temperature. All the results in this section are obtained by

averaging over the various initial conditions.

In Fig. 4.1, we display pressure versus consolidation for a large range of temperatures from $300K$ up to $1900K$. Independent of temperature, the material exhibits extensive consolidation as evidenced by the unloading curves and a distinctive increase in slope during loading. We extract the elastic portion of the response in Fig. 4.2 by examining the unloading curves, determining the elastic Jacobian by $J^e = J/J^p$, and by assuming that the plastic Jacobian remains constant during unloading.

The elastic response softens as the temperature increases. In particular, to attain the same pressure, the volume must be elastically compressed by a substantially larger degree. Interestingly, there is some scatter in the elastic unloading data. We interpret this as noise due to the variability of deformation accommodating microstructure for the purposes of modeling. However, it is imaginable that more sophisticated modeling, perhaps in combination with data science, could extract additional useful information from the data.

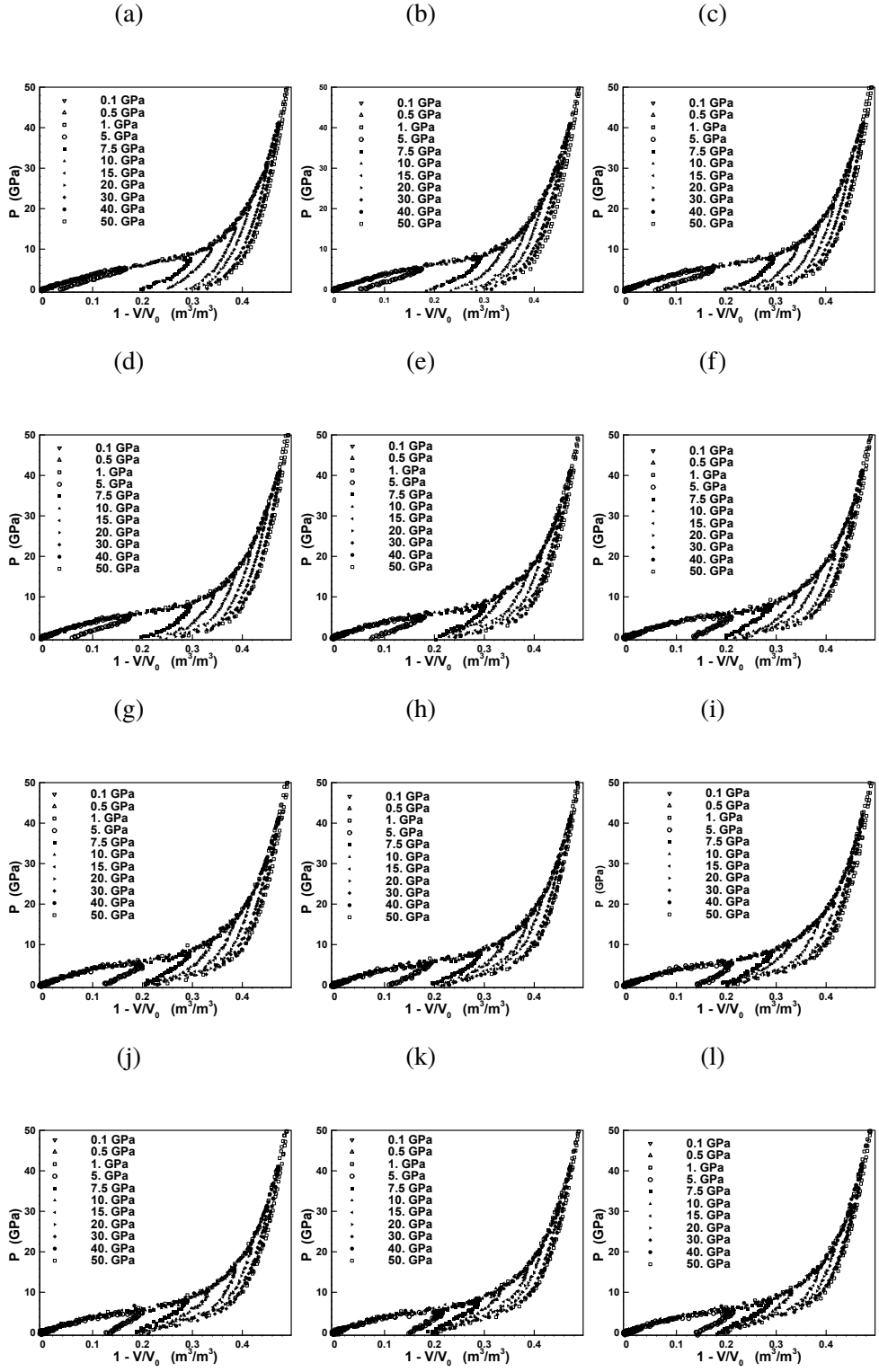

Figure 4.1: The isothermal pressure-compression relationship at temperatures T = (a) 400 (b) 600; (c) 800 (d) 1000 (e) 1200 (f) 1300 (g)1400 (h) 1500 (i) 1600 (j) 1700(k) 1800 (l) 1900 K.

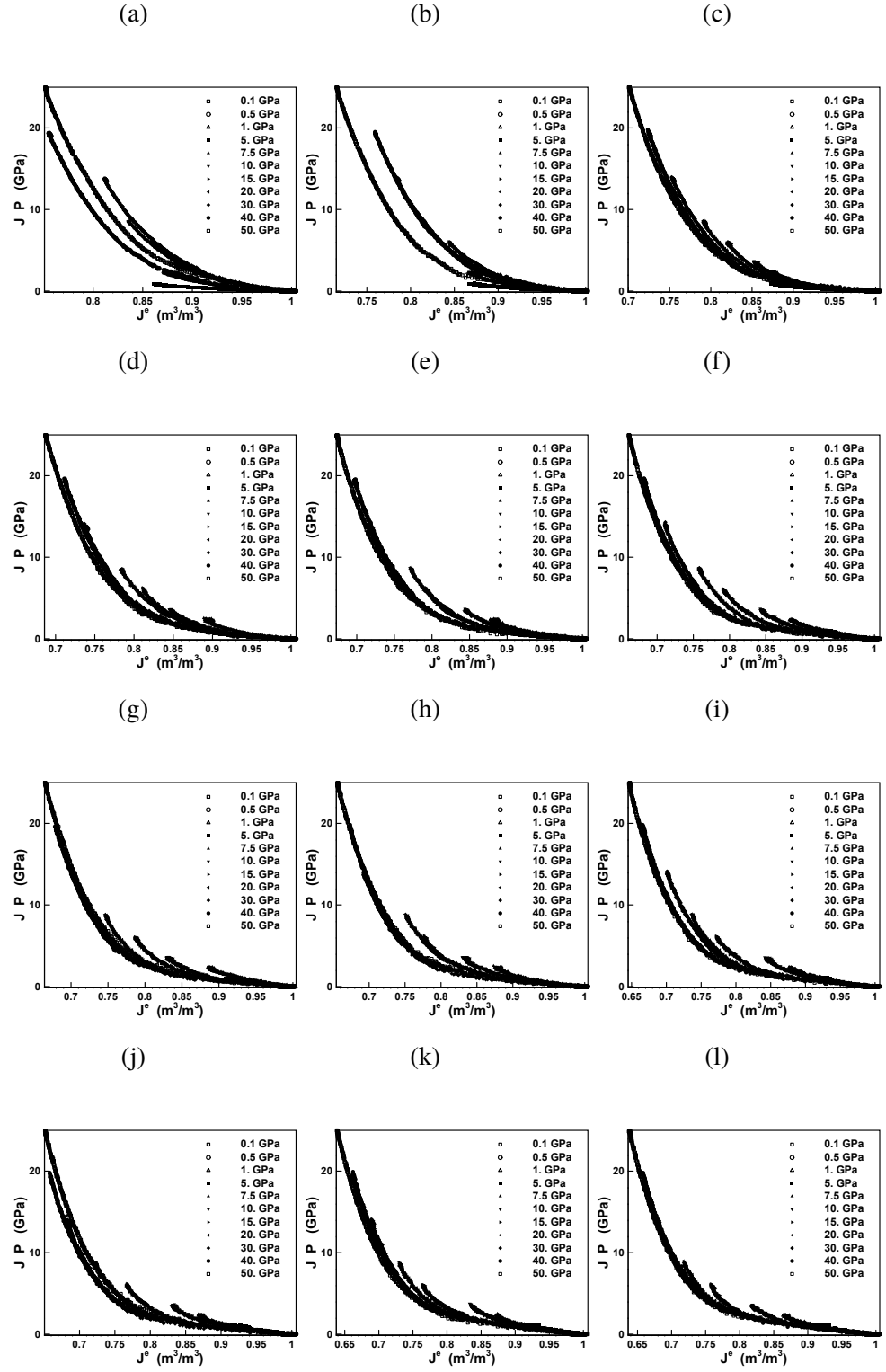

Figure 4.2: The isothermal (Kirchoff) pressure versus elastic Jacobian relationship at temperatures T = (a) 400 (b) 600; (c) 800 (d) 1000 (e) 1200 (f) 1300 (g)1400 (h) 1500 (i) 1600 (j) 1700(k) 1800 (l) 1900 K.

In Fig. 4.3, we plot the permanent volumetric deformation. Specifically, for each temperature we take the maximum pressure from each of the curves in Fig. 4.1 and the final plastic deformation as data points. All curves display a distinctive consolidation regime with small slope followed by a near asymptote at some value of J^p. At high temperatures, the consolidation asymptotes at $J^p \approx 0.82$ whereas at low temperatures the consolidation asymptotes at $J^p \approx 0.68$. We may gain insight from the molecular dynamics calculations in this regime.

The low density phase of silica (which is 4 fold coordinated) has a volume which is nearly independent of temperature. The equilibrium volume of the high density phase of silica (which is 6 fold coordinated) has substantial dependence on temperature. An alternative hypothesis is that the tradeoff between 6-fold and 5 fold coordinated symmetry in the high density phase of silica becomes reversible at high temperature due to thermal activation thereby resulting in decrease of permanent consolidation. Interestingly there is a inflection point in the behavior of the densification at $J^p = 0.82$ where the densification trend reverses. For permanent consolidation $J^p \geq 0.82$, lower temperatures actually exhibit *less* densification whereas higher temperatures exhibit more. Thus, we observe that increasing temperatures result in more immediate deformation and yet the permanent deformation arrests earlier. We now examine the effect of joint volumetric and shear deformation. In Fig. 4.4, we display shear stress versus shear strain for several temperatures. The behavior is qualitatively consistent across a wide range of temperatures exhibiting an elastic region and plastic region.

In each case, for a given shear strain, the shear stress first decreases with increasing pressure and then increases. Furthermore, as the temperature increases, the stress decreases. We compute the yield stress by taking an average over the plateau characterizing the plastic region. We plot the yield stress as a function of pressure for various temperatures in Fig. 4.5. The anomalous yield behavior — that the yield stress is a minimum at about 5 GPa — is evident and persists independent of temperature.

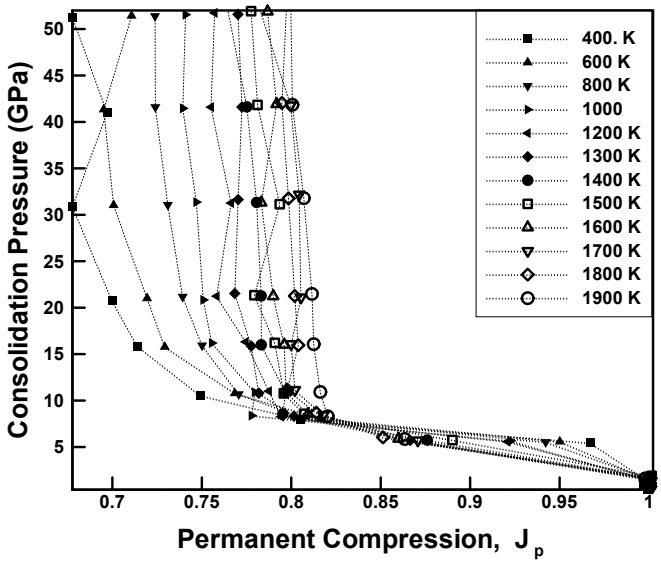

Figure 4.3: The consolidation pressure is plotted versus the plastic Jacobian for several temperatures.

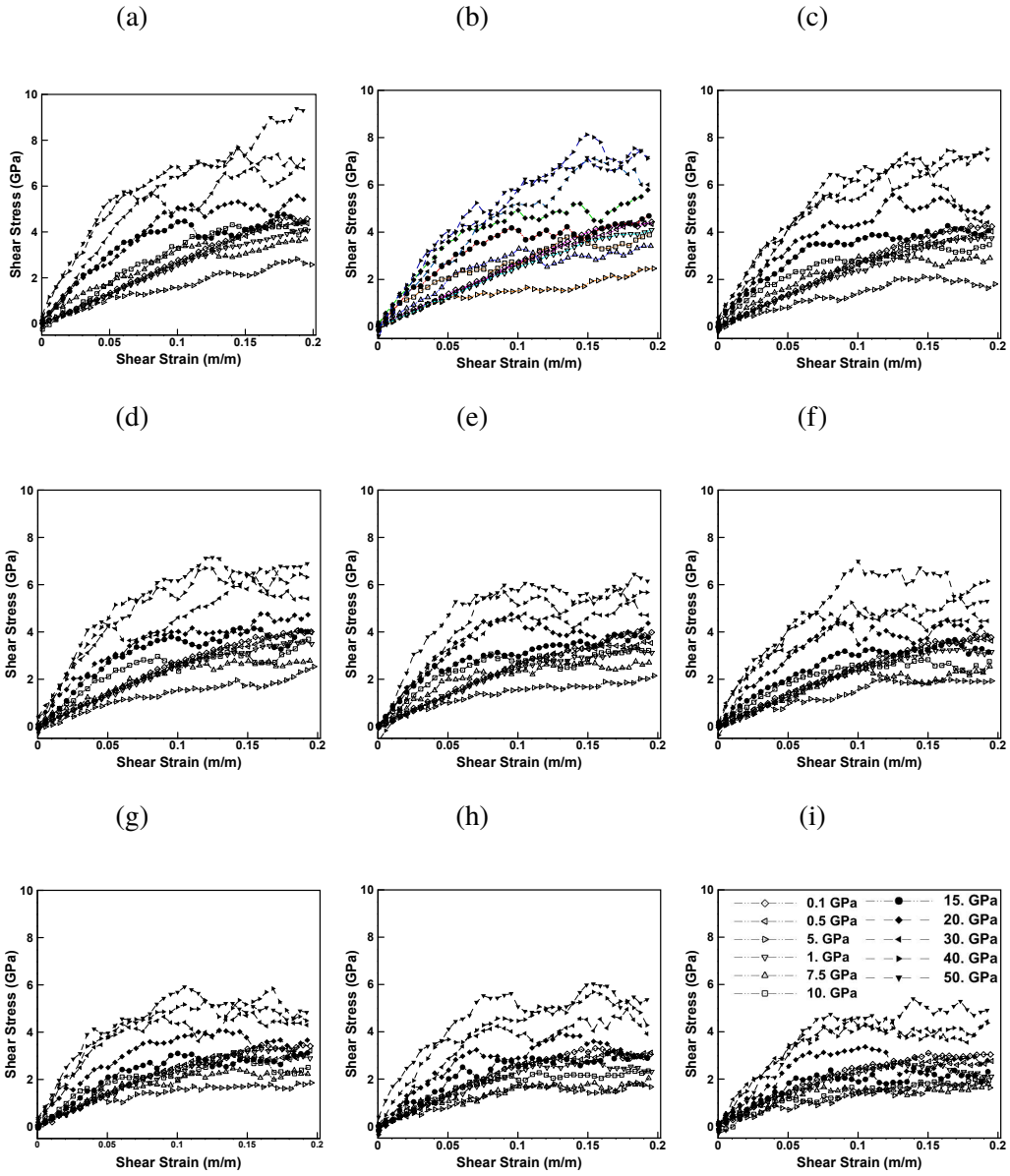

Figure 4.4: The shear stress shear strain relationship at temperatures T = (a) 400 (b) 500; (c) 700 (d) 900 (e) 1100 (f) 1300 (g)1500 (h) 1700 (i) 1900. The legend included in (i) applies to all the figures.

(a)

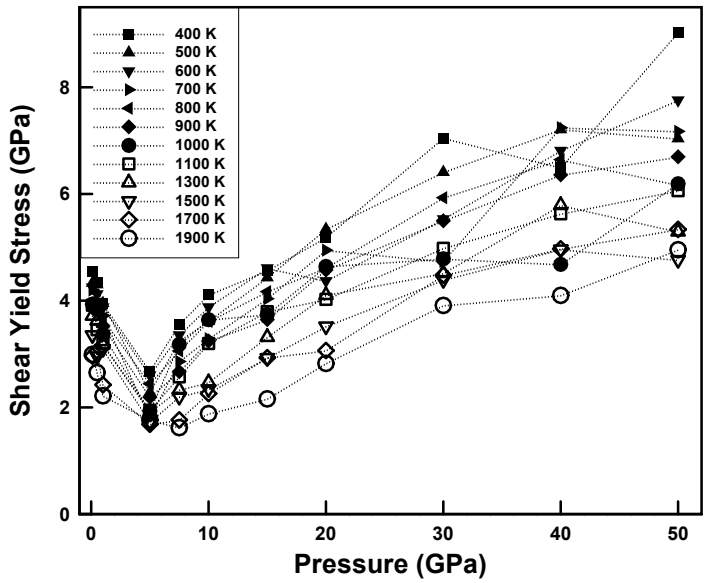

(b)

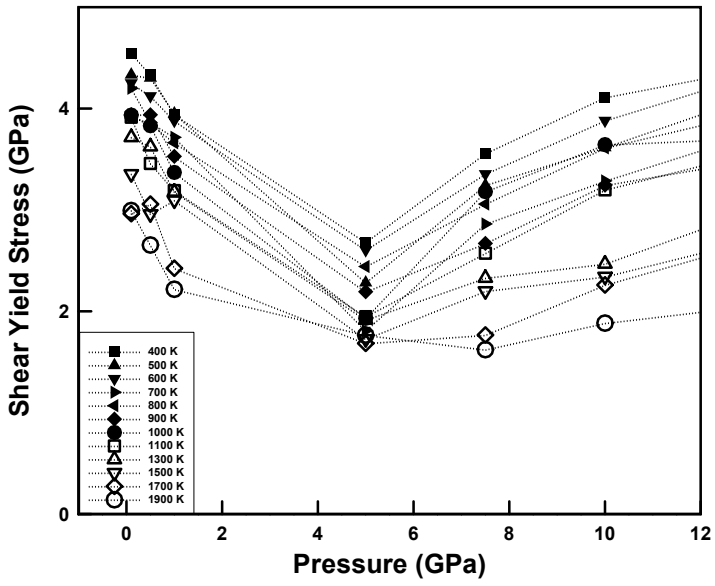

Figure 4.5: (A) Shear yield stress are plotted versus pressure for several of temperatures. (B) A zoomed view of the anomalous yield region.

Rate of deformation

We consider the effect of rate on silica glass utilizing a combination of molecular dynamics and maximum entropy atomistics.

Max-ent atomistics

For completeness, we include a brief summary of the theory of max-ent atomistics. More detail may be found in [4, 36, 55, 100] and references therein. Consider a system of N identical particles described by position, $\boldsymbol{q} = \{q_1, q_2..., q_N\} \in \mathbb{R}^{3N}$ and momentum $\boldsymbol{p} = \{p_1, p_2..., p_N\} \in \mathbb{R}^{3N}$. The phase average of a state variable function $A : \mathbb{R}^{6N} \to \mathbb{R}$ is defined to be

$$\langle A \rangle = \frac{1}{\hbar^{3N}} \int_{\mathbb{R}^{3N} \times \mathbb{R}^{3N}} A(\boldsymbol{q}, \boldsymbol{p}) \rho(\boldsymbol{q}, \boldsymbol{p}) \boldsymbol{dq dp} \,, \tag{4.1}$$

where ρ is a probability density on the phase space where $\hbar^{3N}$ provides a natural nondimensionalization. The least biased probability distribution consistent with our knowledge of the particles is the one for which the entropy is maximum

$$S[\rho] = -k_B \langle \log \rho \rangle \tag{4.2}$$

subject to the constraint of mean position, momenta, and energy for each particle: $\langle q_i \rangle = \bar{q}_i$, $\langle p_i \rangle = \bar{p}_i$ and $\langle h_i \rangle = e_i$ where h_i is a local trial Hamiltonian for each atom [31]. Enforcing the stationarity of (4.2) explicitly we find the least biased estimate of the probability density over phase space to be

$$\rho = \frac{1}{\mathcal{Z}} \exp(-\boldsymbol{\beta}^T \boldsymbol{h}) \,,$$

where we define $\beta_i = \dfrac{1}{k_b T_i}$ component wise. $\mathcal{Z}$ is a partition function defined as

$$\mathcal{Z} = \frac{1}{\hbar^{3N}} \int_{\mathbb{R}^{3N} \times \mathbb{R}^{3N}} \exp(-\boldsymbol{\beta}^T \boldsymbol{h}) \boldsymbol{dq dp} \,,$$

and k_b is Boltzmann's constant. T_i has the interpretation as a local atom-wise temperature. The mean positions may be enforced to above follow the trajectories given by the classical Hamilton's equations

$$\frac{d\bar{p}_i}{dt} = -\frac{d\bar{H}}{d\bar{q}} \,, \tag{4.3}$$

$$\frac{d\bar{q}_i}{dt} = \frac{d\bar{H}}{d\bar{p}} \,, \tag{4.4}$$

where $\bar{H} = \langle H \rangle$ or may minimize a free energy in the quasi-static limit. The previous equations may be closed with a discrete Fourier-type law to describe the manner in which heat is transfered between each of the atoms. Variational mean field theory due to Bogoliubov states that a trial Hamiltonian may be selected via the merit criterion of minimum *meanfield free energy*. We utilize a trial Hamiltonian of the form

$$H_0(q,p) = \sum_{i=1}^{N} h_i \,, \tag{4.5}$$

where

$$h_i := \frac{1}{2m_i}|p_i - \bar{p}_i|^2 + \frac{m_i\omega_i^2}{2}|q_i - \bar{q}_i|^2 \,.$$

To select ω_i, we minimize the meanfield free energy

$$\inf_{\omega \geq 0} \left(F_0 + \langle H - H_0 \rangle_0\right), \tag{4.6}$$

where

$$F_0 := -\sum_{i=1}^{N} \frac{1}{\beta_i} \log(Z_{0i}/\hbar^3) \,, \tag{4.7}$$

with $Z_{0i} = \left(\dfrac{2\pi}{\beta_i\omega_i}\right)^3$ and

$$\langle H_0 \rangle_0 = \sum_{i}^{N} \beta_i^{-1} =: \sum_{i=1}^{N} h_i \,,$$

with $\langle\rangle_0$ denoting average with respect to the trial Hamiltonian probability density. Furthermore,

$$Z_0 = \int \exp(-\alpha \cdot z - \beta \cdot \epsilon(z)) dz = \Pi_{i=1}^{N} Z_{0i}$$

is the mean field approximation to the partition function.

This is equivalent to the problem

$$\inf_{\omega \geq 0} \left(\langle V \rangle_0 - \sum_{i=1} \beta_i^{-1} \log(Z_{0i}/\hbar^3) \right), \tag{4.8}$$

or

$$\inf_{\omega \geq 0} \left(\langle V \rangle_0 + \sum_{i=1} 3h_i \log(\omega_i) \right). \tag{4.9}$$

The Euler Lagrange equations are

$$\frac{\partial \langle V \rangle_0}{\partial \omega_j} + \frac{3}{\omega_j \beta_j} = 0 \, . \tag{4.10}$$

We compute phase averages $\langle V \rangle$ via numerical quadrature (see [36]). This renders the equations of motion in a form that closely resembles those of molecular dynamics. This enables the use of standard software such as LAMMPS [68] and we have specifically utilized the implementation of MaxEntLammps due to Ponga et al.[51]. Our own contribution to this implementation was the computation of phase averages of potentials specific to silica (see [78] for the specific potential forms used in this study). We have verified the robustness of the implementation by correctly predicting thermal expansion in glass.

We remark that time dependent max-ent provided little increase in time step as compared to MD. This contrasts with some previous studies in metals and is most likely due to the 'wobbly' nature of the energy in glasses -– that is to say, the energy landscape of glassy media is highly non-convex. This energetic character is of course responsible for many of the remarkable and physically useful properties of glass. In fact, to our knowledge this is the first application of max-ent to an amorphous solid.

In figures 4.7 and 4.8, we compute several rate dependent curves using (standard) molecular dynamics (MD) and compute the rate independent limit using max-ent (MXE). The effect of temperature is taken into effect variationally with quasi-static max-ent. Evidently, the curve computed with max-ent serves as a limit of the rate dependent curves. The general trend that we observe is that the stress decreases as a function of decreasing strain rate. The rate of loading has minimal effect for low temperatures 300K. However, this decrease becomes more pronounced for both increasing temperatures and pressures.

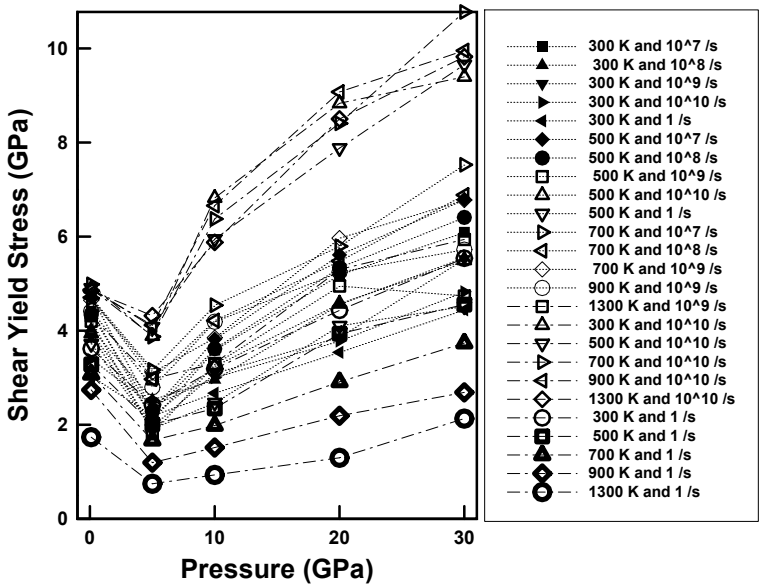

Figure 4.6: Shear yield stress are plotted versus pressure for several temperatures and strain rates.

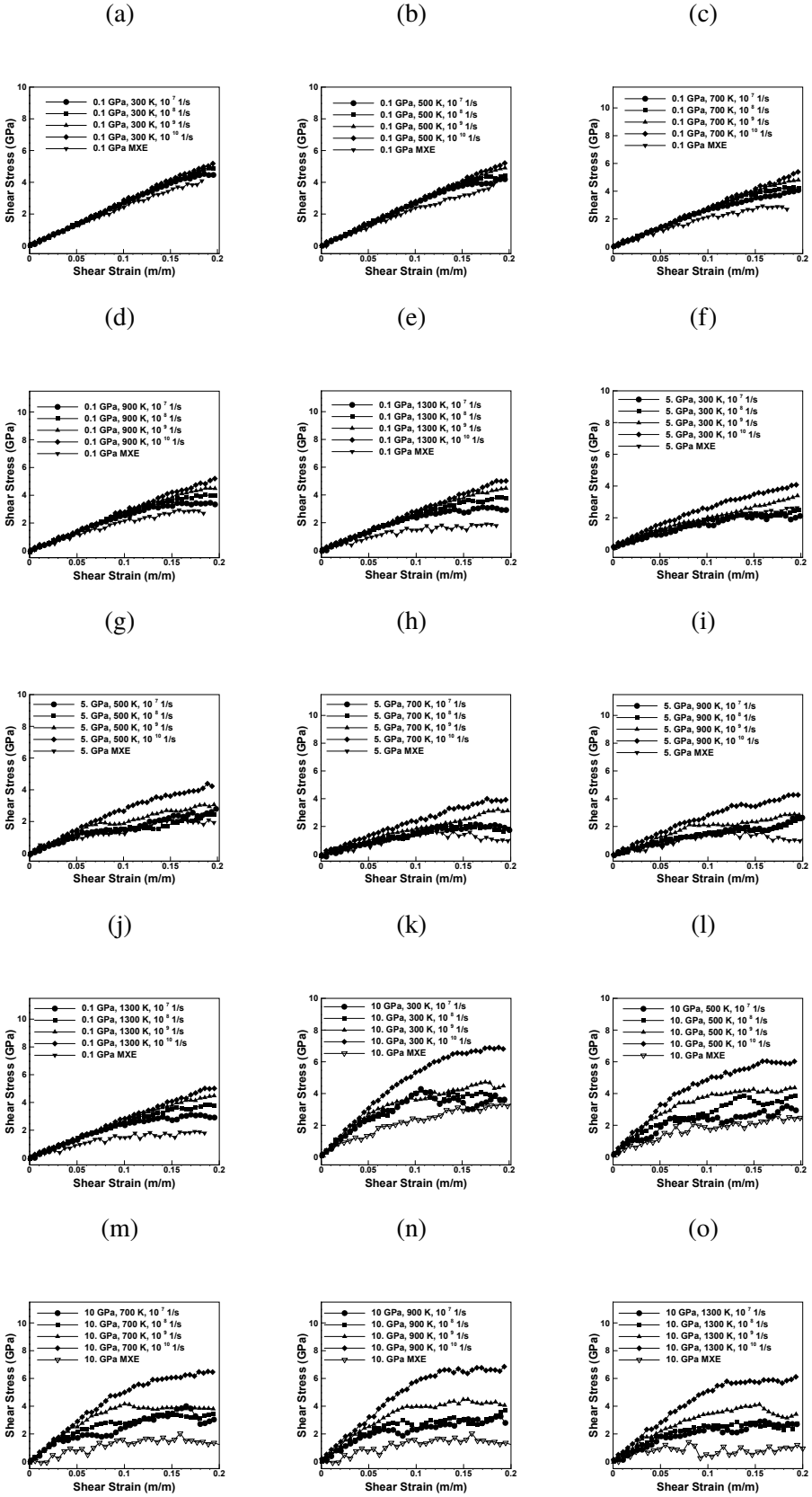

Figure 4.7: The shear strain rate behavior at various temperatures and pressures. The calculated stress strain relations are shown for pressures of $p = 0.1$, 5, and $10GPa$ for several different temperatures and strain rates.

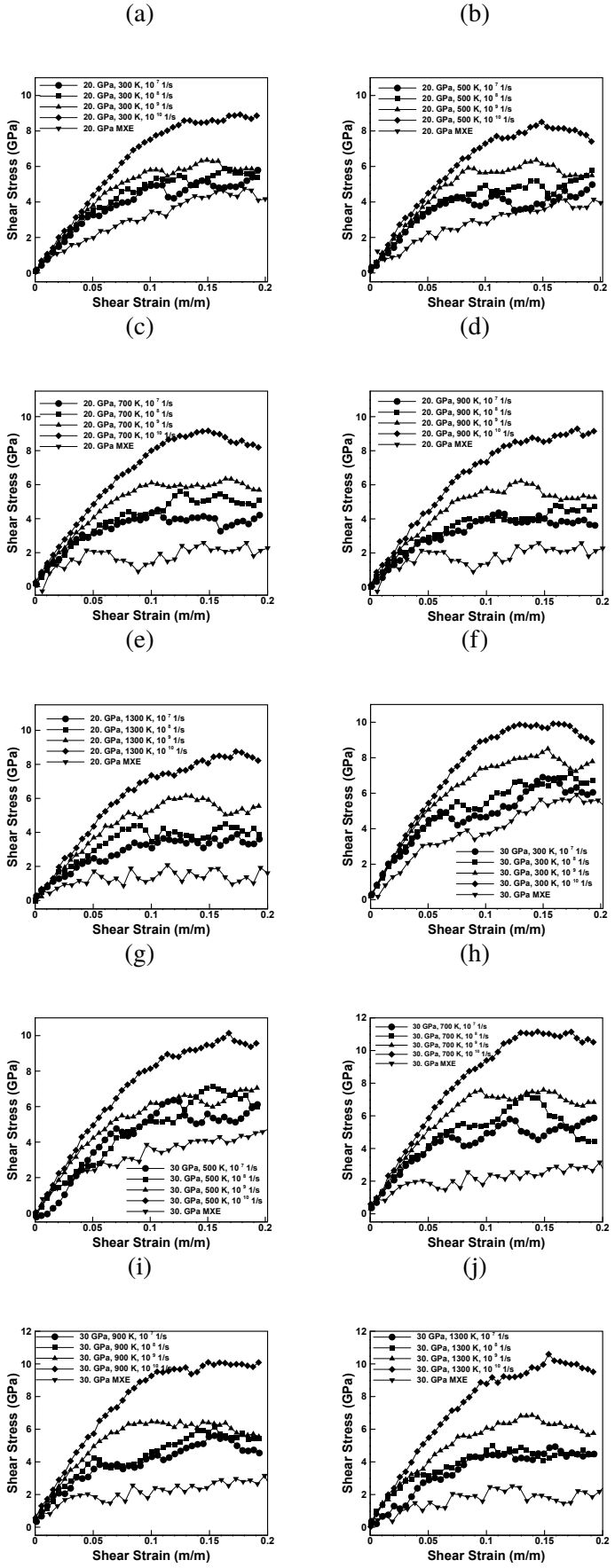

Figure 4.8: The shear behavior at various temperatures and pressures. The calculated stress strain relations are shown for pressures of p = 20, and 30 GPa for several different temperatures and strain rates.

4.3 Continuum model

Let $\Omega \subset \mathbb{R}^3$ denote the material body in the undeformed configuration. Let $\varphi : \Omega \to \mathbb{R}^3$ denote the deformation mapping and $\boldsymbol{F} = \boldsymbol{\nabla}\varphi$ denote the deformation gradient. We make the standard assumption [41] that the deformation gradient undergoes a multiplicative decomposition into an elastic part and a plastic part

$$\boldsymbol{F} = \boldsymbol{F}^e \boldsymbol{F}^p \, .$$

Furthermore, let $J = \det \boldsymbol{F}$, $J^e = \det \boldsymbol{F}^e$, and $J^p = \det \boldsymbol{F}^p$. Let $V = \dot{\varphi}(X)$ denote the material velocity. The spatial velocity gradient follows as

$$\boldsymbol{l} = \dot{\boldsymbol{F}} \boldsymbol{F}^{-1} \, ,$$

and consequently undergoes an additive decomposition

$$\boldsymbol{l} = \boldsymbol{l}^e + \boldsymbol{l}^p \, ,$$

into an elastic and plastic spatial velocity gradient where

$$\boldsymbol{l}^e = \dot{\boldsymbol{F}}^e \boldsymbol{F}^{e-1} \, ,$$

and

$$\boldsymbol{l}^p = \boldsymbol{F}^e \dot{\boldsymbol{F}}^p \boldsymbol{F}^{-1} \boldsymbol{F}^{e-1} \, .$$

We also define

$$\hat{\boldsymbol{l}}^p = \dot{\boldsymbol{F}}^p \boldsymbol{F}^{p-1} \, ,$$

which is also commonly used in the construction of plasticity laws. Interestingly, we can compute the first invariant of $\boldsymbol{l}^p$ and obtain

$$I_1(l^p_{ij}) = l^p_{ii} = F^p_{ij} \dot{F}^p_{jk} F^{p\,-1}_{kl} F^{e-1}_{li} = \dot{F}^p_{jk} F^{p\,-1}_{kj} = I_1(\hat{\boldsymbol{l}}^p) \, ,$$

as well as the second invariant

$$I_2(\boldsymbol{l}^p) = l^p_{ij} l^p_{ij} = \dot{F}^p_{km} F^{p\,-1}_{ml} \dot{F}^p_{ls} F^{p\,-1}_{sk} = I_2(\hat{\boldsymbol{l}}^p) \, .$$

Thus, if $\psi^* = \psi^*(I_1(\boldsymbol{l}^p), I_2(\boldsymbol{l}^p))$, then there is no difference between using $\boldsymbol{l}^p$ and $\hat{\boldsymbol{l}}^p$. The symmetric portion of the velocity gradient is denoted by

$$\boldsymbol{d} = \frac{1}{2}\left(\boldsymbol{l} + \boldsymbol{l}^T\right) \, .$$

If $\boldsymbol{l}^p$ is symmetric, then $\boldsymbol{d}^p = \boldsymbol{l}^p$. We use a dual kinetic law of the form $\boldsymbol{l}^p \in \partial\psi^*(\boldsymbol{y})$ and assume that $\boldsymbol{l}^p = \dot{\gamma}\boldsymbol{M}$ where $\dot{\gamma}$ is a plastic rate multiplier. $\boldsymbol{M}$ specifies the

direction of plastic flow and satisfies a normality rule. If such a normality rule is computed with respect to a set of symmetric matrices such as $\boldsymbol{y}$ then M is symmetric and consequently $\boldsymbol{l}^p$ is symmetric. For specificity, we take the set of internal variables to be $Q_{\alpha+1} = \boldsymbol{F}^p_{\alpha+1}$. Further, we assume that the free energy admits the additive decomposition

$$W = W^e(\boldsymbol{C}^e, T) + W^p(J^p, T) + W^h(T)\,, \tag{4.11}$$

where

$$\boldsymbol{C}^e = \boldsymbol{F}^{eT}\boldsymbol{F}^e \tag{4.12}$$

denotes the elastic Cauchy-Green tensor and W^e, W^p, and W^h denote elastic energy, stored energy due to plastic work, and thermal energy respectively. The equilibrium relations [13] specify the 1st Piola Kirchoff tensor, the conjugate force to the internal variable, and the entropy as

$$\boldsymbol{P}^e = \frac{\partial W}{\partial \boldsymbol{F}} = \frac{\partial W^e}{\partial \boldsymbol{F}} = 2\boldsymbol{F}^e \frac{\partial W^e}{\partial \boldsymbol{C}^e}\boldsymbol{F}^{e-T}\,, \tag{4.13}$$

$$\boldsymbol{Y} = -\frac{\partial W}{\partial \boldsymbol{F}^p} = \big(\boldsymbol{C}^e \frac{\partial W^e}{\partial \boldsymbol{C}^e} + \frac{\partial W^e}{\partial \boldsymbol{C}^e}\boldsymbol{C}^e\big)F^{p-T} - \frac{\partial W^p}{\partial J^p}J^p\boldsymbol{F}^{p-T}\,, \tag{4.14}$$

and

$$N = -\frac{\partial W}{\partial T}\,. \tag{4.15}$$

Assuming isotropy we obtain the relation

$$\boldsymbol{C}^e \frac{\partial W^e}{\partial \boldsymbol{C}^e} = \frac{\partial W^e}{\partial \boldsymbol{C}^e}\boldsymbol{C}^e\,. \tag{4.16}$$

Local form expressions for conservation laws

We utilize conservation of mass

$$\dot{R} = 0\,, \tag{4.17}$$

conservation of momentum

$$R\dot{V} = \mathrm{Div}\boldsymbol{P} + RB\,, \tag{4.18}$$

conservation of angular momentum

$$\boldsymbol{P}\boldsymbol{F}^T = \boldsymbol{F}\boldsymbol{P}^T\,, \tag{4.19}$$

conservation of energy (in entropy form)

$$T\dot{N} = \boldsymbol{Y}\cdot\boldsymbol{F}^p + RQ - \mathrm{Div}H + \boldsymbol{P}^v\cdot\dot{\boldsymbol{F}}\,, \tag{4.20}$$

where Q denotes the heat generation and H denotes heat conduction. In general we may model a viscous stress

$$\boldsymbol{P}^v = \boldsymbol{P} - \boldsymbol{P}^e \,, \tag{4.21}$$

that derives from a potential

$$\boldsymbol{P}^v = \frac{\partial \phi^*}{\partial \dot{\boldsymbol{F}}} \,, \tag{4.22}$$

however, we will assume in this article that $\phi^* = 0$, i.e., there are no viscous effects. We define the specific heat

$$RC := -T\frac{\partial^2 W}{\partial T^2}(\boldsymbol{F}, \boldsymbol{F}^p, T) \,. \tag{4.23}$$

Differentiating (4.15) we obtain the identity

$$T\dot{N} = RC\dot{T} - T\frac{\partial \boldsymbol{P}}{\partial T} \cdot \dot{\boldsymbol{F}} + T\frac{\partial \boldsymbol{Y}}{\partial T} \cdot \dot{\boldsymbol{F}}^p \,. \tag{4.24}$$

For a given free energy $W(\boldsymbol{C}, T, \boldsymbol{F}^p)$,

$$U(\boldsymbol{C}, N, \boldsymbol{F}^p) = \sup_{\theta} W(\boldsymbol{C}, \theta, \boldsymbol{F}^p) + \theta N \tag{4.25}$$

defines the internal energy. We may relate $\dot{T}$ to $\boldsymbol{l}$ using conservation of energy. From equation (4.20) and (4.23), we obtain

$$RC\dot{T} = T\frac{\partial \boldsymbol{P}}{\partial T}\dot{\boldsymbol{F}} - T\frac{\partial \boldsymbol{Y}}{\partial T}\dot{\boldsymbol{F}}^p + \boldsymbol{Y} \cdot \dot{\boldsymbol{F}}^p + RQ - \mathrm{Div}H + \boldsymbol{P}^v \cdot \dot{\boldsymbol{F}} \,, \tag{4.26}$$

whereupon neglecting terms we obtain

$$RC\dot{T} = T\frac{\partial \boldsymbol{P}}{\partial T}\boldsymbol{l}\boldsymbol{F} + (-T\frac{\partial \boldsymbol{Y}}{\partial T} + \boldsymbol{Y}) \cdot \dot{\boldsymbol{F}}^p - \mathrm{Div}H \,. \tag{4.27}$$

Assuming standard Newtonian heat conduction

$$H = -\partial_G \Delta = -\kappa \boldsymbol{\nabla} \cdot T \,,$$

we obtain

$$RC\dot{T} = T\frac{\partial \boldsymbol{P}}{\partial T}\boldsymbol{l}\boldsymbol{F} + (-T\frac{\partial \boldsymbol{Y}}{\partial T} + \boldsymbol{Y}) \cdot (J^p \boldsymbol{F}^{-1} \boldsymbol{l}^p \boldsymbol{F}) + \kappa \Delta T \,. \tag{4.28}$$

The adiabatic limit is obtained by taking the limit $\kappa \downarrow 0$.

Dissipative and diffusive processes

Let $Z = \{\boldsymbol{F}^p\}$ denote the internal variable list. Let $\Delta(\dot{\boldsymbol{F}}^p, G)$ denote the general dissipation potential and assume a separable additive potential

$$\Delta(\dot{\boldsymbol{F}}^p, G) = \Psi^*(\dot{Z}) + \phi^*(\dot{\boldsymbol{F}}) - \chi(G)\,, \tag{4.29}$$

where $G = -\boldsymbol{\nabla} T/T$. We close the internal variable equations with the following kinetic laws:

$$P^v = \frac{\partial \Delta}{\partial \dot{\boldsymbol{F}}}\,, \tag{4.30}$$

$$\boldsymbol{Y} = \frac{\partial \Delta}{\partial \dot{Z}}\,, \tag{4.31}$$

$$-H = \partial_G \Delta\,. \tag{4.32}$$

We define rate potential function following [87, 104]

$$\begin{aligned}\Phi(\dot{\varphi}, T, \dot{N}, \dot{Z}) = \int_\Omega \big(\dot{U} - T\dot{N} + \Delta(\frac{T}{\theta}\dot{\boldsymbol{F}}, \frac{T}{\theta}\dot{Z}, -\frac{1}{T}\boldsymbol{\nabla} T)\big) dV - \int_\Omega RB \cdot \dot{\varphi} dV \\ - \int_{\partial\Omega_2} \bar{T} \cdot \dot{\varphi} dS + \int_\Omega RQ \log(T/T_0) dV - \int_{\partial\Omega} \bar{H} \cdot n \log(T/T_0) dS\,.\end{aligned} \tag{4.33}$$

Taking variations with respect to $\dot{\varphi}$, T, $\dot{N}$ recovers the above equations.

Relating material and spatial configurations

From deformation power duality we have the identity

$$\boldsymbol{Y} \cdot \dot{\boldsymbol{F}}^p = J\boldsymbol{y} \cdot \boldsymbol{d}^p\,, \tag{4.34}$$

with $\boldsymbol{y} = \boldsymbol{\sigma} - p_c \boldsymbol{I}$ the conjugate force to d^p. Let $\psi(\boldsymbol{d}^p)$ denote the spatial dissipation potential and be related to the material dissipation potential by

$$J\psi^*(\boldsymbol{d}^p) = \Psi^*(\dot{F}^p)\,. \tag{4.35}$$

Free energy density for fused silica glass

We modify the constitutive model recently introduced by [78] to incorporate temperature and rate. We adopt the specific material model free energy where

$$W^e = \frac{\mu(T)}{2}\Big(\Big((J^e)^{-2/3}\Big)\,\mathrm{tr}(\mathbf{C}^e) - 3\Big) + f(J^e, T)\,, \tag{4.36}$$

denotes the elastic dependence and

$$W^h = RC_v^0 T(1 - \log(\frac{T}{T_0}))\,, \tag{4.37}$$

denotes the uncoupled thermal dependence. C_v^0 denotes the deformation identity specific heat. We compute

$$\frac{\partial W^e}{\partial \boldsymbol{C}^e} = \frac{1}{2}\left(\frac{\mu'}{2}(\tilde{I}_1 - 3)J^e + f'J^e - \mu\frac{\tilde{I}_1}{3}\right)(\boldsymbol{C}^{e^{-1}}) + \frac{1}{2}\mu J^{e^{-2/3}}\boldsymbol{I}\,, \tag{4.38}$$

where

$$\mu(J^e) = \begin{cases} a_0(T) + a_1(T)J^e + a_2(T)J^{e^2}, & J^e \geq J_c^p, \\ b_1(T)\exp(b_2(T)(J^e - 1)) + b_3(T), & \text{otherwise}, \end{cases} \tag{4.39}$$

and

$$f(J^e) = \begin{cases} \dfrac{c(T)}{2}(J^e - 1)^2, & J^p \geq J_c^p, \\ \dfrac{d_1(T)}{2}(J^e - 1)^2 + \dfrac{d_2(T)}{4}(J^e - 1)^4 + \dfrac{d_3(T)}{6}(J^e - 1)^6, & \text{otherwise}\,, \end{cases} \tag{4.40}$$

are the pressure dependent shear modulus and bulk modulus.

Temperature dependence of the elasticity parameters

We assume the form of continuous piecewise linear functions for the temperature dependence of the finite deformation elastic moduli

$$\begin{aligned} &a_0(T) = a_0^0 + a_0^1(T - T_0)\ ,\ a_1(T) = a_1^0 + a_1^1(T - T_0)\ , \\ &a_2(T) = a_2^0 + a_2^1(T - T_0)\ , \end{aligned} \tag{4.41}$$

$$\begin{aligned} &b_1(T) = b_1^0 + b_1^1(T - T_0)\ ,\ b_2(T) = b_2^0 + b_2^1(T - T_0)\,, \\ &b_3(T) = b_3^0 + b_3^1(T - T_0)\,, \end{aligned} \tag{4.42}$$

and

$$c(T) = c_1^1 + c_1^2(T - T_0)\,. \tag{4.43}$$

$$d_j(T) = \begin{cases} d_j^{1a} + d_j^{2a}(T - T_0) & T \leq T_t \\ d_j^{1b} + d_j^{2b}(T - T_0) & T > T_t \end{cases}\,. \tag{4.44}$$

However, for the data under present study, there is very little temperature dependence for the $b_j(T)$ functions and we take them to be constants with respect to temperature letting $b_j^1 = 0$ for $j = 1, 2, 3$. We refer the reader to [77] for values of b_j^0 which are independent of temperature.

Consolidation relation

We parameterize the effect of temperature on the consolidation curve by linear dependence on the temperature.

$$p_c = -\frac{J^p}{J}\frac{\partial W^p}{\partial J^p} = p_0 + \frac{A^0}{\alpha}(1 - J^{p-\alpha}) + A^1 \exp(\frac{m_0(J_c - J_p)(T - T_0)}{J_c}) , \quad (4.45)$$

where $A^1,\ A^0$ are fit to the consolidation curves at different temperature.

Limit surface, dissipation potential and elastic region

We remark that the above model incorporates the effect of rate for silica glass

$$\psi^*(d^p) = \sup_{\sigma \in K(T)} \sigma \cdot d^p ,$$

and the temperature dependent elastic domain $K(T)$ is given below.

The dissipation potential $\Psi^*(\dot{\boldsymbol{F}}^p)$ is related to the dissipation potential per unit deformed volume $\psi^*(\boldsymbol{d}^p)$ by

$$\Psi^*(\dot{\boldsymbol{F}}^p) = J\psi^*(\boldsymbol{F}^e \dot{\boldsymbol{F}}^p \boldsymbol{F}^{p^{-1}} \boldsymbol{F}^{e^{-1}}) . \quad (4.46)$$

To obtain the dissipation potential per unit deformed volume, we consider the elastic region

$$K = \{\boldsymbol{y} \in \mathbb{R}^{3\times3}_{\text{sym}} | \left(\frac{2p_y + p_c - p_t}{p_c - p_t}\right)^2 + \left(\frac{q}{q_c}\right)^2 = 1; p_y = -\frac{\text{tr}(\boldsymbol{y})}{3}; q = \sqrt{\frac{3}{2}\text{dev}\boldsymbol{y} \cdot \text{dev}\boldsymbol{y}}\} . \quad (4.47)$$

We recall that $y = \sigma + p_c \boldsymbol{I}$ so in particular, $p_y = p - p_c$ where $p = -\frac{1}{3}\text{tr}(\sigma)$. The corresponding dissipation function follows from convex duality as

$$\psi^*(\boldsymbol{d}^p) = \sup_{\boldsymbol{y} \in K} \boldsymbol{y} \cdot \boldsymbol{d}^p . \quad (4.48)$$

Thus,

$$\boldsymbol{d}^p \in \partial I_K(y) , \quad (4.49)$$

where I_K is the indicator function for the set K and ∂ denotes the subdifferential of convex analysis [73]. If the boundary of K is smooth, then $\partial I_K(\boldsymbol{y})$ is the normal to the set K. Let

$$f = \alpha^2 \big(\frac{2p + p_c - p_t}{2}\big)^2 + q^2 - q_c^2 , \quad (4.50)$$

where $\alpha = \dfrac{2q_c}{p_c - p_t}$.

Fitting the parameters to temperature and rate data

The parameters from the preceding sections are fit to MD data and are given in Tables 4.1, 4.2, and 4.3.

Table 4.1: Pressure Dependent Shear Modulus Parameters

a_0	a_1	a_2	b_1	b_2	b_3
347.15 GPa	-745.82 GPa	426.46 GPa	0.20773 GPa	-19.498	34.6439 GPa

Table 4.2: Volumetric Elastic Energy Dependence

c_1^1	c_1^2	T_t
-33.75 GPa	-0.01110 GPa	600 K

Table 4.3: Volumetric Elastic Energy Dependence

j	d_j^{1a} (GPa)	d_j^{2a} (GPa/K)	d_j^{1b} (GPa)	d_j^{2b} (GPa/K)
1	-25.2668	0.0655647	-1.15341	-0.0148131
2	-1915.58	3.25853	-1272.14	1.11374
3	0.0	-26.5007	-7997.01	0.155963

Consolidation curve

In addition, the tensile failure stress p_t specifies the maximum tensile pressure at which the glass sample is stable, thereby providing a lower bound on the initial consolidation pressure. These constants are tabulated in Table 4.4.

Table 4.4: Hardening parameters

A	α	p_0	p_t
-8.48613 GPa	9.2689	3.02934 GPa	−8.5 GPa

Table 4.5: Hardening thermal parameters

A^1	J_c^p	m_0
0.323492 GPa	0.853702	0.0427932

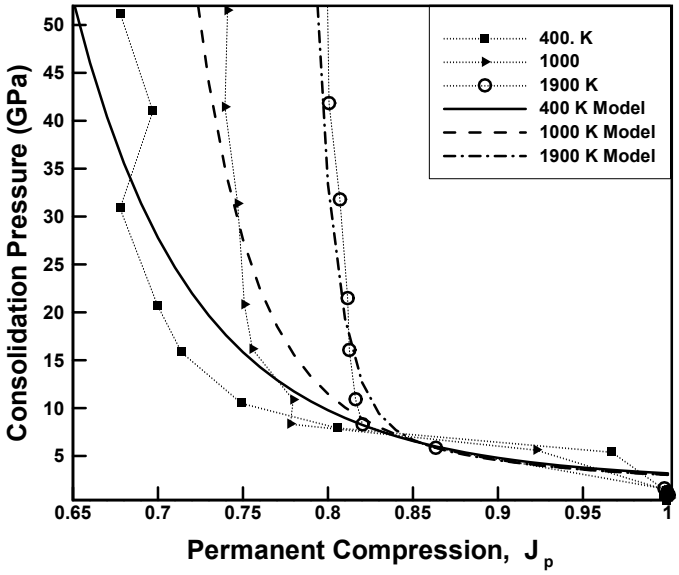

Figure 4.9: We display goodness of fit for the pressure consolidation relation.

The critical state line (limit surface)

We now identity the critical state line. The shear yield stress decreases as a function of temperature. Assuming a separable function, the shear yield stress at critical state is given by

$$q_c(p_m, T) = q_c^0(p_m)\xi(T)w(\dot{\gamma})\,, \tag{4.51}$$

where for instance ξ may take the form $\xi(T) = \exp(-k_2(T - T_0))$ or $\xi = (T/T_0)^\nu$ to be fit to the shear-temperature data. For fixed rate and temperature the tensile regime of the critical-state line is well-represented by a linear relation (capped vertically at $p = p_t$), the compressive regime of the critical-state line is in turn well-presented by a power law, and these are interpolated by a rank-2 connection which ensures the

corresponding limit surface is symmetric div-quasiconvex [78]

$$q_c^0 = \begin{cases} \frac{p_1 - p}{p_1 - p_t}\, q_t, & p \le p_1 \\ \left(s + \frac{3}{4}(p - r)^2\right)^{1/2} & p_1 \le p \le p_2 \\ B p^\beta & p_2 \le p \end{cases} \tag{4.52}$$

The corresponding values of the constants are tabulated in Tables 4.6 and 4.7.

Table 4.6: Critical state line constants

q_t	p_t	B	β
7.402 GPa	−8.5 GPa	1.168 $\sqrt{\text{GPa}}$	0.5

Table 4.7: Critical state line constants specific to rank two connection

p_1	p_2	r	s
4.141 GPa	6.084 GPa	5.176 GPa	7.674 GPa^2

For the specific model where the temperature and thermal dependence are described by power laws $\xi(T) = (T/T_0)^\nu$ and $w(\dot\gamma) = c(\dot\gamma)^m$, we obtain the scaling exponents presented in table 4.8. These exponents characterize the competition between

Table 4.8: Thermal and shear rate critical state line exponents

ν	m	c
−0.259	0.0325	0.700

thermal softening and strain rate hardening. Analysis following [60] immediately suggest that fused silica glass may exhibit shear localization. This is a critical issue requiring analysis in and of itself and we are pursuing this line of inquiry in a concurrent study [81]. Power laws are highly appealing in their simplicity, however, the previous fit consistently *underestimates* thermal softening at low strain rates. This is due to a subtle coupling between the temperature and rate dependence. A simple extension of this model is an enhanced power law model where the exponents may depend (e.g. linearly) on additional variables. We propose such a candidate as

$$q_c(p_m, T, \dot\gamma) = q_c^0(p_m)\chi(T, \dot\gamma)\,,$$

where

$$\chi(T,\dot{\gamma}) := c_1 \left(\gamma_0 \dot{\gamma}^{m_1+m_2 T} + 1\right) \left(\frac{T}{T_0}\right)^{\nu_2 \log(\dot{\gamma})+\nu_1} ,$$

gives the coupled thermal and rate dependence.

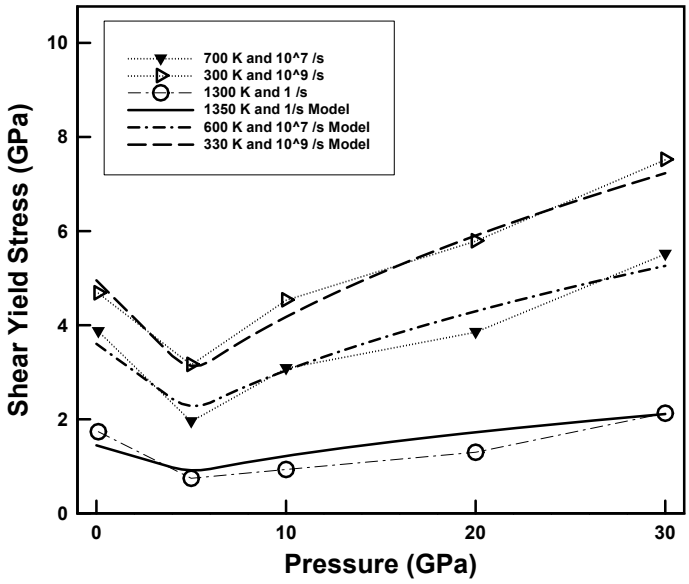

Figure 4.10: Shear yield stress are plotted versus pressure for several temperatures and strain rates.

Table 4.9: Thermal and shear rate critical state line parameters more sophisticated model.

ν_1	m_1	ν_2	m_2	γ_0	c_1
-0.70	0.462	0.0288	5.26×10^{-6}	0.0000141	0.942

Evidently, though the model is slightly more complicated, the fit of the model to the data is improved by the addition of free parameters as evidenced by several demonstrative curves displayed in Fig. 4.10. To verify that the the full model is capable of capturing the MD data, we select several different loading paths and compute the material response. In Fig. 4.11, we exhibit the pressure compression behavior for two different examples. In Fig. 4.12, we exhibit the shear deformation for several different examples. Evidently, the model captures the general behavior quite well. We emphasize that the MD data is noisy and we are applying a low dimensional model to capture the response of a very high dimensional data set. We

remark that it is possible for the non-critical state type behavior, i.e. consolidation driven by shear in an under-consolidated sample, to effect the precise values during the early loading in shear. It is possible that the small deviations seen in Fig. 4.12 are caused by this type of behavior.

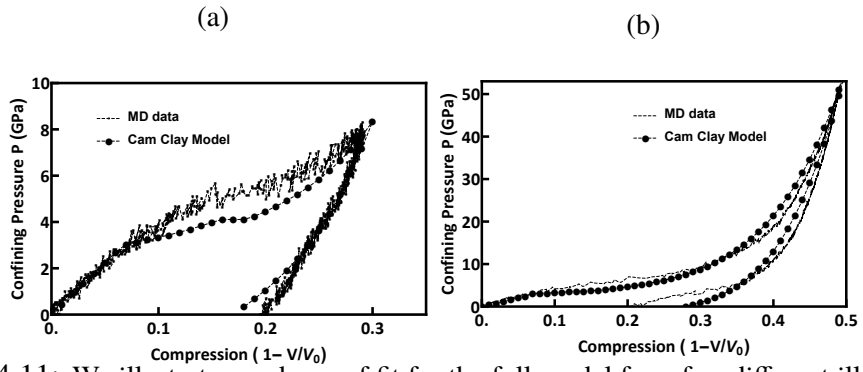

Figure 4.11: We illustrate goodness of fit for the full model for a few different illustrative temperatures and pressures. Evidently the fit is rather good for such a low dimensional model in such a high dimensional data space.

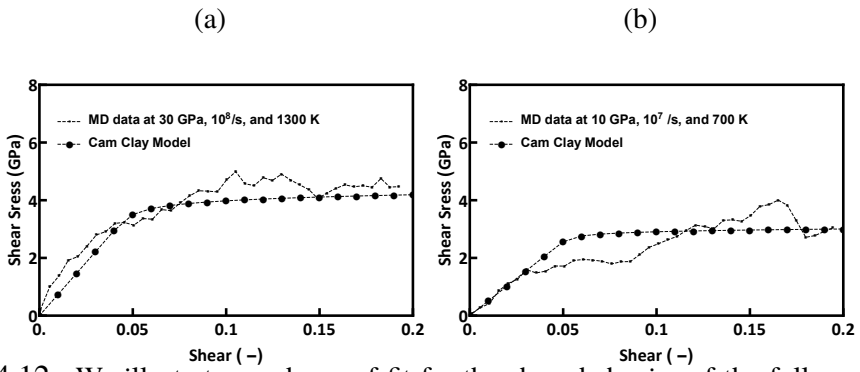

Figure 4.12: We illustrate goodness of fit for the shear behavior of the full model for a few different illustrative temperatures, pressures, and strain rates. Evidently the fit is rather good for such a low dimensional model in such a high dimensional data space.

4.4 Relaxation and interpretation of robustness of the anomalous yield behavior

We now turn to the structure of the critical state line and examine its relationship with microstucture in stress space. We will find that micromechanically glass may support fine mixtures of stress and that the anomalous critical state line is the correct macroscopic model to account for this physics. We begin by defining the *limit domain* to be the set in stress space to which the elastic domain will evolve

at constant loading and refer to Fig. 4.13. The *limit surface* is its boundary. For a Cam-Clay model, the critical state line defines the limit surface. We appeal to notions from the Direct Methods in the Calculus of Variations following the account found in [15] or [78] and couch the problem within the framework of limit analysis [49].

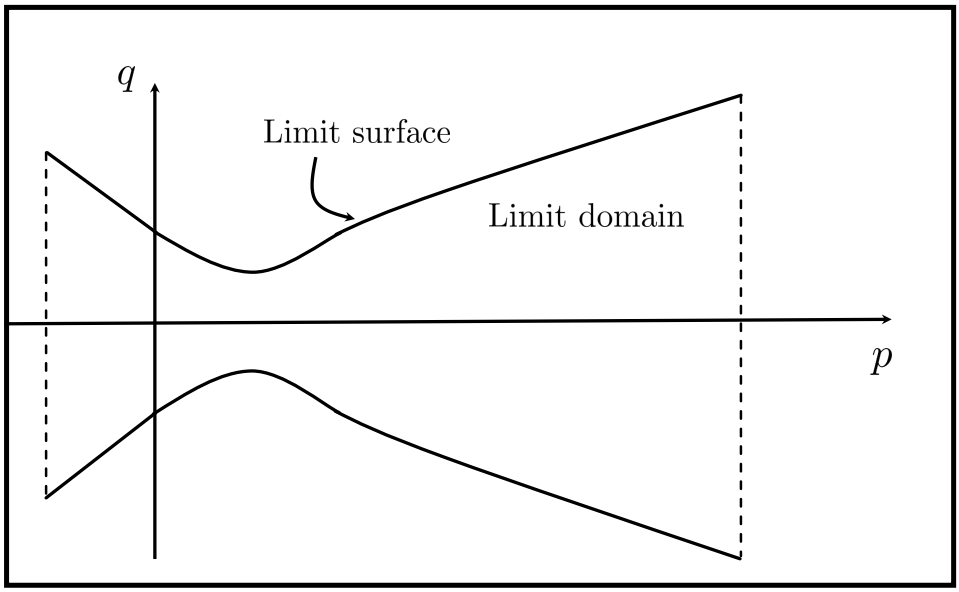

Figure 4.13: The limit domain is the set in stress space to which the elastic domain will evolve at constant loading. The limit surface is its boundary. For a Cam-Clay model, the critical state line defines the limit surface.

Thus, we assume that the solid deforms plastically at constant applied load. We call these conditions *collapse* and consequently the instantaneous behavior of the solid is rigid and ideally plastic, i.e., no instantaneous hardening takes place (ideal plasticity) and (rigid-plastic behavior)

$$\boldsymbol{d}^p = \frac{1}{2}(\nabla \boldsymbol{v} + \nabla \boldsymbol{v}^T)\,, \tag{4.53}$$

where $\boldsymbol{v} : \Omega \to \mathbb{R}^3$ is the velocity field and Ω is the domain of the solid at collapse. The corresponding kinematic and static problems of limit analysis [49] can then be jointly expressed as the saddle-point problem

$$\inf_{\boldsymbol{v}} \sup_{\boldsymbol{\sigma}} \left\{ \int_\Omega \boldsymbol{\sigma} \cdot \nabla \boldsymbol{v}\, dx \;:\; \boldsymbol{\sigma}(x) \in K(J^p(x)),\ \boldsymbol{v} = \boldsymbol{g} \text{ on } \partial\Omega \right\}, \tag{4.54}$$

where the minimization and maximization take place over suitable spaces of velocities and stresses, respectively, J^p accounts for the state of consolidation of the

solid, $\boldsymbol{g}$ is a prescribed velocity field over the boundary and we assume that the solid is free of body forces. We recall that the inner maximum problem in (4.54) embodies Drucker's principle of maximum dissipation and the static principle of classical plasticity, whereas the outer minimum problem embodies the kinematic principle of classical plasticity.

Alternatively, this saddle problem may be viewed as the limit of the theory of variational constitutive updates [64] and a direct specialization of equation (5.29) to the case of constant temperature and vanishing of the rate of elastic deformation. The stress field must be in equilibrium, $\operatorname{div}\boldsymbol{\sigma} = \mathbf{0}$, whereupon (4.54) reduces to the static problem via an application of the Divergence Theorem

$$\sup_{\boldsymbol{\sigma}} \left\{ \int_{\partial\Omega} \boldsymbol{\sigma}\boldsymbol{\nu} \cdot \boldsymbol{g}\, d\mathcal{H}^2 \;:\; \boldsymbol{\sigma} \in K,\ \operatorname{div}\boldsymbol{\sigma} = \mathbf{0} \right\}. \tag{4.55}$$

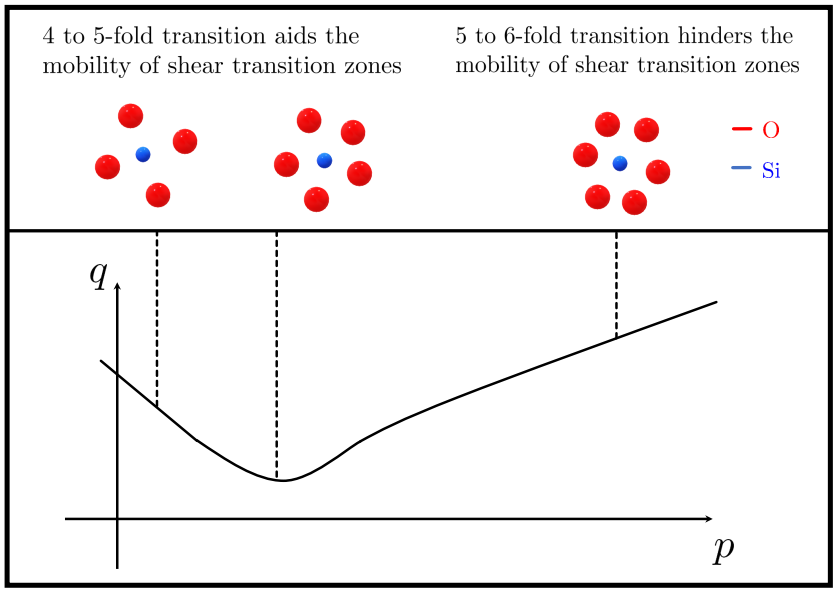

Figure 4.14: We provide a possible atomistic mechanism for the anomalous yield behavior. As the glass is loaded to higher pressures it undergoes a rearrangement in coordination number typically increasing – on average – from 4-fold to 5-fold to 6-fold symmetry. The shear deformation in silica is accommodated by shear transition zones (STZ). The mobility of these STZ is aided during by the transition from 4-fold to 5-fold symmetry. Conversely, the transition from 5-fold to 6-fold symmetry hinders the STZ mobility. This type of process is consistent with more classical dependence of the shear strength on pressure such as Steinberg Guinan.

In the present setting, the appropriate notion to characterize the elastic domain K is *symmetric div-quasiconvexity* [15, 25]. For the case of Silica glass, we interpret the

molecular dynamics data as indicating that the elastic domain K is not stable against the formation of micro-mechanical residual stresses. Thus, the supremum in (4.55) may be attained arbitrarily closely by weakly-convergent sequences of stress fields, but the supremum itself may not be attained by any one stress field. The weakly-convergent maximizing sequences are typically characterized by increasingly fine microstructure.

However, the appropriate macroscale model to use for the critical state line is the *symmetric div-quasiconvex* envelope which is given explicitly and exactly in the form of equation (4.52). This ensures that continuum calculations will be stable against fine fluctuations in the stress field. See [15, 78] for specifics. Therefore, we expect the subscale physics to exhibit fluctuations reminiscent of optimizing sequences. We provide a possible atomistic mechanism for the anomalous yield behavior. As the glass is loaded to higher pressures it undergoes a rearrangement in coordination number typically increasing – on average – from 4-fold to 5-fold to 6-fold symmetry. The shear deformation in silica is accommodated by shear transition zones (STZ). The mobility of these STZ is aided during by the transition from 4-fold to 5-fold symmetry. Conversely, the transition from 5-fold to 6-fold symmetry hinders the STZ mobility. This latter type of process is more classical and is consistent with typical dependence of the shear strength model on pressure such as, for instance, the Steinberg-Guinan model.

We now provide two simple examples illustrating possible (though by no means unique) maximizing sequences.

Example 4.4.1 *We illustrate in Fig. 4.15 a possible pattern that would form a sequence of stress states supremizing the plastic dissipation.*

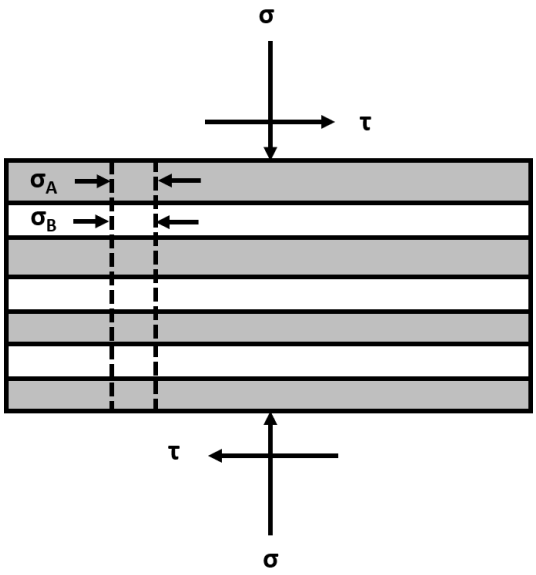

Figure 4.15: Rank 2 lamination relaxes non-convex stress space.

In particular, consider the following two stress states

$$\boldsymbol{\sigma}_A = \begin{bmatrix} \sigma_A & 0 & 0 \\ 0 & \sigma_A & \tau \\ 0 & \tau & \sigma \end{bmatrix},$$

and

$$\boldsymbol{\sigma}_B = \begin{bmatrix} \sigma_B & 0 & 0 \\ 0 & \sigma_B & \tau \\ 0 & \tau & \sigma \end{bmatrix}.$$

Computing the pressure

$$p_B = \frac{\sigma + 2\sigma_B}{3},$$

and

$$p_A = \frac{\sigma + 2\sigma_A}{3},$$

and the deviatoric stress

$$q_A = \sqrt{|\sigma - \sigma_A|^2 + 3\,|\tau|^2},$$

and

$$q_B = \sqrt{|\sigma - \sigma_B|^2 + 3\,|\tau|^2}.$$

Equating $q_A = q_B$, we obtain

$$\sigma = \frac{1}{2}(\sigma_A + \sigma_B)\,,$$

(for otherwise $\sigma_A = \sigma_B = \sigma$ which is the trivial case). These two equibiaxial stresses σ_A and σ_B, up to small corrections at the boundaries remain in equilibrium. Thus, these states may be finely mixed to any degree.

Example 4.4.2 *We now consider the loading geometry presented in Fig. 4.16.*

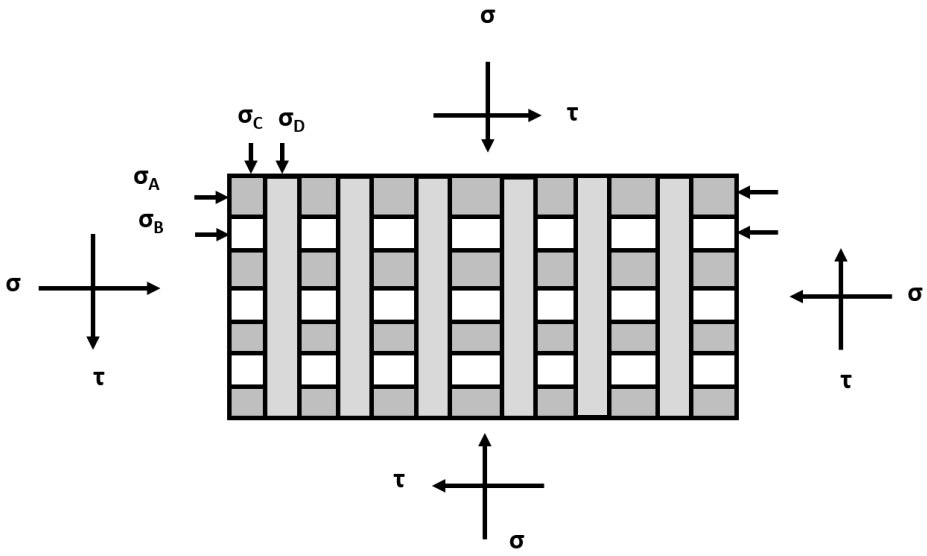

Figure 4.16: Rank-2 tiling relaxes non-convex stress space.

We require that the stress states satisfy the average stress conditions specified by

$$2\sigma = \sigma_A + \sigma_B\,,$$

and

$$2\sigma = \sigma_C + \sigma_D\,.$$

This loading results in four different stress regions

$$\boldsymbol{\sigma}_{AC} = \begin{pmatrix} \sigma_C & \tau & 0 \\ \tau & \sigma_A & 0 \\ 0 & 0 & \sigma \end{pmatrix},$$

$$\boldsymbol{\sigma}_{AD} = \begin{pmatrix} \sigma_D & \tau & 0 \\ \tau & \sigma_A & 0 \\ 0 & 0 & \sigma \end{pmatrix},$$

$$\boldsymbol{\sigma}_{BC} = \begin{pmatrix} \sigma_C & \tau & 0 \\ \tau & \sigma_B & 0 \\ 0 & 0 & \sigma \end{pmatrix},$$

and

$$\boldsymbol{\sigma}_{BD} = \begin{pmatrix} \sigma_D & \tau & 0 \\ \tau & \sigma_B & 0 \\ 0 & 0 & \sigma \end{pmatrix}.$$

The weak limits of these stress states as the loading spacing size goes to 0 *results in the average stress consistent with*

$$\boldsymbol{\sigma} = \begin{bmatrix} \sigma & 0 & 0 \\ 0 & \sigma & \tau \\ 0 & \tau & \sigma \end{bmatrix}. \tag{4.56}$$

Computing the pressure and deviatoric shear

$$q_{AC} = \frac{\sqrt{|2\sigma - \sigma_A - \sigma_C|^2 + |\sigma - 2\sigma_A + \sigma_C|^2 + |\sigma + \sigma_A - 2\sigma_C|^2 + 18\,|\tau|^2}}{\sqrt{6}},$$

$$q_{BC} = \frac{\sqrt{9\left|\sigma - \frac{2\sigma_A}{3} - \frac{\sigma_C}{3}\right|^2 + |-3\sigma + \sigma_A + 2\sigma_A|^2 + |\sigma_A - \sigma_C|^2 + 18\,|\tau|^2}}{\sqrt{6}},$$

$$q_{AD} = \frac{\sqrt{9\left|\sigma - \frac{\sigma_A}{3} - \frac{2\sigma_C}{3}\right|^2 + |-3\sigma + 2\sigma_A + \sigma_C|^2 + |\sigma_A - \sigma_C|^2 + 18\,|\tau|^2}}{\sqrt{6}},$$

$$q_{BD} = \frac{\sqrt{|-2\sigma + \sigma_A + \sigma_C|^2 + |\sigma - 2\sigma_A + \sigma_C|^2 + |\sigma + \sigma_A - 2\sigma_C|^2 + 18\,|\tau|^2}}{\sqrt{6}},$$

$$p_{AC} = \frac{1}{3}(\sigma + \sigma_A + \sigma_C), \quad p_{BC} = \frac{1}{3}\left(2\left(\sigma - \frac{\sigma_A}{2}\right) + \sigma + \sigma_C\right),$$

$$p_{AD} = \frac{1}{3}\left(2\left(\sigma - \frac{\sigma_C}{2}\right) + \sigma + \sigma_A\right),\ p_{BD} = \frac{1}{3}\left(2\left(\sigma - \frac{\sigma_A}{2}\right) + 2\left(\sigma - \frac{\sigma_C}{2}\right) + \sigma\right)\ .$$

σ_A and σ_C may be selected such that no points in the body actually coincide with the point σ.

To best illustrate the behavior of the silica glass plasticity, we examine a strong simplification of the model. We select a model where only the four points considered above in p, q space are admissible – AC, AD, BC, and BD – see the region denoted in gray in Fig. 4.17. We inquire whether or not the solid support a macroscopic load at stress state $\boldsymbol{\sigma}$ with $\sigma = 2$ GPa and $\tau = 1$ GPa. This is indicated as an open triangle in Fig. 4.17. It is easy to see that successively smaller tiling in the manner introduced above results in sequences that converge weakly to $\boldsymbol{\sigma}$.

From the more viewpoint of symmetric-div-quasiconvexity (see [15, 24]), this weakly converging sequence representation of the stress state constitutes a Young measure. In particular, we examine – using the explicit and exact curve corresponding to the anomalous critical state lines – first and second order connections between these stress states. In Fig. 4.17, we show that regions AC and AD have a weak limt and that BC and BD have a weak limit. In turn, these weak limits finely mix to converge to $\boldsymbol{\sigma}$.

The preceding examples provide the following insight into the behavior of silica glass: the microscopic yield behavior corresponding to the macroscopic anomalous yield behavior is a *fine mixture* of micro-stress states. These examples could be generalized to finely mixed loading in higher dimensions. However, the principle motif of the sub-scale physics deformations is well illustrated by these simple and highly tractable cases.

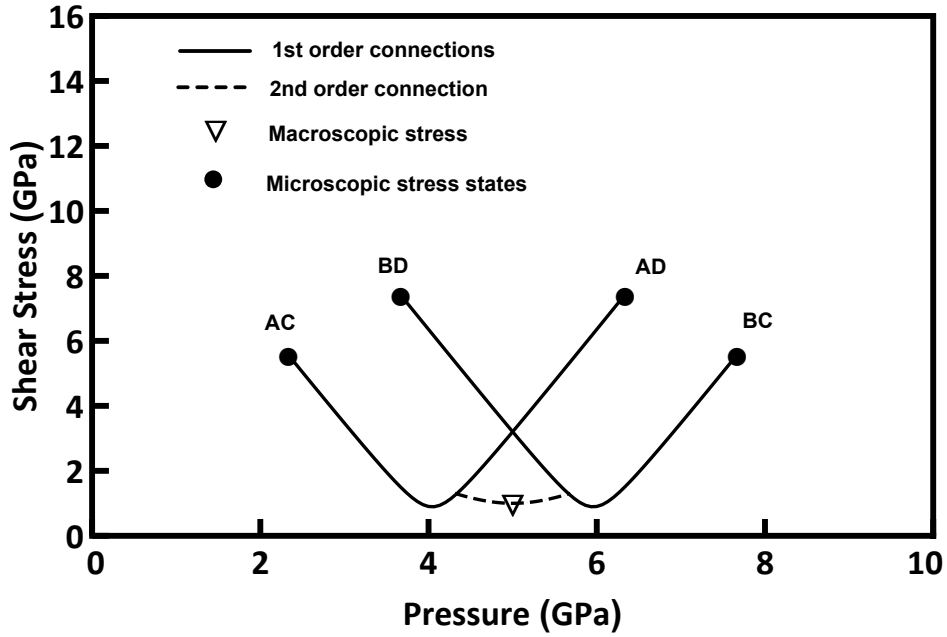

Figure 4.17: The macroscopic stress state – even if it is not in the limit domain – can be represented by combinations of other stress states which are in the limit domain. We refer to the graphic in Fig. 4.16. By first order connections, we refer to the stress states remaining in equilibrium along the horizontal direction and by first order connection, we refer to stress states remaining in equilibrium along the vertical directions. Here, we show that the macroscopic stress state can be represented by the rank-two combination of 4 different stress points. This particular example is far from unique – there are many possible combinations of stress states that could represent the macroscopic stress state.

4.5 Summary and concluding remarks

In this study, we have implemented a multiscale modeling program that succeeds in extending and calibrating a Cam-Clay model of plasticity (originally derived in [78]) for fused silica glass which accounts for the thermal and rate dependence of the media directly from data mined at the atomistic level using both molecular dynamics and max-ent atomistics.

The molecular scale calculations indicate that there is a substantial degree of permanent densification consistent with findings reported in [77] and references therein. This permanent densification displays a strong quantitative dependence on temperature. We find the yield strength of silica to be a decreasing function of the temperature and an increasing function of the rate of shear strain.

We quantify this dependence and find that the material model developed herein captures the MD data well. Moreover, the MD data exhibits anomalous yield

behavior in the sense that it displays a non-monotonic relationship between the shear yield stress and the pressure. This non-monotonic dependence corresponds to a non-convex limit domain in the sense of limit analysis. Silica glass is the first example (to our knowledge) of a non-convex elastic domain derived from micro-mechanics. Furthermore, we have found that though this process is quantitatively dependent on temperature and rate, the non-convexity nonetheless holds for all regimes probed in this study. Thus, the relaxation of the non-convex limit domain and the corresponding rigorous connection between micro-structural patterning and the non-monotonicity of the critical state line is extremely robust with respect to these varied conditions.

There are several follow-up questions that are beyond the scope of the current study but are suggested by it. For instance, there are many soda lime glasses which are mostly SiO_2 with some additional constituents such as Mg, Na, or Ca. It would be a valuable contribution to quantify – in a similar manner to this study – the effect of chemical concentration of such added constituents on the inelastic material behavior. Additionally, it is an interesting question to find other material systems that would be modeled well by a critical state theory with a non-monotonic critical state line. Finally, a common motif in temperature dependent material models is the occurrence of shear localization due to thermal softening and it would be natural to wonder if such processes should occur in silica. In a concurrent study [81], the authors investigate this possibility of the formation of shear bands in amorphous silica, thereby introducing meso-scale microstructure formation and evolution in the deformation field.

Acknowledgements

This work was supported by a NASA Space Technology Research Fellowship.

Chapter 5

SHEAR LOCALIZATION

Research presented in this chapter has been adapted from [81].

5.1 Introduction

Silica glass is one of the most commonly used glassy materials in engineering and its material properties have been a long-standing topic of investigation. However, it exhibits several anomalous behaviors (see [78] and references therein) under extreme pressure. Specifically, silica exhibits both non-monotonic dependence on pressure of the elastic moduli [35] as well as a significant decrease in strength in certain regimes as it is compressed to denser structures with higher coordination [57]. In [78], the anomalous yield behavior was given the interpretation of a *non-convex limit surface* in the sense of limit analysis of classical critical state plasticity theory [49]. In a concurrent study [80], this model was extended to incorporate the effect of temperature and rate by mining data from molecular dynamics simulations. For completeness and continuity with this study, we reproduce several examples showing goodness of fit and display them in Fig. 5.1. In particular, in Fig. 5.1(B), we illustrate the anomalous yield behavior evident in the MD data. The anomalous yield behavior arises as a mesoscale consequence of fine stress-field fluctuations.

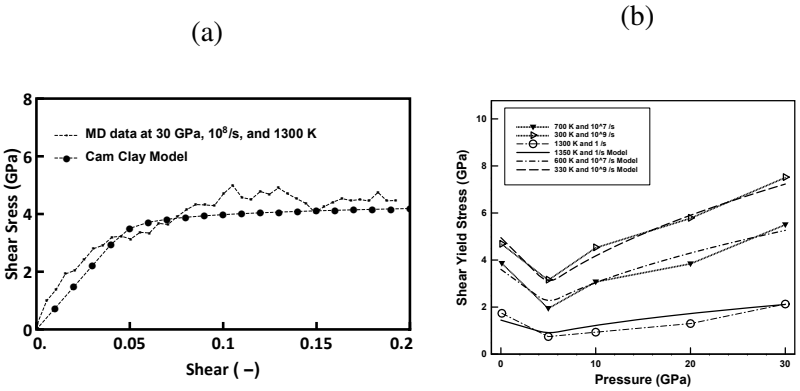

Figure 5.1: We reproduce several plots from [80] that illustrate goodness of fit for the shear behavior of the full model. (A) We show the shear stress shear strain relationship as compared to molecular dynamics data. (B) The yield stress exhibits a non-monotonic dependence on pressure and matches the molecular dynamics data well.

Various experimental studies of failure waves in silica and soda-lime glass through angled flyer plate impact experiments support this viewpoint [1, 12, 84, 90]. However, these studies also include instances where the experimental conditions – such as temperature and strain rate – are quantitatively different from those computed in [78]. Additionally, it appears that under different conditions the inelastic mechanical response of glass may be dramatically different and may involve microstructured deformation such as *shear strain localization* [54]. Though small relative to the macro-scale, these deformations are *large* relative to any atomistic calculations. It is well known, (c.f. for instance [20] for an introduction) that the determination of shear localization is highly dependent on temperature and strain rate.

We aim to characterize conditions under which this localization will occur and predict its effect at the macroscale. We envision, c.f. Fig. 5.2, that the solid will accommodate deformation by localizing shear deformation into a small number of localized regions or *shear bands* which will experience a large shear and local temperature increase. These shear bands, though much smaller than the macroscale, are much larger than the atomistic calculations which were used to parameterize the continuum model of [80].

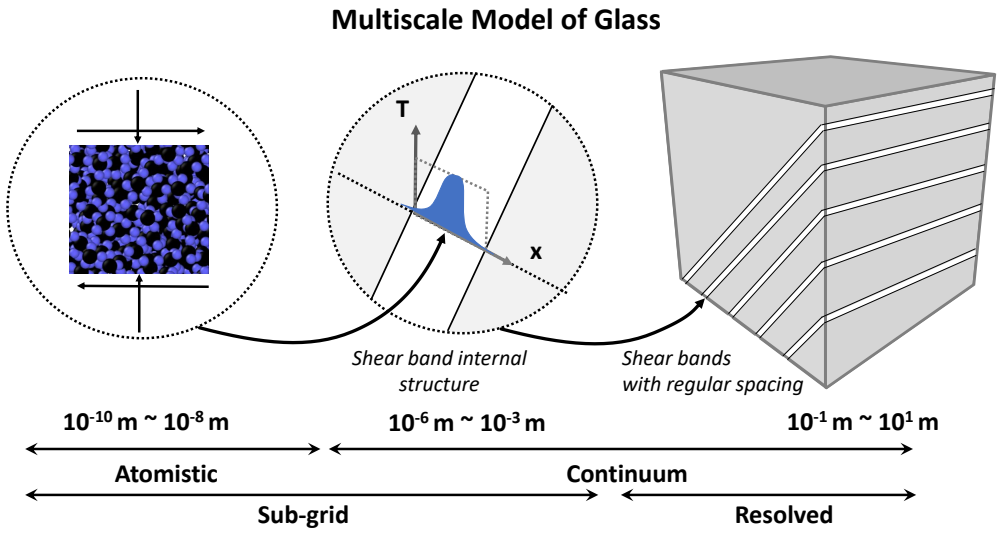

Figure 5.2: The inelastic deformation of glass is inherently multiscale.

We develop a novel single branch rank-one convexification strategy which jointly accounts for the optimal microstructure of the small scale physics. This could be

viewed as an extension of Miehe's work [59] or an application of Aubry *et al.* [5] truncated at the first laminate.

The goal of this study is to characterize the tendency of fused silica glass to undergo shear localization using a model due to [80] which accounts for the temperature and rate dependence. Specifically, we consider shear localization along rank-one lines and find that silica glass admits shear bands. This is remarkable – in a theoretical sense – as silica glass is a material that apparently admits microstructure in both the deformation and stress fields. We provide examples of the behavior of this Cam-Clay theory of plasticity at both critical and non-critical state. We finish by comparing the results of our model to experiment and find good agreement.

The remainder of this paper is organized as follows. In section 5.2, we present a classical analysis of shear localization based on finite time blowup arguments. In section 5.3, we briefly review the finite deformation formulation of mechanics and introduce a variational rate formulation. In section 5.4, we introduce an incremental variational formulation and consider adiabatic shear localization. Here, we find that there is no limiting small-length-scale and thus the localization proceeds uncontrollably. Mathematically this corresponds to a loss of coercivity. In section 5.5, we introduce a joint optimization procedure to solve for both the subscale structure and the volume fraction of shear banded material simultaneously. This procedure predicts reductions in stress consistent with measurements obtained in flyer plate impact experiments.

5.2 Shear localization conditions by finite time blow-up

By way of introduction, we establish that fused silica glass may admit shear localization following a classical analysis strategy due to Molinari and Clifton [60]. We recall the elastic region for silica glass is given by the Cam-Clay model [78]

$$K = \{\boldsymbol{y} \in \mathbb{R}^{3\times 3}_{\text{sym}} | \left(\frac{2p_y + p_c - p_t}{p_c - p_t}\right)^2 + \left(\frac{q}{q_c}\right)^2 = 1; p_y = -\frac{\text{tr}(\boldsymbol{y})}{3}; q = \sqrt{\frac{3}{2}\text{dev}\boldsymbol{y} \cdot \text{dev}\boldsymbol{y}}\} \,. \tag{5.1}$$

We illustrate the paramterization of the model in Fig. 5.3. p_c denotes the consolidation pressure, p_t denotes the maximum tensile pressure, and q_c denotes the shear at critical state, i.e. the shear stress at the top of the ellipse in Fig. 5.3. q_c is taken to be a function of $p_m = (p_t + p_c)/2$ and this relation is called the *critical state line*. p_c is taken to be a function of the permanent volumetric consolidation, J^p, and this relation is known as the consolidation relation. We refer the reader to

[78] for further details concerning this model and a more detailed discussion of its behavior and development.

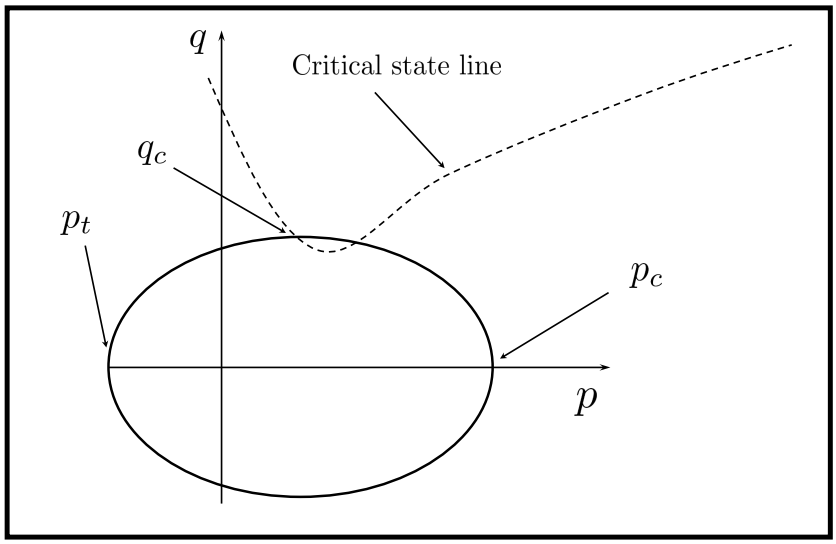

Figure 5.3: We illustrate the elastic domain of the Cam-Clay model.

Case of pure shear

If we fix $p_y = \dfrac{p_t - p_c}{2}$ (i.e. $p = p_m$), then the reduced elastic region is

$$K = \{y \in \mathbb{R}^{3\times 3}_{\text{sym}} \mid \ q < q_c \ \text{ and } p_y = \frac{p_t - p_c}{2}\}\,,$$

which constitutes a Mises yield surface for each fixed pressure. We recall that the model due to [80] states

$$q_c = q_c^0(p_m(J^p))\xi(T)w(\dot{\gamma}^p)\,,$$

where γ^p denotes the plastic shear strain, $\xi(T)$ is a generic function of temperature, and $w(\dot{\gamma}^p)$ is a generic function of strain rate. Assuming a state of pure shear equilibrium, see Fig. 5.4, between any two points A and B, we obtain

$$\tau^A l_A = \tau^B l_B\,, \tag{5.2}$$

where τ^A denotes the shear component of the Cauchy stress tensor and l_A denotes the width of the body at a point A. Conservation of energy gives

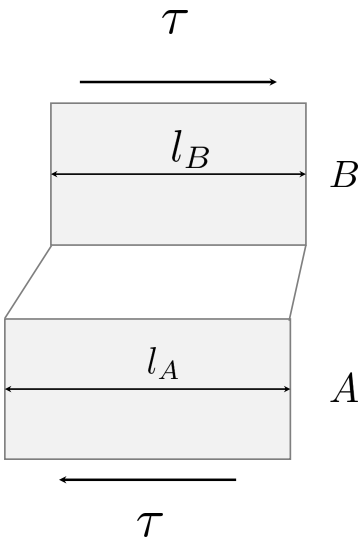

Figure 5.4: We illustrate simple shear.

$$Rc_v\dot{T} = \beta\tau\dot{\gamma}^p + \kappa\Delta T\,, \tag{5.3}$$

where Δ denotes the the Laplace operator and β is a Taylor-Quinney coefficient. Upon taking the limit $\kappa \downarrow 0$ and inserting the constitutive law, we recover

$$Rc_v\dot{T} = \beta q_c^0(p_m)\xi(T)w(\dot{\gamma}^p)\dot{\gamma}^p\,, \tag{5.4}$$

at each point in the body. We examine the limits of large $\dot{\gamma}^p$ such that $g(\dot{\gamma}^p) \approx (\dot{\gamma}^p)^m$, then

$$(\dot{\gamma}^p)^m = \left(\frac{Rc_v\dot{T}}{\beta q_c^0 f(T)}\right)^{\frac{m}{m+1}}\,.$$

Inserting this into (5.2) we obtain after some manipulations

$$l_B^{(m+1)/(m)} f(T_B)^{1/m}\dot{T}_B = l_A^{(m+1)/(m)} f(T_A)^{1/m}\dot{T}_A\,,$$

from which upon assuming sufficient regularity, we may obtain the integral equation

$$l_B^{(m+1)/(m)} \int_{T_B^0}^{T_B} f(\theta)^{1/m} d\theta = l_A^{(m+1)/(m)} \int_{T_A^0}^{T_A} f(\theta)^{1/m} d\theta\,, \tag{5.5}$$

remains bounded. *Localization* in the sense of Molinari and Clifton occurs if and only if $f(\theta)^{1/m}$ is integrable as $\theta \to \infty$. If $f(\theta) = \theta^\nu$, then

$$m + \nu < 0\,,$$

implies localization. We remark that localization of temperature implies localization of strain since

$$\lim_{\theta_A/\theta_B} (\frac{\dot{\gamma}_A}{\dot{\gamma}_B}) \to \infty \, .$$

Combined pressure and shear

We now show that the preceding analysis can be extended to the mixed case of pressure and shear. We now work directly with $p = -\operatorname{tr}(\sigma)/3$ instead of p_y. We assume that everywhere in the body is yielding and hence is on the yield surface

$$\frac{q^2}{q_c^2} + \left(\frac{2p - p_c - p_t}{p_c - p_t} \right)^2 = 1 \, .$$

This constraint is satisfied for some angle θ

$$\frac{q^2}{q_c^2} = \sin^2(\theta) \, , \tag{5.6}$$

and

$$\left(\frac{2p - p_c - p_t}{p_c - p_t} \right)^2 = \cos^2(\theta) \, . \tag{5.7}$$

In the simplest case, the stress field is uniform and is of the form

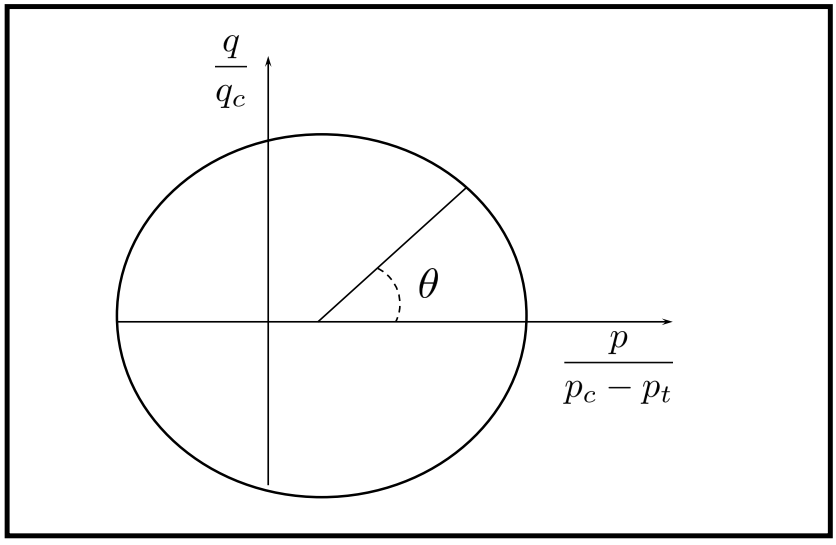

Figure 5.5: Illustration of Cam-Clay phase angle, θ.

$$\sigma = \begin{bmatrix} p & \tau & 0 \\ \tau & p & 0 \\ 0 & 0 & p \end{bmatrix} ,$$

Thus for any two points A, B we have the relations

$$\tau_A l^A = \tau_B l^B ,$$

and

$$p_A = p_B .$$

Inserting equations (5.6) and (5.7), we obtain

$$l_A q_{cA} \sin(\theta_A) = l_B q_{cB} \sin(\theta_B) , \tag{5.8}$$

and

$$l_A(p_{cA} + p_t + (p_{cA} - p_t)\cos(\theta_A)) = l_B(p_{cB} + p_t + (p_{cB} - p_t)\cos(\theta_B)) . \tag{5.9}$$

Using again the constitutive model

$$q_c = q_c^0(p_m(J^p))f(T)g(\dot{\gamma}^p) ,$$

conservation of energy (5.4), and equation (5.8) results in

$$l_B^{(m+1)/(m)} \int_{T_B^0}^{T_B} (f(T)\sin(\theta_B))^{1/m} dT = l_A^{(m+1)/(m)} \int_{T_A^0}^{T_A} (f(T)\sin(\theta_A))^{1/m} dT . \tag{5.10}$$

For localization there must exist some point B such that $T_B \to \infty$ and the quantity

$$l_B^{(m+1)/(m)} \int_{T_B^0}^{\infty} (f(T)\sin(\theta_B))^{1/m} dT ,$$

remains bounded. Assuming $\lim_{T\to\infty} f(T) \approx (T^\nu)$, we compute the following estimate

$$\begin{aligned} &\int_{T_B^0}^{\infty} |(f(T)\sin(\theta_B))^{1/m}| dT \le \int_{T_B^0}^{\infty} |(f(T))^{1/m}|(\sin(\theta_B))^{1/m} dT \\ &\le \int_{T_B^0}^{\infty} |(f(T))^{1/m}| dT < \infty . \end{aligned} \tag{5.11}$$

Equation (5.11) holds only if

$$m + \nu < 0 .$$

This constitutes a condition for the formation of shear bands. In our case, this is clearly satisfied (c.f. table 5.2). Thus, it becomes optimal for the solid to adopt constant and elastic deformations almost everywhere and accommodate deformation via localization in small regions. Precisely how small these regions are is dictated by the thermal conductivity. A common historical approach is made by returning to equation (5.3). We non-dimensionalize, with $\phi = T/T_0$

$$\dot{\phi} = \frac{\beta\tau\bar{t}}{Rc_v T_0}\dot{\gamma}^p + \frac{\kappa\bar{t}}{Rc_v h^2}\Delta\phi\,, \tag{5.12}$$

where we have introduced a characteristic lengthscale h and timescale $\bar{t}$ to non-dimensionalize the position and time respectively.

$$\tau = \text{constant}\,,$$

satisfies equilibrium. Let

$$\varepsilon = \frac{\kappa\bar{t}}{Rc_v h^2}$$

and

$$a = \frac{\beta\tau\bar{t}}{Rc_v}\,,$$

thus recovering

$$\dot{\phi} = a\dot{\epsilon}^p + \varepsilon\Delta\phi\,.$$

The preceding section considered the case where $\varepsilon \downarrow 0$. We now consider the opposite case when the Laplacian term is dominant. Appealing to standard regularity theory of elliptic PDE (c.f. for instance Evans [22]) in finite time $\dot{\phi} \downarrow 0$. Thus, we obtain the equation

$$\varepsilon\Delta\phi = -a\dot{\epsilon}^p(\phi)\,,$$

which in 1D, denoting by y the single variable, reduces to

$$\varepsilon\frac{\partial^2}{\partial y^2}\phi = -a\dot{\epsilon}^p(\phi)\,,$$

which, under mild assumptions, admits a solution

$$\phi = \phi(y, C_1, C_2)\,, \tag{5.13}$$

where C_1, C_2 are constants of integration. Solutions for simple problems may be found by asymptotic matching. In this problem, the boundary region is

$$\delta = \sqrt{\varepsilon}\,.$$

This approach works extremely well for certain special models of shear strength where the explicit determination of the temperature and velocity field can be determined from (5.13). However, for general models, the determination of (5.13) may become tedious. We will elect to, instead, make use of available variational structure to furnish approximations.

5.3 Local form expressions for conservation laws and rate form of variational update

We utilize conservation of mass

$$\dot{R} = 0\,, \tag{5.14}$$

conservation of momentum

$$R\dot{V} = \mathrm{Div}\boldsymbol{P} + RB\,, \tag{5.15}$$

conservation of angular momentum

$$\boldsymbol{P}\boldsymbol{F}^T = \boldsymbol{F}\boldsymbol{P}^T\,, \tag{5.16}$$

conservation of energy (in entropy form)

$$T\dot{N} = \boldsymbol{Y}\cdot\boldsymbol{F}^p + RQ - \mathrm{Div}H\,, \tag{5.17}$$

where Q denotes the heat generation and H denotes heat conduction. We also recall the equilibrium relation

$$N = -\frac{\partial W}{\partial T}\,. \tag{5.18}$$

We define the specific heat

$$RC := -T\frac{\partial^2 W}{\partial T^2}(\boldsymbol{F},\boldsymbol{F}^p,T) = \frac{\partial U}{\partial T}(N(T))\,, \tag{5.19}$$

For a given free energy $W(\boldsymbol{C},T,\boldsymbol{F}^p)$,

$$U(\boldsymbol{C},N,\boldsymbol{F}^p) = \sup_{\Theta}\left(W(\boldsymbol{C},\Theta,\boldsymbol{F}^p) + \Theta N\right), \tag{5.20}$$

defines the internal energy. Differentiating with respect to time, we obtain the identity

$$\dot{U} = \dot{W} + \dot{T}N + \dot{N}T\,. \tag{5.21}$$

Dissipative and diffusive processes

Let $\Delta(\dot{Z}, G)$ denote the general dissipation potential and assume a separable additive potential

$$\Delta(\dot{Z}, G) = \Psi^*(\dot{Z}) - \chi(G)\,, \tag{5.22}$$

where $G = -\boldsymbol{\nabla} T/T$. We close the internal variable equations with the following kinetic laws

$$\boldsymbol{Y} = \frac{\partial \Delta}{\partial \dot{Z}}\,, \tag{5.23}$$

$$H = \partial_G \Delta\,. \tag{5.24}$$

Differentiating (5.18) we obtain the identity

$$T\dot{N} = RC\dot{T} - T\frac{\partial \boldsymbol{P}}{\partial T} \cdot \dot{\boldsymbol{F}} + T\frac{\partial \boldsymbol{Y}}{\partial T} \cdot \dot{Z}\,. \tag{5.25}$$

We may relate $\dot{T}$ to $\boldsymbol{l}$ using conservation of energy. From equation (5.17), (5.19), and (5.25), we obtain

$$RC\dot{T} = T\frac{\partial \boldsymbol{P}}{\partial T}\dot{\boldsymbol{F}} - T\frac{\partial \boldsymbol{Y}}{\partial T}\dot{Z} + \boldsymbol{Y} \cdot \dot{Z} + RQ - \mathrm{Div} H\,, \tag{5.26}$$

whereupon assuming there are no heat sources setting $Q = 0$ we obtain

$$RC\dot{T} = T\frac{\partial \boldsymbol{P}}{\partial T}\boldsymbol{l}\boldsymbol{F} + (-T\frac{\partial \boldsymbol{Y}}{\partial T} + \boldsymbol{Y}) \cdot \dot{Z} - \mathrm{Div} H\,. \tag{5.27}$$

Assuming standard Newtonian heat conduction

$$H = -\partial_G \Delta = -\kappa \boldsymbol{\nabla} T\,,$$

we obtain

$$RC\dot{T} = T\frac{\partial \boldsymbol{P}}{\partial T}\boldsymbol{l}\boldsymbol{F} + (-T\frac{\partial \boldsymbol{Y}}{\partial T} + \boldsymbol{Y}) \cdot (J^p \boldsymbol{F}^{-1} \boldsymbol{l}^p \boldsymbol{F}) + \kappa \Delta T\,. \tag{5.28}$$

The adiabatic limit is obtained by taking the limit $\kappa \downarrow 0$.

Variational constitutive update in rate form

We define the rate potential function following [87, 104]

$$\begin{aligned} f(\dot{\varphi}, T, \dot{N}, \dot{Z}) = &\int_\Omega \big(\dot{U} - T\dot{N} + \Delta(\frac{T}{\Theta}\dot{Z}, -\frac{1}{T}\boldsymbol{\nabla} T)\big) dV - \int_\Omega RB \cdot \dot{\varphi} dV \\ &- \int_{\partial\Omega_2} \bar{T} \cdot \dot{\varphi} dS + \int_\Omega RQ \log(T/T_0) dV - \int_{\partial\Omega} \bar{H} \cdot n \log(T/T_0) dS\,. \end{aligned} \tag{5.29}$$

Taking variations with respect to $\dot{\varphi}, T, \dot{N}$ recovers the above equations. Thus, equation (5.29) constitutes a variational principle for the energetic and kinetic equations of mechanics. In the remainder of this paper, we let $Z = \{\boldsymbol{F}^p\}$ comprise the internal variable list. The dissipation potential $\Psi^*(\dot{\boldsymbol{F}}^p)$ is related to the dissipation potential per unit deformed volume $\psi^*(\boldsymbol{l}^p)$ by

$$\Psi^*(\dot{\boldsymbol{F}}^p) = J\psi^*(\boldsymbol{F}^e\dot{\boldsymbol{F}}^p\boldsymbol{F}^{p^{-1}}\boldsymbol{F}^{e^{-1}}) \,, \tag{5.30}$$

where $\boldsymbol{l}^p = \boldsymbol{F}^e\dot{\boldsymbol{F}}^p\boldsymbol{F}^{p^{-1}}\boldsymbol{F}^{e^{-1}}$.

Steady state shear band

An interesting step in the analysis of shear localization is the examination of steady state processes. We can easily examine these directly via the above variational principle (5.29). We assume $B = 0$ and $Q = 0$. At steady state, $\dot{T} = 0$ and $\dot{W} = 0$, which using equation (5.21) implies $\dot{U} - T\dot{N} = 0$. Thus, the variational principle reduces to the determination of the stationary points of the functional

$$f(T, \dot{Z}) = \int_\Omega (\Psi^*(\dot{Z}) - \chi(G))dV + \int_\Omega RQ\log(T/T_0)dV - \int_{\partial\Omega} \bar{H}\cdot n\log(T/T_0)dS \,, \tag{5.31}$$

where we distinguish f in this equation from (5.29) allowing the function to be defined both by its name and its arguments. We assume a quadratic conduction potential

$$\chi = \kappa T_0/2|G|^2 \,.$$

We make the ansatz on the temperature distribution

$$T(z, \hat{T}) := \bar{T}\exp(\log(\hat{T}/\bar{T})(1 - (2z/h)^2)) \,,$$

noting that $G = -\boldsymbol{\nabla}\log(T) = -\log(\hat{T}/\bar{T})(8z/h^2)$, and truncating the integrals in the above expression in the vicinity of a fully formed shear band, we obtain

$$\begin{aligned} f(T, \dot{Z}) &= \int_\Omega (\Psi^*(\dot{Z}) - \chi(G))dV \\ &= \frac{h}{2}\Psi(\dot{Z}\frac{\hat{T}}{\Theta}, \Theta) - \kappa T_0\frac{8}{3}\frac{1}{h}\log^2(\hat{T}/\bar{T}) \,. \end{aligned} \tag{5.32}$$

Taking variations with respect to both h and $\hat{T}$, we obtain

$$0 = \frac{1}{2}\Psi(\dot{Z}\frac{T}{\Theta}, \Theta) + \kappa T_0\frac{8}{3}\frac{1}{h^2}\log^2(\hat{T}/\bar{T}) \tag{5.33}$$

$$0 = \frac{h}{2}\Psi'(\dot{Z}\frac{T}{\Theta}, \Theta)\frac{\dot{Z}}{\Theta} - \kappa T_0\frac{8}{3}\frac{1}{h}\log(\hat{T}/\bar{T})\frac{1}{\hat{T}} \,. \tag{5.34}$$

We find in section 5.5 that the shear bands evolve to states given by these simple conditions over time.

5.4 Incremental problem with localization condition

Localization in finite deformations was put forth by Rice [71] and later by Borja [8] among others. Ortiz and Repetto [63] forged the connection between loss of convexity and formation of microstructure in plasticity. Carstensen et al. [10] elaborated on these insights and formalized these connections for incremental variational problems. Miehe and coworkers [38, 39, 58, 59] studied approximations to rank-one convexification of non-convex inelastic potentials with an a priori known micro length scale. Trinh and Hackl [94] conducted similar explorations a short time later. These incremental variational principle strategies are extended to include the effect of temperature in Yang, Stainier, and Ortiz [104]. Recent contributions towards studying shear localization in this setting have been made by Stainier and co-workers (see for instance [86, 88, 89]) as well as Yang et al. [103].

In this section, we utilize techniques due to these authors to develop conditions for localization in the variational setting, develop a multiscale one-tier lamination strategy that jointly determines an optimal shear band size, and further apply this strategy to the Cam-Clay model of silica glass. The algorithmic contribution of our present work is the introduction of a joint optimization of *both* the laminates and the sub-length-scale problem. We remark that this differs from the work of Miehe which assumes an a priori length-scale. In this section, we provide the illustration in Fig. 5.6 of the geometry of a shear band.

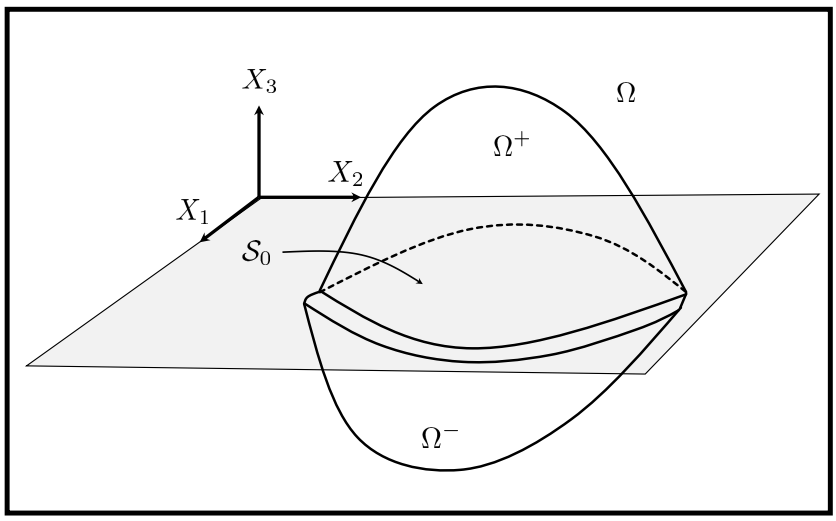

Figure 5.6: We illustrate a shear band in a solid body.

We begin by recalling the definition of rank-one convexity

Definition 5.4.1 *A function $\psi : \mathbb{R}^{d\times d} \to \mathbb{R}$ is called rank-one convex if for every $F \in \mathbb{R}^{d\times d}$ and every $n, m \in \mathbb{R}^d$, the map $t \mapsto \psi(F + tn \otimes m)$ is convex on $\mathbb{R}$.*

From equation (5.29) following [104], we can construct a reduced functional of the form

$$I(\dot{\varphi}) = \inf_{\dot{N}, \dot{\boldsymbol{F}}^p} \sup_{T} f(\dot{\varphi}, T, \dot{N}, \dot{\boldsymbol{F}}^p) \, . \tag{5.35}$$

We consider a time discretization of this function and compute its first variation

$$\delta I(\varphi_{n+1}, \eta) = \int_\Omega (\boldsymbol{\nabla}\eta : \boldsymbol{P}_{n+1} - R\eta \cdot B) dV - \int_{\partial\Omega_2} \eta \cdot \bar{t} dA \, ,$$

along some admissible function η and $\boldsymbol{P}_{n+1} = \dfrac{\partial \Phi_{n+1}}{\partial \boldsymbol{F}}(\boldsymbol{F}_{n+1})$ where Φ_{n+1} serves as incremental potential for the first Piola Kirchoff stress $\boldsymbol{P}_{n+1}$. Computing the 2nd variation

$$\delta^2 I = \int_\Omega \boldsymbol{\nabla}\eta : A(\varphi_{n+1}) : \delta \boldsymbol{F}_{n+1} dV - \int_{\partial\Omega_2} \eta \delta\bar{t} dA \, ,$$

where $\delta \boldsymbol{P}_{n+1} = A(\varphi_{n+1}) : \delta \boldsymbol{F}_{n+1}$ and $A(\varphi_{n+1}) = \dfrac{\partial \boldsymbol{P}_{n+1}}{\partial \boldsymbol{F}_{n+1}} = \dfrac{\partial^2 \Phi}{\partial \boldsymbol{F}^2_{n+1}}$.
Requiring $\delta^2 I = 0$ we obtain

$$\begin{aligned} &- \int_\Omega \eta \cdot \boldsymbol{\nabla} \cdot (A(\varphi_{n+1}) : \delta \boldsymbol{F}_{n+1}) dV - \int_{\partial\Omega_2} \eta(\delta\bar{t} - \delta \boldsymbol{P} \cdot \boldsymbol{N}) dA \\ &+ \int_{\mathcal{S}_0} [\![A(\varphi_{n+1}) : \delta \boldsymbol{F}_{n+1}]\!] \cdot \boldsymbol{N} dS = 0 \, , \end{aligned} \tag{5.36}$$

where the notation $[\![A]\!] := A^+ - A^-$ denotes the jump across the surface $\mathcal{S}_0$ where A^+, A^- are the values of a function A evaluated on either side of $\mathcal{S}^0$(see Fig. 5.6). Assuming equilibrium and that $\boldsymbol{\nabla} \cdot \delta \boldsymbol{P}_{n+1} = \delta \boldsymbol{\nabla} \cdot \boldsymbol{P}_{n+1}$, implies

$$[\![A(\varphi_{n+1}) : \delta \boldsymbol{F}_{n+1}]\!] \cdot \boldsymbol{N} = 0 \, , \tag{5.37}$$

on $\mathcal{S}_0$ and that the remaining Euler Lagrange conditions are satisfied trivially. In the simplest case, A is continuous across the band [71], and since $\delta \boldsymbol{F}$ is co-linear with $\dot{\boldsymbol{F}}$ we obtain

$$A(\varphi^{n+1}) : [\![\dot{\boldsymbol{F}}_{n+1}]\!] \cdot \boldsymbol{N} = 0 \, . \tag{5.38}$$

Then, since the deformation gradient rate has the representation

$$[\![\dot{\boldsymbol{F}}_{n+1}]\!] = [\![\dot{\varphi}_{n+1}]\!] \otimes \boldsymbol{N} \,,$$

where $[\![\dot{\varphi}_{n+1}]\!]$ is the jump in material velocity across $\mathcal{S}_0$, we obtain

$$(\boldsymbol{N}^T A(\varphi_{n+1}) \cdot \boldsymbol{N}) \cdot [\![\dot{\varphi}_{n+1}]\!] = 0 \,, \tag{5.39}$$

which, defining the shorthand $\tilde{A} = \boldsymbol{N}^T A \cdot \boldsymbol{N}$, holds if and only if

$$\det(\tilde{A}) = 0 \,.$$

This is equivalent to the previous statement of incremental rank-one convexity assuming sufficient differentiability of Φ. We remark that although the satisfaction of this condition is sufficient for the formation of microstructure it is certainly not necessary in general, i.e. it may be possible to find localized deformations that are not of this form for a general model. See [17] or [18] for the extensive theoretical foundations of necessity and sufficiency in variational problems.

Incremental potential

We now introduce a fully discretized incremental variational principle following [103, 104]. We remark that there are numerous consistent discretizations. One such scheme is

$$\begin{aligned} f_n[\varphi_{n+1}, T_{n+1}, N_{n+1}, Z_{n+1}] &= \int_\Omega \Phi_n[\varphi_{n+1}, T_{n+1}, N_{n+1}, Z_{n+1}] dV + \text{ boundary terms} \\ &= \int_\Omega [U_{n+1} - U_n] - \frac{T_n^2}{T_{n+1}}(N_{n+1} - N_n) + \Delta t \Delta_{n+1}\left(\frac{T_n}{T_{n+1}}\frac{Z_{n+1} - Z_n}{\Delta t}; -\frac{\boldsymbol{\nabla} T_n}{T_n}\right) \\ &- \int RB_{n+1} \cdot (\varphi_{n+1} - \varphi_n) dV - \int_{\partial_T \Omega} \bar{T}_{n+1} \cdot (\varphi_{n+1} - \varphi_n) dS \\ &+ \int \Delta t R Q_{n+1} \log(T_{n+1}/T_n) dV - \int \Delta t \bar{H}_{n+1} \log(T_{n+1}/T_n) dS \,. \end{aligned} \tag{5.40}$$

The Euler-Lagrange equations consistent with conservation of energy and the kinetic equation along with a discretized version of equation (5.25) with conduction neglected are

$$\begin{aligned} RC(T_{n+1} - T_n) = \boldsymbol{Y}_{n+1} \cdot (Z_{n+1} - Z_n) \\ - T_{n+1} \partial_T \boldsymbol{Y}_{n+1} (Z_{n+1} - Z_n) \,, \end{aligned} \tag{5.41}$$

and

$$-\boldsymbol{Y}_{n+1} + \partial_{\dot{Z}} \Delta_{n+1}\left(\frac{T_n}{T_{n+1}}\left(\frac{Z_{n+1} - Z_n}{\Delta t}\right)\right) = 0 \,. \tag{5.42}$$

In principle, we can solve T_{n+1}, Z_{n+1} as a function of $\boldsymbol{F}_{n+1}$ (where we are assuming the adiabatic limit). Inserting these into f_n recovers I_n. This is challenging to enforce explicitly for general deformations. However, at the present we restrict our attention to rank-one deformations and make approximations introduced in the following sections.

Material parameters

Some material constants for silica are provided in table 5.1.

Table 5.1: Heat capacity, density, and conduction coefficient of silica

c_v	R	κ
703 J/(Kg K)	2200 Kg/m^3	1.4 W/(m K)

Following [80], we adopt a specific model where the temperature and thermal dependence of the yield stress are described by power laws $\xi(T) = (T/T_0)^\nu$ and $w(\dot{\gamma}^p) = 1 + \gamma_0(\dot{\gamma}^p)^m$. The scaling exponents are presented in table 5.2. These

Table 5.2: Thermal and shear rate critical state line exponents

ν	m	γ_0
-0.70	0.462	0.0000141

exponents characterize the competition between thermal softening and strain rate hardening.

Shear banding at critical state

The second term in (5.41) are of higher order and we assume they are negligible. From work conjugacy and equation (5.30), we obtain the condition

$$Rc_v(T_{n+1} - T_n) = \boldsymbol{Y}_{n+1} \cdot (\boldsymbol{F}^p_{n+1} - \boldsymbol{F}^p_{n+1}) = J\boldsymbol{y}_{n+1} \cdot (\Delta\varepsilon^p \boldsymbol{M}) + O(\Delta t)\,,$$

recalling that in particular the flow rule is of the form $\boldsymbol{l}^p = \dot{\varepsilon}^p \boldsymbol{M}$. We recall we have made the constitutive assumption

$$\sigma_y = q_c^0(p_m(J^p))\xi(T)w(\boldsymbol{l}^p)\,,$$

namely that the dual kinetic potential is homogeneous function of degree one with the flow direction determined by normality to the yield surface. We have also assumed

a constant heat capacity $C = c_v$. We further restrict the rank-one deformation corresponding to pure shear. Accordingly, we assume

$$\boldsymbol{M} = \begin{bmatrix} 0 & 1 & 0 \\ 1 & 0 & 0 \\ 0 & 0 & 0 \end{bmatrix} ,$$

Thus, at critical state, the dissipation per unit deformed volume is

$$\psi^*(\boldsymbol{l}^p) = q_c^0(p_m(J^p))\xi(T)\left(|\dot{\gamma}^p| + \frac{\gamma_0}{m+1}|\dot{\gamma}^p|^{m+1}\right) .$$

We now consider the reduction of the problem to simple shear composed with a dialation which we assume to be independent of time:

$$\boldsymbol{F} = J \begin{bmatrix} 1 & \gamma^e & 0 \\ 0 & 1 & 0 \\ 0 & 0 & 1 \end{bmatrix} \begin{bmatrix} 1 & \gamma^p & 0 \\ 0 & 1 & 0 \\ 0 & 0 & 1 \end{bmatrix} = J \begin{bmatrix} 1 & \gamma^e + \gamma^p & 0 \\ 0 & 1 & 0 \\ 0 & 0 & 1 \end{bmatrix} .$$

Then

$$\dot{\boldsymbol{F}} = J \begin{bmatrix} 0 & \dot{\gamma}^e + \dot{\gamma}^p & 0 \\ 0 & 0 & 0 \\ 0 & 0 & 0 \end{bmatrix} ,$$

and

$$\dot{\boldsymbol{F}} = \boldsymbol{l}\boldsymbol{F} .$$

We consider the energy

$$W^e = \frac{\mu(T)}{2}((J^e)^{-2/3}\,\mathrm{tr}(\boldsymbol{C}^e) - 3) + f(J^e, T) ,$$

and assume that the temperature dependence of the elasticity is much smaller than the temperature dependence of the inelastic processes (which is borne out in the molecular dynamics data). Moreover, for simple shear at fixed J^e, $f(J_e)$ is a constant. Thus, by direct evaluation with $\boldsymbol{C}^e = \boldsymbol{F}^{eT}\boldsymbol{F}^e$, up to constants

$$W^e = \frac{\mu}{2}(\gamma^e)^2 + f(J^e) ,$$

where $\gamma^e = \gamma - \gamma^p$ Thus we may write the incremental elastic energy simply

$$W^e_{n+1}(\gamma^e_{n+1}) = \frac{\mu}{2}\gamma^{e2} + f(J^e) .$$

Thus the problem is reduced to solving the following two equations

$$c_v(T_{n+1} - T_n) = Jq_c^0(p)\xi(T_{n+1})w(\gamma^p)\Delta\gamma^p ,$$

$$\mu(\gamma_{n+1} - \gamma^p_{n+1}) = q^0_c \xi(T) w(\Delta\gamma^p)\,,$$

for γ^p_{n+1} and T_{n+1} for each fixed $\gamma_{n+1}$and evaluating the incremental potential

$$\Phi_{n+1} = W_{n+1}(\gamma^e_{n+1}) + \Delta t \psi^*(\gamma^p_{n+1}, T_{n+1})\,,$$

at each γ_{n+1}. We perform this algorithm and plot the results in Fig. 5.7.

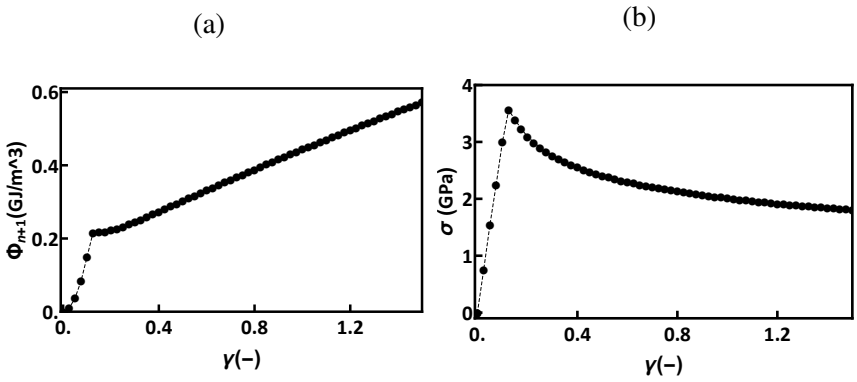

Figure 5.7: The incremental potential and stress plotted along a rank-one line at $p = 0.1$ GPa.

It is immediately evident that the potential is *not* convex along this rank-one line and in fact remains concave for the entire (inelastic) domain computed. Thus we may appeal to standard theory from the calculus of variations (c.f. for instance [16] and [18]) to recognize that this potential is prone towards minimizing sequences that do not converge. To wit, we illustrate this problem in Fig. 5.8.

Given a deformation in the non-convex region of the potential, we may evidently lower the value of the incremental potential by mixing by volume fractions a point near the elastic energy minima and a point with very large deformation γ. Mathematically, the lack of growth observed in Fig. 5.7 as the strain tends to infinity results in a lack of coercivity. It then becomes optimal to have infinitely large shears in infinitely small regions. Practically, for the purposes of numerical computation, this can lead to a well known problem of mesh-dependence of solutions. We will see, however, that the proper accounting of lower-scale physical processes alleviates this issue.

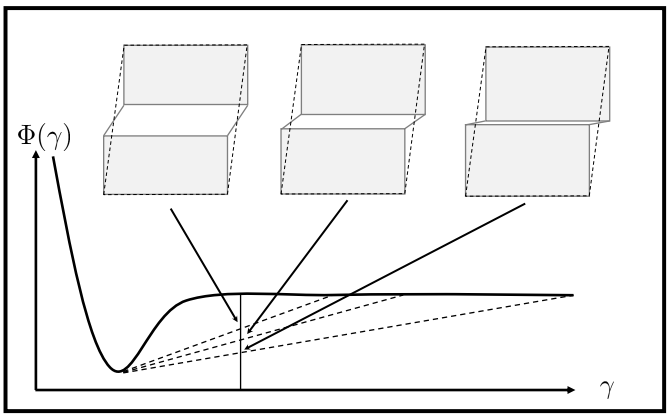

Figure 5.8: We provide an illustration of the consequences of loss of coercivity. It is optimal for the solid to adopt infinitesimally fine shearing regions.

5.5 local conditions limit lamination

We begin by formulating the strain localization condition following Yang et. al. [103]. We recall that $\varphi : \Omega \times (0,T) \to \mathbb{R}^3$ where $(0,T)$ denotes the time interval. Let $S_0 \subset \Omega$ denote a surface contained in the body as well as the thin region containing it with thickness h. Denote by Ω^+, Ω^- each side of the surface.

We assume now that we are examining a lengthscale, h, where heat conduction plays a strong role. Thus we assume that conduction derives from a Fouier potential

$$H = \frac{\partial \chi}{\partial G} ,$$

with

$$G = -\frac{\boldsymbol{\nabla} T}{T} .$$

We assume that the plastic flow is of the form $\boldsymbol{l}^p = \varepsilon^p \boldsymbol{M}$ where $\boldsymbol{M}$ is in the normal cone of the safe set (5.1). We define the shear band incremental functional, which is consistent with the rate functional (5.29),

$$\begin{aligned} f_n(\varphi_{n+1}, T_{n+1}, \varepsilon^p_{n+1}, \boldsymbol{M}) = \int_{-h_{n+1}/2}^{h_{n+1}/2} \Big(& U(\boldsymbol{F}_{n+1} \boldsymbol{F}^p_{n+1}{}^{-1}, N_{n+1}, J^p) \\ & - U_n - \frac{T_n^2}{T_{n+1}}(N_{n+1} - N_n) + \Delta t \psi^*\Big(\frac{T_n}{T_{n+1}} \frac{\varepsilon^p_{n+1}}{\Delta t}\Big) + \Delta t \chi(G_{n+1})\Big) dz , \end{aligned} \tag{5.43}$$

and refer to Fig. 5.6 for illustration. We assume that the temperature profile across the band is Gaussian

$$T(z, T_{n+1}) := \bar{T}_{n+1} \exp\Big(\log\Big(\frac{T_{n+1}}{\bar{T}_{n+1}}\Big)\Big(1 - \Big(\frac{2z}{h_{n+1}}\Big)^2\Big)\Big) , \tag{5.44}$$

where T_{n+1} is the temperature at the center of the band and $\bar{T}_n$ is the temperature at the boundary. This constitutes a low dimensional Galerkin approach to shear banding, enabled by the variational structure (5.35). We remark that there are many possible ansätze. However, this selection is extremely simple due to it's low dimensionality and its behavior is consistent with that of more sophisticated trial functions put forth in, for instance, [89].

Assuming a conduction law quadratic in G, $\chi = \kappa T_0/2|G|^2$, we may explicitly evaluate χ

$$\chi(G_{n+1}) = \frac{\kappa T_0}{2}|\frac{8}{h_{n+1}^2} z \log(\frac{T_{n+1}}{\bar{T}_{n+1}})|^2 ,$$

whereupon integrating we obtain the conduction contribution explicitly to the incremental variational principle

$$\Delta t \int_{-h_{n+1}/2}^{h_{n+1}/2} \chi dz = \kappa T_0 \frac{8}{3} \log^2(T_{n+1}/\bar{T}_{n+1})\Delta t/h_{n+1} .$$

Then the incremental principle for the shear band becomes

$$\begin{aligned} f_n(\varphi_{n+1}, T_{n+1}, \varepsilon^p_{n+1}, \boldsymbol{M}) = \int_{-h_{n+1}/2}^{h_{n+1}/2} \big(& U(\boldsymbol{F}_{n+1}\boldsymbol{F}^p_{n+1}{}^{-1}, N_{n+1}, J^p) - U_n \\ & - \frac{T_n^2}{T_{n+1}}(N_{n+1} - N_n) + \Delta t \psi^*(\frac{T_n}{T_{n+1}}\frac{\varepsilon^p_{n+1}}{\Delta t})\big) dz \\ & + \kappa T_0 \frac{8}{3} \log^2(T_{n+1}/\bar{T}_{n+1})\Delta t/h_{n+1} . \end{aligned} \tag{5.45}$$

Taking variations we may obtain the following Euler-Lagrange equations, and utilizing the simplified kinematics of the previous section

$$\mu(\gamma_{n+1} - \gamma^p_{n+1}) = \frac{T_n}{T_{n+1}} q_{c0}(p_m)\xi(T_{n+1}) w(\dot{\gamma}^p) , \tag{5.46}$$

$$\begin{aligned} & h_{n+1}^2 \frac{T_n^2}{T_{n+1}}(T_{n+1} - T_n) R c_v \\ & - h_{n+1}^2 q_{c0}(p_m)\xi(T_{n+1}) w(\frac{\gamma^p_{n+1} - \gamma^p_n}{\Delta t}\frac{T_n}{T_{n+1}}) T_n(\gamma^p_{n+1} - \gamma^p_n) \\ & + \frac{16}{3}(\Delta t k T_0) T_{n+1} \log(T_{n+1}/\bar{T}_{n+1}) = 0 , \end{aligned} \tag{5.47}$$

and

$$\begin{aligned} & \frac{1}{2}\mu(\gamma_{n+1} - \gamma^p_{n+1})^2 - \frac{1}{2}\mu(\gamma_n - \gamma^p_n)^2 \\ & - \frac{T_n^2}{T_{n+1}^2} R c_v (T_{n+1} - T_n) + \Delta t \psi^*\big(\frac{T_n}{T_{n+1}}\frac{\gamma^p_{n+1} - \gamma^p_n}{\Delta t}\big) \\ & - \Delta t \frac{8 k T_0}{3 h_{n+1}} \log^2(\frac{T_{n+1}}{\bar{T}_{n+1}}) = 0 . \end{aligned} \tag{5.48}$$

Computing T_{n+1} and γ^p_{n+1} from the Euler-Lagrange equations of this function, assuming the same kinematics as the preceding section, we obtain an incremental variational potential for the evolution of the shear band.

Approximate rank-one convexification

Define $\Omega^A, \Omega^B \subset \Omega$ and consider a macroscopically defined average shear strain rate $\dot{\bar{\gamma}}$. We introduce the following rank one convexification, computing the convex envelope following definition 5.4.1 restricted to two point combinations:

$$\inf_{\Omega^A,\Omega^B,\varphi^A_{n+1},\varphi^B_{n+1}} \int_{\Omega^A} \Phi(\varphi^A_{n+1})dX + \int_{\Omega^B} \Phi(\varphi^B_{n+1})dX \,, \tag{5.49}$$

subject to $\Omega^A \cap \Omega^B = \emptyset$ and $\Omega^A \cup \Omega^B = \Omega$. We assume that the lamination only occurs in shear along the direction of maximum shear. This formula reduces to

$$\inf_{\lambda,\gamma^A,\gamma^B} \lambda\Phi(\gamma^A_{n+1}) + (1-\lambda)\Phi(\gamma^B_{n+1}) \,, \tag{5.50}$$

subject to $\lambda\dot{\gamma}^A + (1-\lambda)\dot{\gamma}^B = \dot{\bar{\gamma}}$ where $\bar{\gamma}$ is a macroscopically specified shear rate and $\lambda \in [0,1]$. Discretizing and eliminating the constraint we obtain

$$\inf_{\lambda,\Delta\gamma^A} \lambda\Phi(\Delta\gamma^A) + (1-\lambda)\Phi(\frac{\Delta\bar{\gamma} - \lambda\Delta\gamma^A}{1-\lambda}) \,. \tag{5.51}$$

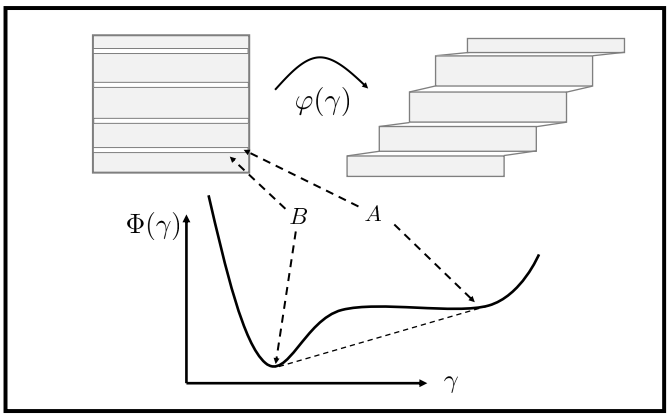

Figure 5.9: We provide a graphical illustration of incremental potential minimization sequence mixing two phases labeled A and B. This is known in the classical thermodynamics literature as the Gibb's tangent which is related to the Maxwell line.

The incremental shear strain $\Delta\gamma := \gamma_{n+1} - \gamma_n$ is the total shear increment across one of the domains. In this problem, we will define $\Delta\gamma^A$ to be the incremental shear

in the shear band. Similarly, λ is the volume fraction of shear bands within the material. Taking variations with respect to λ and γ^A we obtain

$$\Phi(\gamma^A) - \Phi(\frac{\Delta\bar{\gamma} - \lambda\Delta\gamma^A}{1-\lambda}) + (1-\lambda)\frac{\partial\Phi}{\partial\Delta\gamma}\frac{1}{(1-\lambda)^2}\left(\Delta\bar{\gamma} - \Delta\gamma^A\right) = 0\,, \tag{5.52}$$

and

$$\frac{\partial\Phi}{\partial\Delta\gamma}(\Delta\gamma^A) - \frac{\partial\Phi}{\partial\Delta\gamma}(\frac{\Delta\bar{\gamma} - \lambda\Delta\gamma^A}{1-\lambda}) = 0\,. \tag{5.53}$$

For the current model under consideration, these equations reduce to

$$\Delta t\psi^*(\frac{\Delta\gamma^p}{\Delta t}) + \frac{\left(\Delta\bar{\gamma} - \Delta\gamma^A\right)}{(1-\lambda)}\frac{\partial\Phi}{\partial\Delta\gamma} = 0\,, \tag{5.54}$$

and

$$\gamma^{A^e} = \gamma^{B^e}\,. \tag{5.55}$$

Hereafter, we write $\gamma = \gamma^A$ for simplicity. These imply

$$\lambda = \frac{\Delta\bar{\gamma} - \Delta\gamma^e}{\Delta\gamma^p}\,. \tag{5.56}$$

Inserting into (5.50), we obtain

$$\begin{aligned}
&\inf_{\lambda,\Delta\gamma} \lambda\Phi(\Delta\gamma_1) + (1-\lambda)\Phi(\frac{\Delta\bar{\gamma} - \lambda\Delta\gamma}{1-\lambda}) \\
&= \inf_{\Delta\gamma,\Delta\gamma^p,T,\lambda} W(\gamma^e) + \lambda\Delta t\psi^*(\frac{\Delta\gamma^p}{\Delta t})\,, \\
&= \inf_{\Delta\gamma,\Delta\gamma^p,T} W(\gamma^e) + \frac{\Delta\bar{\gamma} - \Delta\gamma^e}{\Delta\gamma^p}\Delta t\psi^*(\frac{\Delta\gamma^p}{\Delta t}) \\
&= \inf_{\Delta\gamma} W(\gamma^e) + \frac{\Delta\bar{\gamma} - \Delta\tilde{\gamma}^e}{\Delta\tilde{\gamma}^p}\Delta t\psi^*(\frac{\Delta\tilde{\gamma}^p}{\Delta t}, \tilde{T})\,,
\end{aligned} \tag{5.57}$$

where $\tilde{T}, \tilde{\gamma}^p$ are optimal for fixed γ. We determine $\tilde{T}, \tilde{\gamma}^p$ by minimizing (5.45).

As is expected for the model under present study in shear, the growth of the incremental potential is barely super-linear – this is consistent with a plasticity model for which the kinetic potential exhibits mild strain rate hardening. Nonetheless, such growth is sufficient to recover coercivity of the model (see, for instance, [17]). Thus, the glass will minimize its incremental deformation power by mixing small regions – on of order $1 \sim 40\mu m$ as we will see in the next section – with large regions undergoing small, elastic deformations.

Shear banding at critical state

We now study the behavior of the shear band evolution at critical state. We first directly compute formula (5.57) for a particular strain increment to exhibit the minimization problem for the incremental shear in the band γ_{n+1}, see Fig. 5.10. Evidently, there is a well defined minimum. We should emphasize that γ_{n+1} is distinct from the macroscopic shear $\bar{\gamma}$. By the previous analysis, the incremental energy as a function of $\bar{\gamma}$ is strongly non-convex.

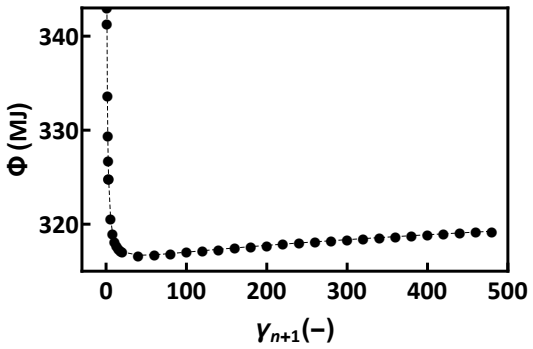

Figure 5.10: Computed incremental potential has a well defined minimum for γ_{n+1}.

In Fig. 5.11, we examine the evolution of the shear band in time. The shear band appears to evolve more quickly towards a steady state at higher pressure. At steady state, the shear stress is minimized for instance at a pressure of 5 GPa and the corresponding shear band thickness is maximized. The non-monotonic dependence on the pressure at steady state arises from the anomalous critical state line. The

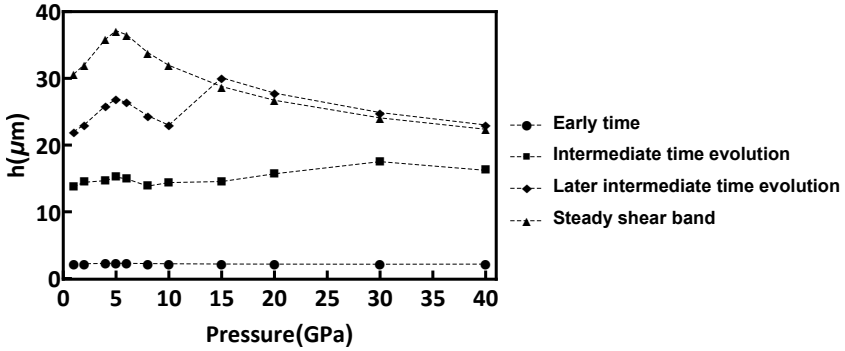

Figure 5.11: We plot the shear band thickness versus pressure at various stages of evolution of the shear band.

temperature rises to a steady state as the shear strain increases and the stress exhibits

a corresponding decrease as a function of time (see Fig. 5.12). The localized plastic shear is large (see Fig. 5.12) which is consistent with classical descriptions of shear localization and observations of experiment, see [20] for a multitude of examples.

(a)

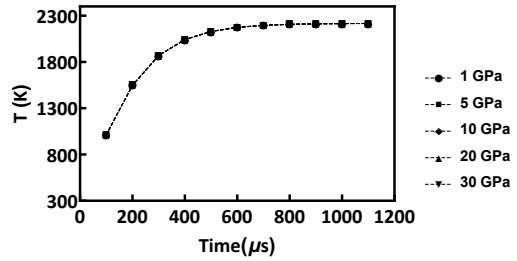

(b)

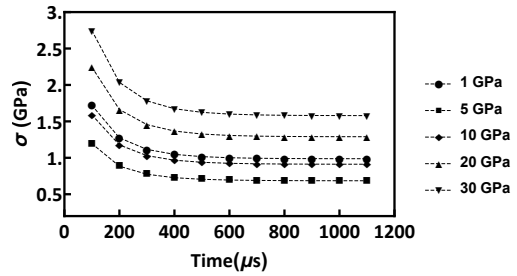

(c)

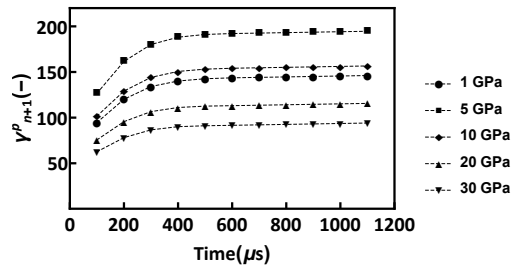

Figure 5.12: We examine the behavior of the shear band evolution over time plotting (a) Temperature (K) as a function of time (b) Stress (GPa) as a function of time (c) Plastic incremental strain.

In Fig. 5.12, the stress decreases as a function of time and is also a function of pressure. The decrease in stress however is stable due to the shear band evolution as dictated by the competition between energetics and kinetics of the glass.

In Fig. 5.13 (a), the shear band thickness is plotted versus time. The shear band thickness increases over time from around 2 μm to nearly 40 μm. This is consistent

(a)

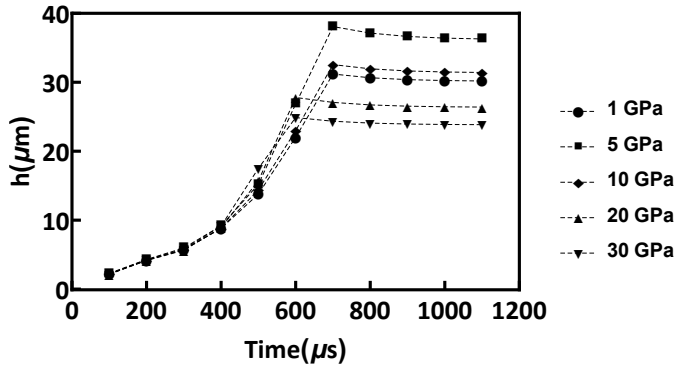

(b)

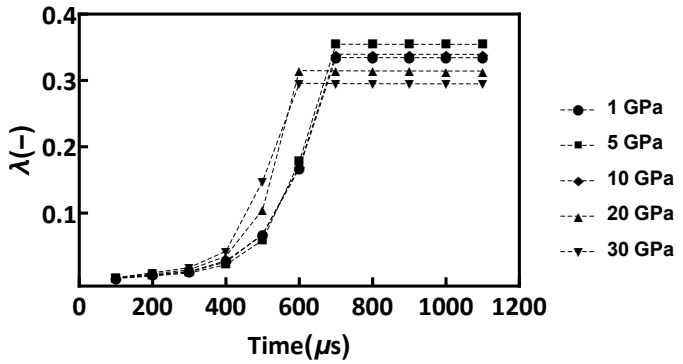

(c)

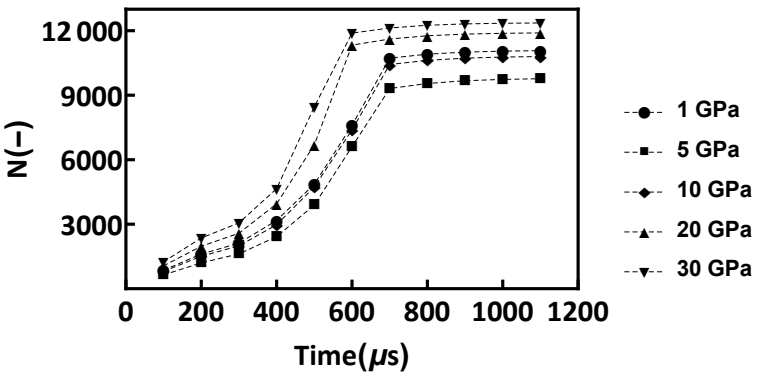

Figure 5.13: We examine the behavior of the shear band evolution over time plotting (a) Shear band thickness in *mm* as a function of time (b) the volume fraction of shear banded material as a function of time and (c) The approximate number of shear bands in a $1m$ thick sample. The last is of course carrying the same information from the previous two plots.

with size of shear bands observed in many experimental studies of shear banding in

a variety of materials [20]. We also evaluate the volume fraction (or equivalently the number of shear bands in a fixed sample size) and display these results in Fig. 5.13 (a) and (b). The volume fraction increases substantially during the deformation.

We remark we assume that each update of the internal variable depends on the internal variable from the previous step (i.e. the prediction of the current temperature depends on the previous temperature).

Shear banding at non-critical state and comparison to plate impact experiments

We now examine the behavior of the Cam-Clay model when it is not at critical state. We recall (see [78]) that the initial consolidation of silica glass occurs with mild increase in consolidation pressure p_c. Thus, as a first approximation, we take p_c to be constant in the following analysis. Though a simplifying approximation, this assumption yields significant insight into the physical behaviors observed in silica glass during flyer plate impact experiments. Specifically, the combination of lack of hardening in the consolidation curve, anomalous critical state line, and thermal softening drives the drops in stress observed in flyer plate impact experiments.

We study the deformation at a particular pressure, p, and a particular macroscopic shear strain increment $\Delta\bar{\gamma}$. Since p and p_c are constant in our calculation, then the ratio $\chi \equiv q/q_c$ is constant by (5.1). Thus, the shear and pressure components decouple which enables the utilization of the simple computational strategy from the previous section with a yield stress of χq_c where χ has been set a priori. We select $\chi = 0.2$, $p_m = 3$ GPa which is consistent with a state which has just been loaded to a maximum pressure of 3.5 GPa as was done in the flyer plate impact experiments by Sundaram and Clifton [90]. We illustrate such a point in stress space relative to the Cam Clay elastic domain in Fig. 5.14.

We display the stress, temperature, and shear band size history versus time in Fig. 5.16, 5.17, and 5.18 respectively. In Fig. 5.16, we compare the stress history to that provided by Sundaram and Clifton [90]. Their results exhibit the entire loading history including an elastic ramp loading region and a brief flow plateau. We shift their data set to the onset of decrease in shear to make a comparison to our data. As we are modeling a shear localization process this is the most appropriate basis for comparison. The shear stress decreases as a function of time.

In Fig. 5.17, we observe that the width of the shear bands increase in time. Additionally, the shear bands are rather small (sub-μm). To be consistent with the experiments of Sundaram and Clifton, the calculation was performed at a higher

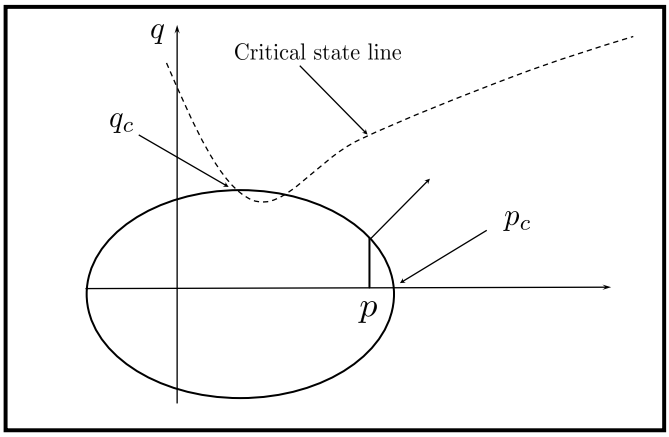

Figure 5.14: Illustration of the Cam-Clay elastic domain and critical state line. Normality gives the direction of plastic flow.

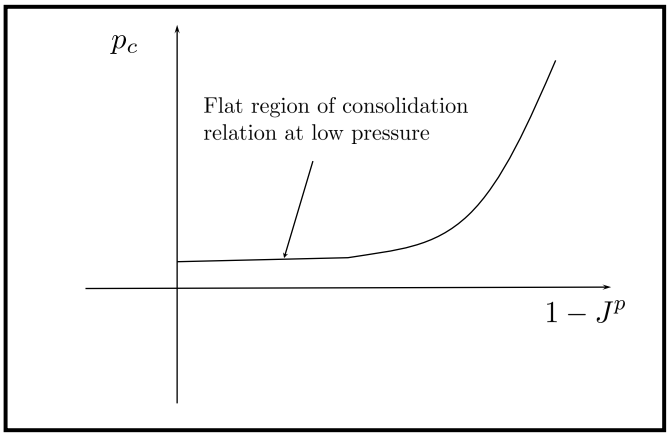

Figure 5.15: At low pressures, there is little hardening in the consolidation relation. We sketch an idealization of this consolidation curve.

strain rate than those in the previous section. The deformation process at non-critical state along with the lower stress drives the formation of smaller shear bands. Consistent with expectations, the temperature in the shear bands increases towards a constant value over time.

Evidently, examining Fig. 5.16, the comparison to the experimental data is rather good. We emphasize that none of the material model parameters here have been fit to this experimental data and rather have been derived via molecular dynamics calculations. Thus, we interpret the adiabatic shear localization process that we

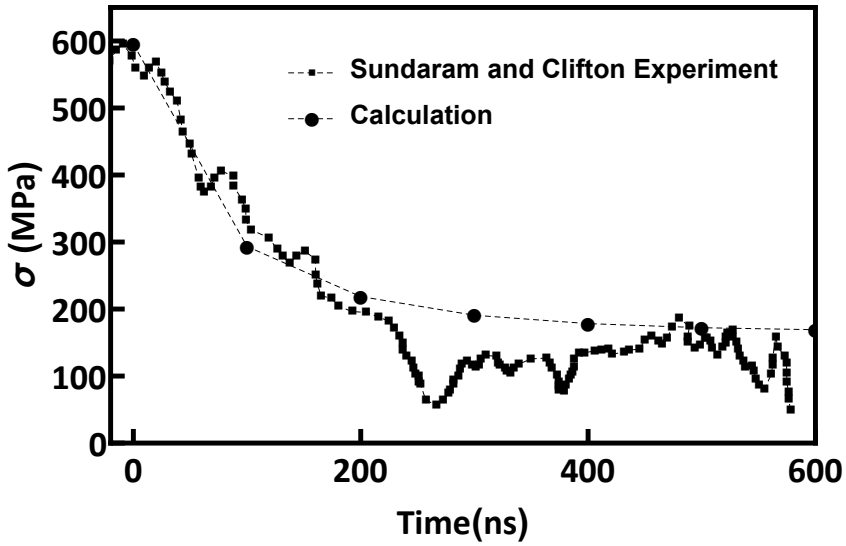

Figure 5.16: Stress history versus time due to Sundaram and Clifton [90] shifted to start at the onset drop in stress.

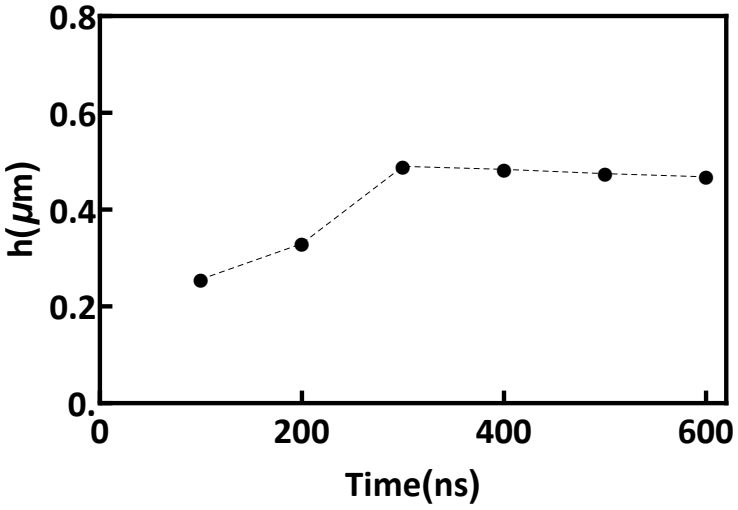

Figure 5.17: Shear band size versus time.

are modeling as a highly probable candidate mechanism for the large drops in stress observed in silica glass. We remark that though we have explored one particular weakening mechanism – namely adiabatic shear localization – there are other possible processes at play including both melting and confined fragmentation. Theoretical treatment of these processes could proceed along similar lines to the development in this work however detailed investigation is beyond the present scope.

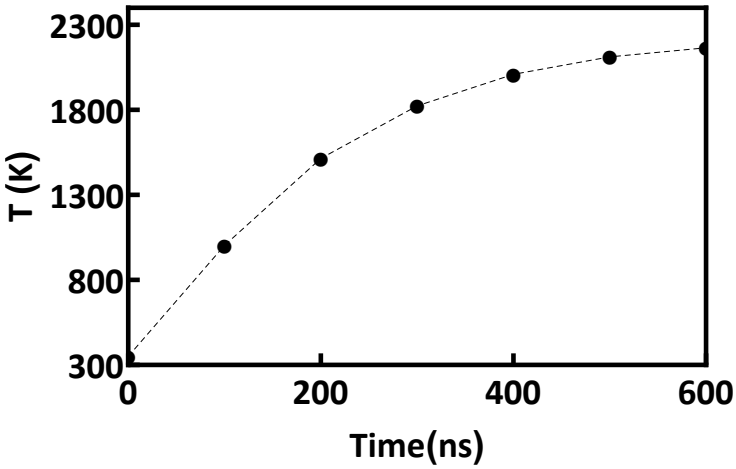

Figure 5.18: Temperature versus time.

5.6 Summary and concluding remarks

In this study, we have analyzed a model of plasticity (originally derived in [80]) for fused silica glass which accounts for the thermal and rate dependence of the media and determined that silica glass does admit microstructured deformation via shear banding. By computing incremental deformation along rank-one lines and leveraging the variational structure of the incremental update, we have determined the evolution of shear band thickness and approximate number of shear bands for a given sample size.

In addition, we have computed the corresponding yield stress supported by shear bands as function of time and pressure both at critical and non-critical state with no volumetric hardening. We have compared our computational results to the experimental flyer plate impact experiments of Sundaram and Clifton[90] and found that the agreement is remarkably good. This is strong evidence that adiabatic shear localization is the likely mechanism for the large drops in stress observed in silica glass.

The micro-mechanical origins of the anomalous yield behavior of silica glass lies in the formation of microstructure in stress space[78]. Thus, silica glass is a material that admits microstructure in both the deformation and stress fields. This is a unique and intriguing physics material behavior that we believe merits further study.

Finally, we propose a line of inquiry which is immediately suggested by the present study. The computational rank-one convexification procedure which jointly solves for the sub-length-scale is computationally rather simple – perhaps only slightly

more involved than many inelastic constitutive laws. A natural use case for this procedure would be to include it as a material point calculation within a numerical computational mechanics framework (finite elements, meshfree, etc.). This would, in principle, substantially mitigate common pitfalls such as mesh-dependence of the numerical solution due to lack of material energetic functional convexity.

Acknowledgements

This work was supported by a NASA Space Technology Research Fellowship.

Chapter 6

CONCLUSIONS AND FUTURE WORK

We have studied the behavior of silica glass from a variational and multiscale perspective. This effort resulted in a well posed model for the inelastic behavior of amorphous silica glass. In Chapter 2, we focused on the study of the anomalous yield behavior. We mined data from molecular dynamics and developed a finite deformation Cam-Clay model of plasticity. We found that a *non-local* formulation of the kinetic relation governing plastic flow in tandem with a concept from the direct methods in the calculus of variations [24] known as $\mathcal{A}$-quasi-convexity resulted in a well-posed model that captured the MD data.

In Chapter 3, we applied this model to the study of failure waves in glass rods using the optimal transport meshfree method. We found that the speed of the failure waves and the general characteristics of the behavior are well captured by the model. In Chapter 4, we introduced the effect of temperature and rate into the model. Specifically, we utilized max-ent-atomistics to aid in the characterization of rate. We found that the model captured the data well and the anomalous yield behavior persisted across a vast range of temperatures and strain rates.

In Chapter 5 we studied the occurrence of strain localization. We leveraged the variational structure of the model to jointly solve for both phase volume fractions as well as the micro-length scale. This amounts to essentially a rank-one convexification of the material model. The competition between thermal softening and rate hardening – which we have derived from microscale physics – dictated these processes. We compared the results of these calculations to experimental flyer plate impacts and found good agreement.

Silica glass is the first example (to our knowledge) of a material exhibiting a non-convex elastic domain derived from micro-mechanics. Furthermore, we have found that though this process is quantitatively dependent on temperature and rate, the non-convexity nonetheless holds for all regimes probed in this thesis. Thus, the relaxation of the non-convex limit domain and the corresponding rigorous connection between micro-structural patterning and the non-monotonicity of the critical state line is extremely robust with respect to these varied conditions.

There are many additional lines of research suggested by this thesis.

For instance, there are many soda lime glasses which are mostly SiO_2 with some additional constituents such as Mg, Na, or Ca. It would be a valuable contribution to quantify – in a similar manner to the study in Chapter 4 – the effect of chemical concentration of such added constituents on the inelastic material behavior.

We hope that the ideas presented in this work may be applied more broadly beyond silica glass and that this work may serve as a template – in some sense – for computational materials characterization for high velocity impact applications. In particular, as the so-called materials genome of engineering continues to dramatically grow, we hope that such computational characterization can be incorporated into materials selection for design. For instance, we envision robustness of flight hardware components in space craft to impact by debris or micro-meteoroids to be a topic of high importance in future space missions. Rapid analysis of candidate component material behavior that takes into account the complex thermodynamic states involved in such events would be a valuable contribution to engineering physics.

From a theoretical perspective, we also hope that the variational analysis of non-convex elastic domains in plasticity receives more attention. Such a viewpoint may be applied to more materials from the perspective of modeling. For instance, the author and colleagues are currently actively investigating a generic model for granular media where the elastic domain is non-convex.

The micro-mechanical origins of the anomalous yield behavior of silica glass lies in the formation of microstructure in stress space. As we saw in Chapter 5, silica glass admits microstructure in the deformation field. Thus, silica glass is a material that admits microstructure in both the deformation and stress fields. This is a unique and intriguing physical aspect of material behavior that we believe merits further study into the interaction of such processes. For instance, in the spirit of the incremental variational principles which we have utilized so heavily in this work, one could study the problem

$$\inf_{\boldsymbol{F}^p_{n+1}} \sup_{\boldsymbol{\sigma};\ \boldsymbol{\nabla}\cdot\boldsymbol{\sigma}=0} \int_\Omega W^p(\boldsymbol{F}^p_{n+1}) + \Delta t(\sigma \cdot \boldsymbol{l}^p - I_K(\boldsymbol{\sigma}))dX \,,$$

where both K is non-convex and W^p is non-convex and $\boldsymbol{l}^p = \boldsymbol{F}^e\dot{\boldsymbol{F}}^p\boldsymbol{F}^{p-1}\boldsymbol{F}^{e-1}$. Certainly, both of these cases have now been analyzed separately. However, does the joint interaction result in additional exotic behavior? Can formation of microstructure in one field be used to mitigate or control the microstructure formation in the

other? Perhaps such analysis could be used to motivate new avenues for determining design criterion.

Similarly, we could envision modeling plasticity and fracture jointly and assessing if non-convexity in the elastic domain effects the nature of crack propagation.

We now suggest a line of inquiry which is suggested by Chapter 5. In that chapter, the computational rank-one convexification procedure which jointly solves for the sub-length-scale is computationally rather simple – perhaps only slightly more involved that many inelastic constitutive laws. A natural use case for this procedure would be to include it as a material point calculation within a numerical computational mechanics framework (finite elements, meshfree, etc.) which would, in principle, substantially mitigate common pitfalls such as mesh-dependence of the numerical solution due to lack of material energetic functional convexity. Quite similarly, one could imagine a computational rank-2 convexification procedure for generic non-convex elastic domains.

Appendix A

APPENDICES

A.1 Relaxation of the limit-analysis problem

For completeness, we summarize the main concepts and arguments leading to the computation of the relaxed critical-state line and limit domain $\bar{K}$. Further mathematical details may be found in the article of [15].

We begin by introducing the dissipation functional $F : L^\infty(\Omega, \mathbb{R}^{3\times3}_{sym}, \mathrm{d}iv) \to \overline{\mathbb{R}}$ defined as

$$F(\boldsymbol{\sigma}) = \begin{cases} \int_{\partial\Omega} \boldsymbol{\sigma}\boldsymbol{\nu} \cdot \boldsymbol{g}\, d\mathcal{H}^2, & \text{if } \boldsymbol{\sigma} \in K \text{ almost everywhere in } \Omega, \\ -\infty, & \text{otherwise,} \end{cases} \tag{A.1}$$

where $L^\infty(\Omega, \mathbb{R}^{3\times3}_{sym}, \mathrm{d}iv)$ is the space of essentially bounded stress fields over Ω with zero distributional divergence endowed with its weak* topology and we assume Ω to be Lipschitz and bounded. Then, problem (4.55) is equivalent to

$$\sup_{\boldsymbol{\sigma}\in L^\infty(\Omega,\mathbb{R}^{3\times3}_{sym},\mathrm{d}iv)} F(\boldsymbol{\sigma}). \tag{A.2}$$

The question of existence of solutions of problem (A.2) may be ascertained by recourse to the direct method of the Calculus of Variations [16]. Thus, if K is bounded the functional F is clearly weakly coercive in $L^\infty(\Omega, \mathbb{R}^{3\times3}_{sym}, \mathrm{d}iv)$. In addition, if $\boldsymbol{g} \in L^1(\partial\Omega, \mathbb{R}^3)$, the space of integrable velocity fields over $\partial\Omega$, then the dissipation function

$$D(\boldsymbol{\sigma}) = \int_{\partial\Omega} \boldsymbol{\sigma}\boldsymbol{\nu} \cdot \boldsymbol{g}\, d\mathcal{H}^2 \tag{A.3}$$

is weakly continuous in $L^\infty(\Omega, \mathbb{R}^{3\times3}_{sym}, \mathrm{d}iv)$ by the trace theorem for $W^{1,1}(\Omega, \mathbb{R}^3)$ (cf., e.g., [2], p. 168).

In order to apply Tonelli's theorem [93], there remains to identify conditions under which F is upper-semicontinuous on $L^\infty(\Omega, \mathbb{R}^{3\times3}_{sym}, \mathrm{d}iv)$. We recall that F is upper-semincontinuous if $\limsup_{h\to\infty} F(\boldsymbol{\sigma}_h) \le F(\boldsymbol{\sigma})$ for every $\boldsymbol{\sigma} \in L^\infty(\Omega, \mathbb{R}^{3\times3}_{sym}, \mathrm{d}iv$ and every sequence $(\boldsymbol{\sigma}_h)$ converging weak* to $\boldsymbol{\sigma}$ in $L^\infty(\Omega, \mathbb{R}^{3\times3}_{sym}, \mathrm{d}iv)$. Wpect upper-semicontinuity to necessitate some appropriate notion of convexity of K. The appropriate notion is *symmetric* $\mathrm{d}iv$*-quasicoity*, which is a special case of $\mathcal{A}$-quasiconvexity, see Fonseca and Müller [25] and Conti S. [15] for the mathematical treatment.

Definition 1 (Symmetric d*iv*-quasiconvex function) *A function* $f : \mathbb{R}^{3\times3}_{sym} \to \overline{\mathbb{R}}$ *is symmetric* d*iv*-*quasiconvex if*

$$f(\boldsymbol{\sigma}) \leq \int_{(0,1)^3} f(\boldsymbol{\sigma} + \boldsymbol{\xi})\, dx, \tag{A.4}$$

for all $\boldsymbol{\sigma} \in \mathbb{R}^{3\times3}_{sym}$ *and all* $\boldsymbol{\xi} \in C^{\infty}_{per}([0,1]^3, \mathbb{R}^{3\times3}_{sym})$ *such that* $\mathrm{div}\, \boldsymbol{\xi} = \mathbf{0}$ *and* $\int_{(0,1)^3} \boldsymbol{\xi}\, dx = \mathbf{0}$.

This notion of convexity may be transferred to sets.

Definition 2 (Symmetric d*iv*-quasiconvex set) *A compact set* $K \subset \mathbb{R}^{3\times3}_{sym}$ *is symmetric* d*iv*-*quasiconvex if there is a symmetric* D*iv*-*quasiconvex function* $g \in C^0(\mathbb{R}^{3\times3}_{sym}; [0,\infty))$ *such that* $K = \{\boldsymbol{\sigma} : g(\boldsymbol{\sigma}) = 0\}$.

Evidently, every convex function, respectively convex set, is a symmetric d*iv*-quasiconvex function, respectively symmetric d*iv*-quasiconvex set, but the converse, as we shall see, is not true. The relevance of symmetric d*iv*-quasi-convexity to problem (A.2) stems from the following connection.

Theorem A.1.1 (d*iv*-quasiconvexity and upper-semicontinuity) *Suppose that the compact set* $K \subset \mathbb{R}^{3\times3}_{sym}$ *is symmetric* d*iv*-*quasiconvex. Then, the functional (A.1) is weak* upper semicontinuous in* $L^{\infty}(\Omega, \mathbb{R}^{3\times3}_{sym,\mathrm{div}}$.

This theorem is in the spirit of the classical theorems of Morrey [61], which put forth a equivalence between quasiconvexity and lower-semicontinuity of energy functionals. The proof of the theorem is based on the results of Fonseca and Müller [25] and may be found in [15]. Existence then follows from an application of Tonelli's theorem [93].

Theorem A.1.2 (Existence) *Let* $\Omega \subset \mathbb{R}^3$ *be bounded and Lipschitz. Suppose that* $K \subset \mathbb{R}^{3\times3}_{sym}$ *is a nonempty compact symmetric* d*iv*-*quasiconvex set. Let* $\boldsymbol{g} \in L^1(\partial\Omega, \mathbb{R}^3)$. *Then, the static problem (A.2) of limit analysis has solutions.*

Suppose now that K fails to be symmetric d*iv*-quasiconvex. Based on standard theory [16] we expect that the weak limits of maximizing sequences, representing

the macroscopic states of solids with increasingly fine microstructure, satisfy the relaxed problem

$$\sup_{\boldsymbol{\sigma}\in L^\infty(\Omega,\mathbb{R}^{3\times3}_{sym},\mathrm{d}iv)} \bar{F}(\boldsymbol{\sigma}), \tag{A.5}$$

where the relaxed functional $\bar{F} : L^\infty(\Omega, \mathbb{R}^{3\times3}_{sym}, \mathrm{d}iv) \to \overline{\mathbb{R}}$ has the form

$$\bar{F}(\boldsymbol{\sigma}) = \begin{cases} \int_{\partial\Omega} \boldsymbol{\sigma}\boldsymbol{\nu}\cdot\boldsymbol{g}\, d\mathcal{H}^2, & \text{if } \boldsymbol{\sigma} \in \bar{K} \text{ almost everywhere in } \Omega, \\ -\infty, & \text{otherwise,} \end{cases} \tag{A.6}$$

for some effective limit domain $\bar{K}$. Evidently, $\bar{K}$ must contain K and be symmetric div-quasiconvex in order for $\bar{F}$ to be upper-semicontinuous and the supremum in the effective problem (A.5) to be attained. In addition, $\bar{K}$ must be as small as possible in order for the solutions of the effective problem (A.5) to be weak limits of maximizing sequences of the unrelaxed problem (A.2). These constraints lead to the following notion of envelope.

Definition 3 (Symmetric div-quasiconvex envelope) *The symmetric* div*-quasiconvex envelope of a compact set $K \subset \mathbb{R}^{3\times3}_{sym}$ is the set*

$$\begin{aligned} \bar{K} = \{\boldsymbol{\sigma} \in \mathbb{R}^{3\times3}_{sym} \,:\, & g(\boldsymbol{\sigma}) \le \max g(K) \\ & \textit{for all symmetric } \mathrm{d}iv\textit{-quasiconvex } g \in C^0(\mathbb{R}^{3\times3}_{sym}; [0,\infty))\}. \end{aligned} \tag{A.7}$$

The remaining problem of interest is to determine the symmetric div-quasiconvex envelope $\bar{K}$ of sets K in the (p, q)-plane. For sets of a specific form, a construction of $\bar{K}$ has been put forth by [15]. Here we limit ourselves to summarizing the main arguments and refer the interested reader to [15] for mathematical details.

A main building block of the explicit construction of $\bar{K}$ is the following classical result of [91].

Theorem A.1.3 (Tartar'85) *The function $f(\boldsymbol{\sigma}) = 2|\boldsymbol{\sigma}|^2 - tr(\boldsymbol{\sigma})^2$ is symmetric* div*-quasiconvex.*

We recall that the critical-state surface of fused silica is isotropic and is defined by its trace, or critical-state line, on the (p, q)-plane. From Tartar's theorem A.1.3, [15] show the following.

Theorem A.1.4 *The set $\{\boldsymbol{\sigma} \in \mathbb{R}^{3\times3}_{sym} \,:\, q^2 \le s + \frac{3}{4}(p-r)^2\}$, with $r,\ s \in \mathbb{R}$, is symmetric* div*-quasiconvex.*

The curves $q = (s + \frac{3}{4}(p - r)^2)^{1/2}$ in (p, q)-plane represent rank-2 connections, or connections between stress states in equilibrium. By theorem A.1.4, the curves bound symmetric div-quasiconvex sets in the (p, q)-plane. Therefore, the smallest such set containing K, or *rank*-2 *envelope* of K, contains $\bar{K}$. [15] show that the rank-2 envelope of K and $\bar{K}$ in fact coincide, which effectively replaces the computation of $\bar{K}$ by the much easier task of constructing the rank-2 envelope of K.

For fused silica with K determined from MD data, the rank-2 envelope construction of $\bar{K}$ is given in Section 2.4, Table 2.5.

A.2 Dissipation function gradients

Here we compute the gradient of the dissipation function

$$\frac{\partial \psi^*(\dot{\boldsymbol{F}}^p)}{\partial \dot{\boldsymbol{F}}^p} = J\boldsymbol{F}^{e^T} \frac{\partial \tilde{\psi}^*}{\partial \boldsymbol{d}^p} \boldsymbol{F}^{-T} \ . \tag{A.8}$$

The gradient of the dissipation function per unit deformed volume is

$$\begin{aligned} \frac{\partial \tilde{\psi}^*}{\partial \boldsymbol{d}^p} = &\frac{1}{2}\left(\frac{\bar{\eta}}{\alpha^2}\operatorname{tr}(\boldsymbol{d}^p) - p_c + p_t\right)I + \frac{1}{2}\operatorname{tr}(\boldsymbol{d}^p)\frac{\bar{\eta}}{\alpha^2}I + \frac{2}{3}\bar{\eta}\operatorname{dev}\boldsymbol{d}^p \\ &+ \left(\frac{1}{2\alpha^2}\operatorname{tr}(\boldsymbol{d}^p)^2 + \frac{1}{3}\operatorname{dev}\boldsymbol{d}^p \cdot \operatorname{dev}\boldsymbol{d}^p\right)\frac{\partial \bar{\eta}}{\partial \boldsymbol{d}^p} \ , \end{aligned} \tag{A.9}$$

where

$$\frac{\partial \bar{\eta}}{\partial \boldsymbol{d}^p} = \frac{-q_c^2}{2\bar{\eta}\xi^2}\left(\frac{1}{2\alpha^2}\operatorname{tr}(\boldsymbol{d}^p)I + \frac{1}{3}\operatorname{dev}\boldsymbol{d}^p\right), \tag{A.10}$$

and

$$\xi \equiv \frac{1}{4\alpha^2}\operatorname{tr}(\boldsymbol{d}^p)^2 + \frac{1}{6}\operatorname{dev}\boldsymbol{d}^p \cdot \operatorname{dev}\boldsymbol{d}^p \ . \tag{A.11}$$

We now have specified the problem and may solve equation (3.9). It is worth noting that computing the second derivatives of $\mathcal{F}^{\alpha+1}$ is quite cumbersome. However, we have all the first derivative information so the problem is solvable by optimization methods such as the conjugate gradient.

Directly solving the above equations works in principle but often exhibits sensitivity to initial guess of $\boldsymbol{F}^p_{\alpha+1}$. Moreover, it is possible to produce a simplified computational strategy. We may specify $\boldsymbol{M}$ from equation (3.23) a priori and simply solve for $\Delta\epsilon^p$ at each iteration (approximating via backward difference $\boldsymbol{d}^p = \dot{\epsilon}^p\boldsymbol{M} \approx \dfrac{\Delta\epsilon^p}{\Delta t}\boldsymbol{M}$). We pursue this enhancement in the next section.

Let

$$g := W^e + W^p + \Delta\psi^* \ , \tag{A.12}$$

The taking stationarity with respect to $\Delta\epsilon^p$ we have

$$0 \in \frac{\partial W^e_{\alpha+1}}{\partial \boldsymbol{C}^e_{\alpha+1}} \frac{\partial \boldsymbol{C}^e_{\alpha+1}}{\partial \boldsymbol{F}^p_{\alpha+1}} \frac{\partial \boldsymbol{F}^p_{\alpha+1}}{\partial \Delta\epsilon^p} + \frac{\partial W^p_{\alpha+1}}{\partial J^p_{\alpha+1}} \frac{\partial J^p_{\alpha+1}}{\partial \boldsymbol{F}^p_{p+1}} \frac{\partial \boldsymbol{F}^p_{\alpha+1}}{\partial \Delta\epsilon^p} + \Delta t \left(\frac{\partial \psi^*}{\partial \Delta\epsilon^p} + \frac{\partial \psi^*}{\partial p_c} \frac{\partial p_c}{\partial \Delta\epsilon^p} \right). \tag{A.13}$$

We have, in fact, calculated most of this already. The remaining terms may be obtained as follows. The plastic symmetric spatial velocity gradient admits the decomposition

$$\boldsymbol{d}^p = \boldsymbol{F}^e \dot{\boldsymbol{F}}^p \boldsymbol{F}^{p^{-1}} \boldsymbol{F}^{e^{-1}} . \tag{A.14}$$

Discretizing this we obtain

$$\Delta\epsilon^p \boldsymbol{M} = \boldsymbol{F}^e_{\alpha+1} \left(\boldsymbol{F}^p_{\alpha+1} - \boldsymbol{F}^p_{\alpha} \right) \boldsymbol{F}^{p^{-1}}_{\alpha+1} \boldsymbol{F}^{e^{-1}}_{\alpha+1} , \tag{A.15}$$

from which we realize

$$\Delta\epsilon^p (\boldsymbol{F}_{\alpha+1})^{-1} \boldsymbol{M} \boldsymbol{F}_{\alpha+1} = \left(\boldsymbol{I} - \boldsymbol{F}^{p^{-1}}_{\alpha+1} \boldsymbol{F}^p_{\alpha} \right) . \tag{A.16}$$

This implies

$$\boldsymbol{F}^p_{\alpha+1} = \boldsymbol{F}^p_{\alpha} \left(\boldsymbol{I} - \Delta\epsilon^p (\boldsymbol{F}_{\alpha+1})^{-1} \boldsymbol{M} \boldsymbol{F}_{\alpha+1} \right)^{-1} \tag{A.17}$$

and

$$\frac{\partial \boldsymbol{F}^p_{\alpha+1}}{\partial \Delta\epsilon^p} = \boldsymbol{F}^p_{\alpha+1} \boldsymbol{F}^{-1}_{\alpha+1} \boldsymbol{M} \boldsymbol{F}_{\alpha+1} \boldsymbol{F}^{p^{-1}}_{\alpha} \boldsymbol{F}^p_{\alpha+1}. \tag{A.18}$$

Finally, we specify the remaining chain rule terms

$$\frac{\partial \psi^*}{\partial \Delta\epsilon^p} = \frac{J}{\Delta t} \tilde{\psi}^*(\boldsymbol{M}) , \tag{A.19}$$

$$\frac{\partial \psi^*}{\partial p_c} = J \frac{\tilde{\psi}^*}{p_c} , \tag{A.20}$$

and

$$\begin{aligned} \frac{\partial (J p_c)}{\partial \Delta\epsilon^p} &= \frac{\partial (J p_c)}{\partial J^p} \frac{\partial J^p}{\partial \boldsymbol{F}^p} \cdot \frac{\partial \boldsymbol{F}^p}{\partial \Delta\epsilon^p} \\ &= \left(\frac{\partial W^p}{\partial J^p} + J^p \frac{\partial^2 W^p}{\partial (J^p)^2} \right) J^p (\boldsymbol{F}^p)^{-T} \cdot \frac{\partial \boldsymbol{F}^p}{\partial \Delta\epsilon^p} . \end{aligned} \tag{A.21}$$

This constitutes all the necessary information to compute derivatives. We remark that since we have reduced the problem to finding $\Delta\epsilon^p$, it is sufficient to use a simple method such as the secant rule. More generally, it may become desirable to compute second derivatives for higher dimensional optimization problems – for instance optimizing the incremental variational update with respect to the entire $\boldsymbol{F}^p$ tensor.

BIBLIOGRAPHY

[1] Abou-Sayed, A. S., Clifton, R. J., 1976. Pressure shear waves in fused silica. Journal of Applied Physics 47 (5), 1762–1770.

[2] Ambrosio, L., Fusco, N., Pallara, D., 2000. Functions of bounded variation and free discontinuity problems. Oxford mathematical monographs. Clarendon Press, Oxford ; New York.

[3] Argon, A. S., 1979. Plastic deformation in metallic glasses. Acta Metallurgica 27 (1), 47–58.

[4] Ariza, M., Romero, I., Ponga, M., Ortiz, M., 2012. Hotqc simulation of nanovoid growth under tension in copper. International journal of fracture 174 (1), 75–85.

[5] Aubry, S., Fago, M., Ortiz, M., 2003. A constrained sequential-lamination algorithm for the simulation of sub-grid microstructure in martensitic materials. Computer Methods in Applied Mechanics and Engineering 192 (26-27), 2823–2843.

[6] Becker, R., 2012. A glass model capturing high-rate fracture observations. In: Technical Report, ARL-TR-6086. US Army Research Laboratory Aberdeen Proving Ground, MD.

[7] Becker, R. C., 2012. A glass model capturing high-rate fracture observations. Tech. Rep. ARL-TR-6086, U.S. Army Research Laboratory, Aberdeen Proving Ground, MD.

[8] Borja, R. I., 2002. Bifurcation of elastoplastic solids to shear band mode at finite strain. Computer Methods in Applied Mechanics and Engineering 191 (46), 5287–5314.

[9] Brar, N. S., Bless, S. J., Rosenberg, Z., 1991. Impact induced failure waves in glass bars and plates. Applied Physics Letters 59 (26), 3396–3398.
URL https://doi.org/10.1063/1.105686

[10] Carstensen, C., Hackl, K., Mielke, A., 2001. Non–convex potentials and microstructures in finite–strain plasticity. Proceedings of the royal society of London. Series A: mathematical, physical and engineering sciences 458 (2018), 299–317.

[11] Chen, M. H., Goldstein, M., 1972. Anomalous viscoelastic behavior of metallic glasses of Pd-Si-based alloys. Journal of Applied Physics 43 (4), 1642–1648.

[12] Clifton, R. J., Mello, M., Brar, N. S., 1998. Effect of shear on failure waves in soda lime glass. AIP Conference Proceedings 429 (1), 521–524.

[13] Coleman, B. D., Noll, W., 1963. The thermodynamics of elastic materials with heat conduction and viscosity. Archive for Rational Mechanics and Analysis 13 (1), 167–178.

[14] Conti, S., Muller, S., Ortiz, M., 2019. Symmetric div-quasiconvexity and the relaxation of static problems. In Submission.

[15] Conti S., Muller S., O. M., 2019. Symmetric div-quasiconvexity and the relaxation of static problems.

[16] Dacorogna, B., 1989. Direct Methods in the Calculus of Variations. Springer-Verlag New York, Inc., New York, NY, USA.

[17] Dacorogna, B., 2007. Direct methods in the calculus of variations. Vol. 78. Springer Science & Business Media.

[18] Dal Maso, G., 2012. An introduction to Γ-convergence. Vol. 8. Springer Science & Business Media.

[19] Demkowicz, M. J., Argon, A. S., Dec 2005. Autocatalytic avalanches of unit inelastic shearing events are the mechanism of plastic deformation in amorphous silicon. Phys. Rev. B 72, 245206.

[20] Dodd, B., et al., 1992. Adiabatic shear localization: occurrence, theories, and applications. Pergamon Press.

[21] Ekeland, I., Temam, R., 1999. Convex analysis and variational problems. Classics in applied mathematics. Society for Industrial and Applied Mathematics, Philadelphia.

[22] Evans, L. C., 2010. Partial differential equations.

[23] Falk, M. L., Langer, J. S., Jun 1998. Dynamics of viscoplastic deformation in amorphous solids. Phys. Rev. E 57, 7192–7205.

[24] Fonseca, I., Leoni, G., Müller, S., 2004. A-quasiconvexity: weak-star convergence and the gap. In: Annales de l'IHP Analyse non linéaire. Vol. 21. pp. 209–236.

[25] Fonseca, I., Müller, S., 1999. $\mathcal{A}$-quasiconvexity, lower semicontinuity, and Young measures. SIAM Journal on Mathematical Analysis 30 (6), 1355–1390.

[26] Gazonas, G. A., McCauley, J. W., Batyrev, I. G., Becker, R. C., Patel, P., Rice, B. M., Weingarten, N. S., 2011. Multiscale modeling of non-crystalline ceramics (glass). Tech. Rep. ARL-MR-0765, U.S. Army Research Laboratory, Aberdeen Proving Ground, MD.

[27] Holmquist, T. J., Johnson, G. R., 2011. A computational constitutive model for glass subjected to large strains, high strain rates and high pressures. Journal of Applied Mechanics 78 (5), 051003.

[28] Huang, L., Kieffer, J., Jun 2004. Amorphous-amorphous transitions in silica glass. i. reversible transitions and thermomechanical anomalies. Phys. Rev. B 69, 224203.

[29] Huang, L., Kieffer, J., Jun 2004. Amorphous-amorphous transitions in silica glass. ii. irreversible transitions and densification limit. Phys. Rev. B 69, 224204.

[30] Inamura, Y., Katayama, Y., Utsumi, W., Funakoshi, K.-I., Jun. 2004. Transformations in the Intermediate-Range Structure of SiO_2 Glass under High Pressure and Temperature. Physical Review Letters 93 (1), 015501.

[31] Jaynes, E. T., 1957. Information theory and statistical mechanics. Physical review 106 (4), 620.

[32] Jin, W., Kalia, R. K., Vashishta, P., Rino, J. P., 1993. Structural transformation, intermediate-range order, and dynamical behavior of sio 2 glass at high pressures. Physical review letters 71 (19), 3146.

[33] Jin, W., Kalia, R. K., Vashishta, P., Rino, J. P., Jul 1994. Structural transformation in densified silica glass: A molecular-dynamics study. Phys. Rev. B 50, 118–131.

[34] Kermouche, G., Barthel, E., Vandembroucq, D., Dubujet, P., 2008. Mechanical modelling of indentation-induced densification in amorphous silica. Acta Materialia 56 (13), 3222 – 3228.

[35] Kondo, K., Iio, S., Sawaoka, A., 1981. Nonlinear pressure dependence of the elastic moduli of fused quartz up to 3 gpa. Journal of Applied Physics 52 (4), 2826–2831.

[36] Kulkarni, Y., Knap, J., Ortiz, M., 2008. A variational approach to coarse graining of equilibrium and non-equilibrium atomistic description at finite temperature. Journal of the Mechanics and Physics of Solids 56 (4), 1417–1449.

[37] Lacks, D. J., Jun 1998. Localized mechanical instabilities and structural transformations in silica glass under high pressure. Phys. Rev. Lett. 80, 5385–5388.

[38] Lambrecht, M., Miehe, C., 2001. A note on formulas for localized failure of frictional materials in compression and biaxial loading modes. International journal for numerical and analytical methods in geomechanics 25 (10), 955–971.

[39] Lambrecht, M., Miehe, C., Dettmar, J., 2003. Energy relaxation of non-convex incremental stress potentials in a strain-softening elastic–plastic bar. International Journal of Solids and Structures 40 (6), 1369–1391.

[40] Langer, J. S., Jun 2001. Microstructural shear localization in plastic deformation of amorphous solids. Phys. Rev. E 64, 011504.

[41] Lee, E. D., 1969. Elastic-plastic deformation at finite strains. Journal of Applied Mechanics 13 (3), 167–178.

[42] Lemaître, A., Caroli, C., Aug 2009. Rate-dependent avalanche size in athermally sheared amorphous solids. Phys. Rev. Lett. 103, 065501.

[43] Li, B., Habbal, F., Ortiz, M., 2010. Optimal transportation meshfree approximation schemes for fluid and plastic flows. International Journal for Numerical Methods in Engineering 83 (12), 1541–1579.

[44] Li, B., Perotti, L., Adams, M., Mihaly, J., Rosakis, A., Stalzer, M., Ortiz, M., 2013. Large scale optimal transportation meshfree (otm) simulations of hypervelocity impact. Procedia Engineering 58, 320 – 327, proceedings of the 12th Hypervelocity Impact Symposium.
URL http://www.sciencedirect.com/science/article/pii/S1877705813009429

[45] Liang, Y., Miranda, C. R., Scandolo, S., Jan 2007. Mechanical strength and coordination defects in compressed silica glass: Molecular dynamics simulations. Phys. Rev. B 75, 024205.

[46] Lubliner, J., 1972. On the thermodynamic foundations of non-linear solid mechanics. International Journal of Non-Linear Mechanics 7 (3), 237 – 254.

[47] Lubliner, J., 1973. On the structure of the rate equations of materials with internal variables. Acta Mechanica 17 (1-2), 109–119.

[48] Lubliner, J., 1990. Plasticity theory. Macmillan ; Collier Macmillan, New York, London.

[49] Lubliner, J., 2008. Plasticity theory. Courier Corporation.

[50] Luo, S. N., Tschaune, O., Asimow, P. D., Ahrens, T. J., 2004. A new dense silica polymorph: A possible link between tetrahedrally and octahedrally coordinated silica. American Mineralogist 89, 455–461.

[51] M. Ponga, JP. Mendez, D. S., 2019. A computational framework to simulate long term diffusive transport phenomena in atomic systems. To be submitted 47 (5), 705–715.

[52] Malavasi, G., Menziani, M. C., Pedone, A., Segre, U., 2006. Void size distribution in md-modelled silica glass structures. Journal of Non-Crystalline Solids 352 (3), 285 – 296.

[53] Maloney, C. E., Robbins, M. O., 2008. Evolution of displacements and strains in sheared amorphous solids. Journal of Physics: Condensed Matter 20 (24), 244128.

[54] Mantisi, B., Tanguy, A., Kermouche, G., Barthel, E., 2012. Atomistic response of a model silica glass under shear and pressure. The European Physical Journal B 85 (9).

[55] Marian, J., Venturini, G., Hansen, B., Knap, J., Ortiz, M., Campbell, G., 2009. Finite-temperature extension of the quasicontinuum method using langevin dynamics: entropy losses and analysis of errors. Modelling and Simulation in Materials Science and Engineering 18 (1), 015003.

[56] Martin, J. B., 1975. Plasticity : fundamentals and general results. MIT Press, Cambridge, MA.

[57] Meade, C., Jeanloz, R., 1988. Effect of a coordination change on the strength of amorphous sio2. Science 241 (4869), 1072–1074.

[58] Miehe, C., Lambrecht, M., 2003. A two-scale finite element relaxation analysis of shear bands in non-convex inelastic solids: small-strain theory for standard dissipative materials. Computer Methods in Applied Mechanics and Engineering 192 (5-6), 473–508.

[59] Miehe, C., Lambrecht, M., Gürses, E., 2004. Analysis of material instabilities in inelastic solids by incremental energy minimization and relaxation methods: evolving deformation microstructures in finite plasticity. Journal of the Mechanics and Physics of Solids 52 (12), 2725–2769.

[60] Molinari, A., Clifton, R., 1987. Analytical characterization of shear localization in thermoviscoplastic materials. Journal of Applied Mechanics 54 (4), 806–812.

[61] Morrey, C. B., 1952. Quasi-convexity and the lower semicontinuity of multiple integrals. Pacific Journal of Mathematics 2 (1), 25–53.

[62] Ortiz, M., Pandolfi, A., 2004. A variational cam-clay theory of plasticity. Computer Methods in Applied Mechanics and Engineering 193, 2645–2666.

[63] Ortiz, M., Repetto, E., 1999. Nonconvex energy minimization and dislocation structures in ductile single crystals. Journal of the Mechanics and Physics of Solids 47 (2), 397–462.

[64] Ortiz, M., Stainier, L., 1999. The variational formulation of viscoplastic constitutive updates. Computer methods in applied mechanics and engineering 171 (3-4), 419–444.

[65] Pandolfi, A., Li, B., Ortiz, M., 2013. Modeling fracture by material-point erosion. International Journal of fracture 184 (1-2), 3–16.

[66] Pandolfi, A., Ortiz, M., 2012. An eigenerosion approach to brittle fracture. International Journal for Numerical Methods in Engineering 92 (8), 694–714.

[67] Pilla, O., Angelani, L., Fontana, A., Gonçalves, J. R., Ruocco, G., 2003. Structural and dynamical consequences of density variation in vitreous silica. Journal of Physics: Condensed Matter 15 (11), S995.

[68] Plimpton, S., 1995. Fast parallel algorithms for short-range molecular dynamics. Journal of Computational Physics 117 (1), 1 – 19.

[69] Polk, D. E., Turnbull, D., 1972. Flow of melt and glass forms of metallic alloys. Acta Metallurgica 20 (4), 493–498.

[70] Repetto, E., Radovitzky, R., Ortiz, M., 2000. Finite element simulation of dynamic fracture and fragmentation of glass rods. Computer Methods in Applied Mechanics and Engineering 183 (1), 3 – 14.
URL http://www.sciencedirect.com/science/article/pii/S004578259900208X

[71] Rice, J. R., 1976. The localization of plastic deformation.

[72] Rockafellar, R. T., 1970. Convex analysis. Princeton Mathematical Series. Princeton University Press, Princeton, N. J.

[73] Rockafellar, R. T., 1970. Convex analysis.

[74] Roscoe, K. H., Schofield, A. N., Wroth, C. P., 1958. On the yielding of soils. Geotechnique 8 (1), 22–53.

[75] Sato, T., Funamori, N., Dec 2008. Sixfold-coordinated amorphous polymorph of sio$_2$ under high pressure. Phys. Rev. Lett. 101, 255502.

[76] Sato, T., Funamori, N., Nov 2010. High-pressure structural transformation of sio$_2$ glass up to 100 gpa. Phys. Rev. B 82, 184102.

[77] Schill, W., Heyden, S., Conti, S., Ortiz, M., 2017. The anomalous yield behavior of fused silica glass. arXiv preprint arXiv:1710.05077.

[78] Schill, W., Heyden, S., Conti, S., Ortiz, M., 2018. The anomalous yield behavior of fused silica glass. Journal of the Mechanics and Physics of Solids 113, 105 – 125.
URL http://www.sciencedirect.com/science/article/pii/S0022509617309158

[79] Schill, W., Li, B., Ortiz, M., forthcoming. Optimal transport meshfree analysis of the impact of glass rods.

[80] Schill, W., Mendez, J., Ortiz, M., forthcoming. Temperature, rate, and the anomalous yield behavior of fused silica glass.

[81] Schill, W., Stainier, L., Ortiz, M., forthcoming. Shear localizaion in fused silica glass.

[82] Schmidt, B., Fraternali, F., Ortiz, M., 2009. Eigenfracture: an eigendeformation approach to variational fracture. Multiscale Modeling & Simulation 7 (3), 1237–1266.

[83] Schofield, A. N., Wroth, P., 1968. Critical state soil mechanics. European civil engineering series. McGraw-Hill, London, New York.

[84] Simha, C. H. M., Gupta, Y. M., 2004. Time-dependent inelastic deformation of shocked soda-lime glass. Journal of Applied Physics 96 (4), 1880–1890.

[85] Spaepen, F., 1977. A microscopic mechanism for steady state inhomogeneous flow in metallic glasses. Acta Metallurgica 25 (4), 407–415.

[86] Stainier, L., 2011. Consistent incremental approximation of dissipation pseudo-potentials in the variational formulation of thermo-mechanical constitutive updates. Mechanics research communications 38 (4), 315–319.

[87] Stainier, L., Ortiz, M., 2010. Study and validation of a variational theory of thermo-mechanical coupling in finite visco-plasticity. International Journal of Solids and Structures 47 (5), 705–715.

[88] Su, S., Stainier, L., 2015. Energy-based variational modeling of adiabatic shear bands structure evolution. Mechanics of Materials 80, 219–233.

[89] Su, S., Stainier, L., Mercier, S., 2014. Energy-based variational modeling of fully formed adiabatic shear bands. European Journal of Mechanics-A/Solids 47, 1–13.

[90] Sundaram, S., Clifton, R. J., Jul. 1998. Flow behavior of soda-lime glass at high pressures and high shear rates. In: American Institute of Physics Conference Series. Vol. 429 of American Institute of Physics Conference Series. pp. 517–520.

[91] Tartar, L., 1985. Estimations fines des coefficients homogénéisés. In: Ennio De Giorgi colloquium (Paris, 1983). Vol. 125 of Research Notes in Mathematics. Pitman, Boston, MA, pp. 168–187.

[92] Thompson, A. P., Plimpton, S. J., Mattson, W., 2009. General formulation of pressure and stress tensor for arbitrary many-body interaction potentials under periodic boundary conditions. The Journal of chemical physics 131 (15), 154107.

[93] Tonelli, L., 1921. Fondamenti di Calcolo delle Variazioni. Zanichelli, Bologna.

[94] Trinh, T. B., Hackl, K., 2014. Modelling of shear localization in solids by means of energy relaxation. Asia Pacific Journal on Computational Engineering 1 (1), 9.

[95] Tuckerman, M., 2010. Statistical mechanics: theory and molecular simulation. Oxford University Press.

[96] Tuckerman, M., Berne, B. J., Martyna, G. J., 1992. Reversible multiple time scale molecular dynamics. The Journal of chemical physics 97 (3), 1990–2001.

[97] van Beest, B. W. H., Kramer, G. J., van Santen, R. A., Apr 1990. Force fields for silicas and aluminophosphates based on ab initio calculations. Phys. Rev. Lett. 64, 1955–1958.

[98] Van Ginhoven, R. M., Jónsson, H., Corrales, L. R., 2005. Silica glass structure generation for ab initio calculations using small samples of amorphous silica. Physical Review B 71 (2), 024208.

[99] Vandembroucq, D., Deschamps, T., Coussa, C., Perriot, A., Barthel, E., Champagnon, B., Martinet, C., ???? Density hardening plasticity and mechanical ageing of silica glass under pressure: a raman spectroscopic study. Journal of Physics: Condensed Matter 20 (48), 485221.

[100] Venturini, G., Wang, K., Romero, I., Ariza, M., Ortiz, M., 2014. Atomistic long-term simulation of heat and mass transport. Journal of the Mechanics and Physics of Solids 73, 242–268.

[101] Wakabayashi, D., Funamori, N., Sato, T., Taniguchi, T., Oct 2011. Compression behavior of densified sio$_2$ glass. Phys. Rev. B 84, 144103.

[102] Wu, M., Liang, Y., Jiang, J.-Z., John, S. T., 2012. Structure and properties of dense silica glass. Scientific reports 2, 398.

[103] Yang, Q., Mota, A., Ortiz, M., 2005. A class of variational strain-localization finite elements. International Journal for Numerical Methods in Engineering 62 (8), 1013–1037.

[104] Yang, Q., Stainier, L., Ortiz, M., 2006. A variational formulation of the coupled thermo-mechanical boundary-value problem for general dissipative solids. Journal of the Mechanics and Physics of Solids 54 (2), 401–424.